Optimization of a Balance Drum

Labyrinth Seal to Minimize Leakage

_____

A Thesis

Presented to

The faculty of the School of Engineering and Applied Science

University of Virginia

_____

in partial fulfillment

of the requirements for the degree

Master of Science

by

NEAL ROBERT MORGAN

May

2014

APPROVAL SHEET

The thesis

is submitted in partial fulfillment of the requirements

for the degree of

Master of Science

_____

Neal Robert Morgan

The thesis has been read and approved by the examining committee:

_____

Houston G. Wood, Advisor

_____

Robert Ribando, Committee Chair

_____

Alexandrina Untaroiu, Committee Member

Accepted for the School of Engineering and Applied Science:

_____

James H. Aylor, Dean

School of Engineering and Applied Science

May

2014

II

ABSTRACT

Annular labyrinth seals are designed as tortuous paths that force a working fluid to expand and contract repeatedly through small clearances between high and low pressure stages of turbomachinery. The resulting expansion and recirculation reduces kinetic energy of the flow and minimizes leakage rate between regions of high and low pressure through the seal. Most current seal geometries are selected based on what has worked in the past, or by incremental improvements on existing designs. In the present research, a balance drum used in a multi-stage centrifugal pump was selected as a starting point, and design of experiments studies were performed to investigate the influence of groove shape and scale on leakage rate across the seal for a fixed pressure differential.

The CFD model of the baseline labyrinth seal has an upstream region leading to 20 evenly spaced semicircular grooves along a 267 mm seal length, with a clearance region of 0.305 mm. For each test parameterization, the definition of the seal geometry was specified by a set of five factors. The first parameterization factors allow for variation in scale of the semicircular grooves within a pattern of five independently scaled grooves repeated four times along the seal length. The second parameterization factors allow for a single repeated groove shape variation between a rectangular, triangular and semi-circular groove.

The seal was constructed with two parameterized CFD models in ANSYS CFX as a 5 degree sector of the full 3D seal. A designed experiment involving a non-central composite design was performed to investigate the effects of 5 parameters, representing seal groove radii, on leakage rate and rotordynamic coefficients of the seal. A second designed experiment was

performed as a five-level fractional factorial design to investigate groove shape on seal performance characteristics. This study demonstrates a practical approach for investigating the effects of various geometric factors on leakage rate and rotordynamic coefficients for balance drum seals. The empirical linear regression models fitted to the responses of the experimental designs suggest geometric parameters that could be applied to improve performance of future seals.

ACKNOLWEDGEMENTS

CONTENTS:

TABLE OF FIGURES

TABLE OF TABLES

NOMENCLATURE

Geometric Constants

c	seal clearance	[m]
D	seal diameter, inner	[mm]
L_S	axial seal length	[mm]
l_i	axial length of landing at the seal entrance and exit	[mm]
l_l	axial length of landing between grooves	[mm]
N	number of grooves along the seal	[−]
R	seal radius, inner	[mm]

Geometric Variables

$R_\blacksquare$	seal groove radius, indexed	[mm]
W	groove width	[mm]
f	groove flat width	[mm]
d	groove depth	[mm]
α	groove entrance angle	[°]
β	groove exit angle	[°]

Vibrational Analysis Variables

[C]	seal damping matrix	$\left[\frac{\text{N s}}{\text{m}}\right]$
[F]	seal force vector matrix	[N]
[K]	seal stiffness matrix	$\left[\frac{\text{N}}{\text{m}}\right]$
[M]	seal mass matrix	[kg]
$C_\blacksquare$	seal damping coefficient	$\left[\frac{\text{N s}}{\text{m}}\right]$
$K_\blacksquare$	seal stiffness coefficient	$\left[\frac{\text{N}}{\text{m}}\right]$
$M_\blacksquare$	seal mass coefficient	[kg]
x	displacement vector of the rotor axis	[m]

Fluid Dynamics Analysis Constants

a_1, b_2, b_3	Moody friction factor coefficients	$[-]$
n, m	Blasius friction factor coefficients	$[-]$
μ	working fluid dynamic viscosity	$\left[\dfrac{kg}{m\,s}\right]$
ω	fluid reference frame rotational speed	$\left[\dfrac{1}{s}\right]$
Re	Reynolds number	$[-]$
ρ	working fluid density	$\left[\dfrac{kg}{m^3}\right]$

Fluid Dynamics Analysis Variables

$\left[A_{ij}\right]$	CFD coefficient matrix	$[-]$
$\left[B_j\right]$	CFD solution residual errors matrix	$[-]$
$F_\blacksquare$	fluid reaction force	$[N]$
f	empirical friction factor	$[-]$
P	fluid pressure	$[Pa]$
$\varphi_\blacksquare$	CFD solution vector for flow properties	$[-]$
Q	fluid leakage rate	$\left[\dfrac{kg}{s}\right]$
S_i	shape function vectors	$[-]$
t	time	$\left[\dfrac{N\,s}{m}\right]$
$\tau_\blacksquare$	wall shear stress	$[Pa]$
U	fluid velocity magnitude	$\left[\dfrac{m}{s}\right]$
u, v, w	fluid velocity components: axial, radial, circumferential	$\left[\dfrac{m}{s}\right]$
x, r, θ	cylindrical coordinates, axial, radial, circumferential	$[-]$
$y+$	normalized distance from a wall	$[-]$

Regression Analysis and Experimental Design Variables

α_{star}	point spacing factor for star design	$[-]$
$\beta_{\blacksquare}$	linear least-squares regression model parameter, indexed	$[-]$
k	number of factors in composite experimental design	$[-]$
p	number of parameters in central experimental design	$[-]$
r	residual parameter of linear least-squares regression model	$[-]$
$\mathrm{x}_{\blacksquare}$	experimental regression factor	$[-]$
y	response of linear least-squares regression model	$[-]$

Superscripts

$\dot{\blacksquare}$	first derivative with respect to time	$[-]$
$\ddot{\blacksquare}$	second derivative with respect to time	$[-]$

Subscripts

$\blacksquare_x$	axial direction	$[-]$
$\blacksquare_\theta$	circumferential direction	$[-]$
$\blacksquare_{XX}$	direct matrix coefficients	$[-]$
$\blacksquare_{XY}$	cross-coupled matrix coefficients	$[-]$
$\blacksquare_{Rx}$	axial direction on rotor surface	$[-]$
$\blacksquare_{Sx}$	axial direction on stator surface	$[-]$
$\blacksquare_{R\theta}$	circumferential direction on rotor surface	$[-]$
$\blacksquare_{S\theta}$	circumferential direction on stator surface	$[-]$

CHAPTER 1: INTRODUCTION

Contact seals are used infrequently in rotating machinery due to wear and loss of energy to heat through friction. Instead, non-contacting annular seals are utilized, along secondary flow paths, to maintain distinctions of pressure between various regions in the primary flow path. These seals employ tight clearances, and specific geometry to promote fluid expansion, contraction, and recirculation within the seal, to dissipate energy and reduce the fluid leakage rate across the seal. Minimization of fluid leakage rate also maximizes the pressure differential across the seal, improving the overall efficiency of the turbomachine system.

The tight clearances are the cause of other interactions between the annular seal and the overall turbomachine system. The rotors, or shafts, of turbomachines tend to vibrate during operation. Rotordynamics is the study of the vibrations in rotating systems to predict resonant frequencies and, with that information, design safe systems. These vibrations are modeled with the vibrational equations of motion for a mass-spring-damper system, given as [1]:

$$[F] = [M][\ddot{x}] + [C][\dot{x}] + [K][x] \tag{1}$$

As the rotor vibrates, compression of the liquid between the vibrating rotor and the stator wall acts as a restorative force radially, but also causes tangential forces in the direction of rotation [2, 3]. These circumferential forces are dependent on the instantaneous radial eccentricity of the rotor and result in cross-coupling of the above vibrational equations of motion. That is to say, the conservation equations for the radial direction are not separable from those for the circumferential direction. Thus, in addition to the leakage rate of the

working fluid, the rotordynamic coefficients for the seal are critical components of its operating characteristics. Typically, operating characteristics of such seals are calculated using bulk flow models, computational fluid dynamics (CFD), or recently a hybrid bulk flow/CFD method [4].

1.1 Analysis Methodology

Analytical analysis of annular seals has grown from the initial study of the effect of the direct stiffness forces in the clearance region on dynamic stability by Lomakin in 1958 [2]. Current bulk flow analytical models are derived from initial work by Hirs [5], followed by Nelson [6]. Arghir and Frêne [7] review present advances in bulk flow analysis before presenting their own three control volume theory. Bulk flow models have the advantage of being derived analytically from the general Navier-Stokes equations of fluid motion. The solutions of flow rate and the rotordynamic stability characteristics of a seal are a simple numerical iteration solution of the bulk flow equations. These solutions have the advantage of being intuitively understandable, in addition to requiring relatively low cost in solution time or necessary computational power. Offsetting these advantages, the assumptions made to simplify the full Navier-Stokes equations limit the accuracy of bulk flow analysis methods. Specifically, the empirical models for friction factors, which govern fluid-solid wall shear interactions, are dependent on experimental observations and can vary widely based on the particular seal geometry and the operating conditions. Additionally, bulk flow analysis methods can be somewhat restrictive in terms of potential seal geometry. The complexity of formulating the bulk flow governing equations increases significantly when any grooves are added to a plain

2

seal, let alone if the grooves themselves have complex geometric shapes or are non-uniform along the axial length of the seal.

The alternative to bulk flow analysis, is the use of CFD for solving the complete Navier-Stokes equations in conjunction with an appropriate turbulence model [7-13]. Unlike the bulk flow models, computational fluid dynamics makes no simplifying assumptions based on the seal geometry, shear stress at the wall, relationship between wall shear stress and mean fluid velocity, or characterization of interfaces between control volumes through empirical friction factors. The annular seal flow behavior is obtained while rapid flow variations at the interface between the groove and land sections are inherently incorporated into the solution. Although lack of the above simplifying assumptions provides increased accuracy for CFD methods, CFD models can be expensive in terms of modeling time and computational power. Even neglecting the time and effort required to create a quality mesh of the fluid region and the availability of modern parallel computing clusters, a full seal model can take hours or days to solve a single case. Considering that it is necessary to run each seal geometry at multiple whirl speeds to determine the rotordynamic coefficients, performing large scale experimentation can be impractical.

Recently, a new method has been developed by Migliorini *et al.* [4] that combines the benefits of both bulk flow and CFD methods. This method replaces the base state of the bulk flow equations with the solutions from a CFD model representing a small sector of the full non-eccentric seal. Using a smaller CFD model with a steady state solution greatly decreases solution time, while still providing an accurate representation of the unperturbed flow behavior

in the seal. The bulk flow methodology can then be applied to solve for the rotordynamic coefficients of the seal. The increased accuracy over standard bulk flow analysis, decreased solution time, and decreased computational expense make this analysis method the most practical for testing potential seal geometric designs.

1.2 Prior Work

Rhode, Ko, and Morrison [14] performed optimization of leakage rate through step labyrinth annular seals. The leakage rate of the step seal was calculated using a numerical Navier-Stokes code based on the TEACH algorithm with a variation in the QUICK differencing scheme and the high Reynolds number k-ε turbulence model. Seven characteristic geometric parameters were varied over 16 simulation experiments. The simulation experiment with minimum leakage rate was selected to be investigated experimentally for verification of the numerical code. The predicted optimal seal geometry had a 60% less leakage than their baseline seal geometry, and suggested some significant factors relating step seal geometry to leakage rate. The results of this work show the benefits of optimizing seal geometry designs for improved leakage rate.

Schramm, Denecke, Kim and Wittig [15] performed simulated annealing optimization of step labyrinth seal geometry. The step seal geometry shape was parameterized for only two design variables representing step position and step height. A three-dimensional CFD mesh was automatically generated and TASCflow3D was used to solve for the seal's flow properties. Nine hundred simulation experiments were performed with factor values selected by the optimization algorithm. Both factors converged to predicted optimum values after

approximately 600 simulations, resulting in an improved leakage rate of greater than 10%. The resulting data was plotted to perform a sensitivity study relating the step position and step height to seal discharge coefficient. Linking automated mesh generation, CFD and optimization codes was demonstrated to produce improved seal geometries, even with simple parameterizations. Additionally the application of the simulated annealing optimization algorithm was found to work with the design space of the stepped labyrinth seal parameters.

Asok, *et al.* 2007 [16] employed an artificial neural network simulation model to optimize labyrinth seal groove geometries for minimal leakage rate. Initially five different aspect ratio square cavity labyrinth seal groove geometries were simulated in Fluent with the second-order upwind SIMPLEC algorithm. The CFD results for the square cavity labyrinth seal geometries were confirmed by physical experiment. Artificial neural network simulation and analytical modeling were then combined to predict the performance of new seal geometries based on the CFD results of the previous simulations. Additionally, based on the flow fields found in the square cavity grooves by CFD simulation, two new seal geometries were defined with curved cavity walls at the rear of the grooves. This additional curve creates a counter rotating double vortex in the groove cavity resulting in a pressure differential increase of more than 75%. The results of this study suggest that investigation of novel groove geometries can yield significant performance increases.

Untaroiu, et al. [11] also performed CFD simulation and verified with physical experiments. The four factor parameterized seal geometry was meshed and simulated using ANSYS CFX. The design factors include the seal tooth front and back angles, the tooth tip width,

and the spacing between teeth. The CFD simulation results for five seal geometries were verified by physical experiment. Subsequently, design factor values selected based on the output of a genetic optimization algorithm. The genetic algorithm was used to generate design points for 38 simulated experiments and a sensitivity study was performed with this sample. This study demonstrates the effective use of a genetic optimization algorithm for prediction of local optimum design points.

Bellaouar, Kopey, and Abdelbaki [17] performed a similar optimization of annular labyrinth seal tooth geometry using the multivariate Gauss-Seidel iteration method. The five parameterization factors under investigation include the seal tooth front and rear angles, and the rounding radii on each side of the base and tip of the seal tooth. Cosmos FloWorks 2009 for SolidWorks 2009 was the CFD code employed to model the performance of the test seal geometries. This study demonstrates the use of the Gauss-Seidel iteration method to optimize seal geometry for reduced leakage rates.

Pierret, Coelho, and Kato [18] did not optimize labyrinth seal geometries. However, the optimization method employed by their study parallels the approach of this thesis. The NASA rotor 67 geometry is used as a baseline for the shape optimization of three dimensional compressor blades. A method was proposed to improve the efficiency of genetic algorithm optimization by applying the optimization algorithm to a multiple regression model instead of directly to the CFD simulation experiments. This requires first creating a design of experiments (DOE) to select initial design points for simulation. The responses of these design points were then analyzed to produce a multiple regression model relating the design factors to the

response data. The genetic algorithm was applied to these analytical models to predict optimal design points, which are then simulated, added to the library of simulation data, and used to modify the analytical model further. This study demonstrates the applicability of design of experiments statistics and multiple regression analysis to simplify and increase the efficiency of optimizing a geometric flow problem.

1.3 Motivation and Plan of Work

Current seal geometry designs are usually based on what has worked in the past, or by incremental improvements on existing designs. The goal of this study is to demonstrate a novel approach to iterative seal design. This will be done by investigating the effects of various geometric factors on leakage rate for a labyrinth seal model using CFD. The balance drum labyrinth seal, Figure 1.2, from the eight-stage pump, Figure 1.1, was selected as a baseline for comparison of results. Two seal geometry parameterizations will be chosen and tested. Design of experiments will be used to create efficient test plans to explore and model the effects of seven response variables characterizing the behavior of an annular seal in a larger turbomachine system model. The seven characteristic responses of the annular seal model will be leakage rate plus the six rotordynamic coefficients that form the skew-symmetric coefficient matrices for the dynamic stability equations of motion. Multiple linear regression analyses will be employed to provide a sensitivity analysis of the seven responses with respect to the parameterization factors. The sensitivity analysis can also act as a map for seal designers to minimize leakage or tune a seal's geometry to provide particular rotordynamic coefficients to match their larger turbomachine system. Thus, a practical approach for seal design that

combines CFD with characterization of the performance characteristics via experimental design

and statistical modeling of the relevant response variable is proposed.
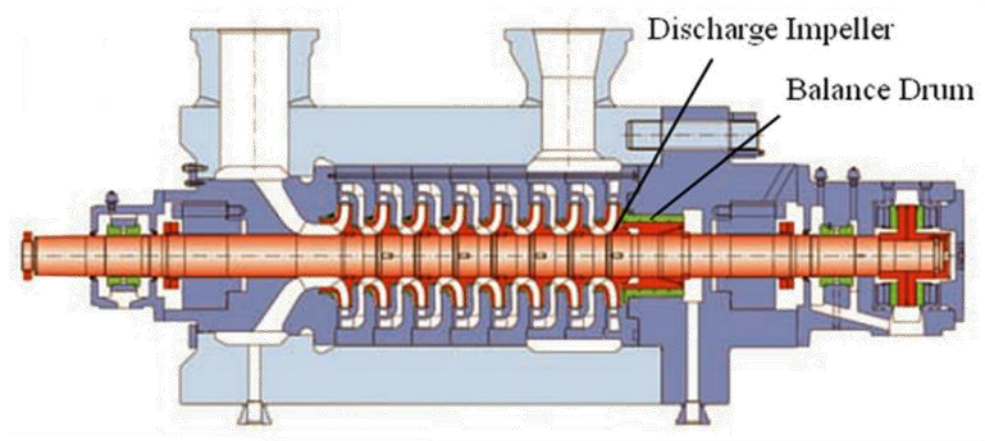
Figure 1.1: FlowServe 8-stage water pump
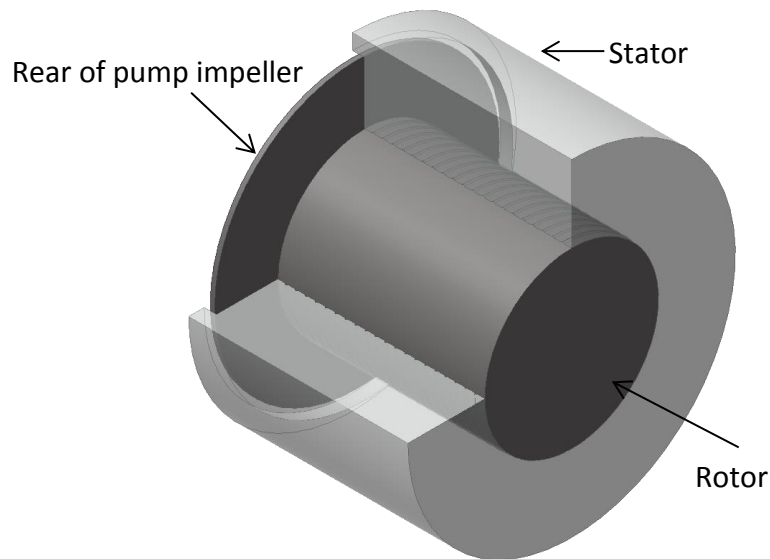
Figure 1.2: Balance drum labyrinth seal, cutaway view

CHAPTER 2: BACKGROUND

This chapter contains an overview of the computational, analytical and statistical methods employed by this study. First the fluid mechanics of the computational fluid dynamic (CFD) simulations performed in ANSYS CFX will be discussed. The CFD results will be used as the base state for the zeroth-order bulk flow equations to improve the accuracy of the bulk flow solutions for rotordynamic coefficients. A summary of bulk flow theory is presented, followed by the hybrid CFD/bulk flow methodology. A discussion of experimental design and its application to optimization of CFD parameters is then presented. Finally, statistical criteria for judging the quality of multiple linear regression models are discussed.

2.1 ANSYS CFX

CFD simulations for this study are performed in ANSYS CFX versions 13.0 and 14.0. CFX numerically solves a discrete formulation of the full unsteady Navier-Stokes conservation equations [19, 20, 21]. This study assumes a Newtonian incompressible fluid due to the properties of the working fluid and operating conditions of the seal. Thus the energy conservation equation and the equation of state are neglected. Conceptually, any flow can fully be defined by the solution of the Navier-Stokes equations. Unfortunately, any significant turbulence in the flow means that present day computational power is not sufficient to solve a mesh that would be fine enough to resolve the smallest turbulent length scales by direct numerical simulation (DNS). To overcome this challenge, CFX relies on modifications to the original Navier-Stokes equations and additional information provided by an appropriate turbulence model.

2.1.1 Governing Equations: Reynolds Averaged Navier-Stokes Equations

Because it is not feasible to calculate the behavior of every temporal and spatial turbulent disturbance in the flow, the Reynolds averaged Navier-Stokes (RANS) equations are used to represent the average characteristics of the flow properties for larger time and space scales. To achieve this statistical representation of the flow, the RANS equations redefine the dependent variables of the Navier-Stokes equations as time-averaged and instantaneous perturbation terms. Time-averaged terms are averaged over a time scale that is much smaller than the entrainment time for a fluid element in the seal, but large compared to the turbulent perturbations. The dependent variables in question are pressure and velocity for the conservation and momentum equations. This study employs an incompressible model; however, were compressibility an issue, the independent variables would be time averaged with a density weighting. The compressible perturbation terms fluctuate over time and pressures, and thus would not automatically average to zero like a variable that is only perturbed in time. Substituting the new dependent variables into the previous continuity and momentum equations and time-averaging the equations as a whole, gives the RANS equations for an incompressible flow. All perturbation terms vanish due to the time averaging process, except for the term representing stresses from turbulent mixing. This term is known as the Reynolds stress tensor. The Reynolds stresses are now an additional unknown term without an additional equation to solve. Annular seal literature commonly applies the two equation k-ε turbulence model to allow the solution of the additional unknown in the momentum conservation equation [21]. The k-ε turbulence model is an "eddy viscosity" turbulence model.

This category of model is defined by the Boussinesq assumption in which turbulence is characterized by spontaneous evolution and break-up of small eddies [22]. The fluid stresses resulting from eddies are correlated to the time-averaged strain rate by a determined constant representing the viscosity of the turbulent flow in an eddy, μ_t [23].

2.1.2 Scalable Wall Function

Both the rotor and stator walls are defined by a no-slip boundary condition. CFX deals with a no-slip wall by defining the tangential velocity in the turbulent boundary layer as a function of wall shear stress, τ_w, and distance from the wall, Δy or $y+$. Near the wall, in the "viscous sublayer", the relationship between distance and velocity tangent is linear before transitioning to a logarithmic relationship as the flow becomes fully turbulent. The ANSYS CFX "scalable wall function" is designed to mitigate the near wall mesh sensitivity of these calculations. This is done by setting a minimum value for the normalized distance from the wall to 11.06. The specific value is chosen by the intersection of the velocity predictions for the viscous sublayer and the fully turbulent region [21].

2.1.3 Numerical Solution Method

The Navier-Stokes equations do not have analytical solutions for flows as complex as those presented in this study. Instead, ANSYS CFX discretizes the fluid domain into small control volumes using a user defined mesh. The fluid properties for the domain are stored at each node, or corner, of the control volumes. The RANS conservation equations and turbulence model are then integrated over the control volume. Source and time differentiation terms are evaluated at the centroid of the control volume, while flux integrals are evaluated at the

midpoint of a line connecting the centroid of the control volume to the respective face. The flow properties are then found by application of a backwards, or implicit, Euler method to the governing equations. This numerical iteration method equates the differential form of the governing equations to change in flow properties between times t_0 and $t_0 + \Delta t$, through the integrated governing equations. In the case of a steady-state simulation, the time step both resolves turbulent time scales and functions as a limiter on the rate of convergence.

2.1.3.a Shape Functions

The fluid flow variables and flow properties stored at each node are combined with simple algebraic "shape functions" and summed to represent the approximate influence of each node in a given control volume at the points of integration, shown in Equation 2. The shape functions, S_i, allow the value of the flow properties, represented by φ, and the influence of the element's nodes to vary throughout each element. The summed shape functions for each element act as general solutions to the discretized RANS equations.

$$\varphi = \sum_i^{nodes}(S_i\varphi_i) \tag{2}$$

ANSYS CFX employs different shape functions based on the number of nodes defining an element, which is dictated by the shape of the elements used to mesh the fluid domain. Because the fluid domains in the present work are meshed with a sweep method, the only type of elements employed herein are hexahedral and "wedge", or triangular prism, elements. The sweep method takes a two-dimensional mesh of triangles and/or quadrilaterals and "sweeps" it across a three-dimensional body of constant cross section to create three-dimensional prism

elements. The various element shapes and their shape functions are given in ANSYS documentation [19-21,23].

2.1.3.b Solution and Determination of Residuals

The discretized RANS equations formulated for each element in the domain form a system of linear equations. Equation 3 shows the general matrix representation of the equations. The variable φ_j represents the solution vector composed of shape functions as seen above. Matrix a_{ij} consists of coefficients and b_i is a measure of solution residual errors. All conservation equations are coupled, which requires larger memory capacity to store coefficients, but increases solution efficiency and robustness.

$$[a_{ij}][\varphi_j] = [b_i] \tag{3}$$

ANSYS CFX employs a "Multigrid (MG) accelerated Incomplete Lower Upper (ILU) factorization technique" to solve the linear system of equations [19, 21]. The "Multigrid", or "Algebraic Multigrid", portion of the technique refers to the process of using a progressively coarser mesh, composed of multiple control volumes from the base mesh, as iterations progress and transferring the resulting solution back to the "fine" or base mesh. Each iteration of a fine mesh can smooth out residuals within each individual element, however more widely spread residuals, or larger, will take many iterations to be corrected. The algebraic multigrid method sums the solutions for several fine grid elements to simulate the use of a coarser grid structure, increasing the rate at which residuals may be reduced. This coarser grid allows larger steps to improve large residuals, and allows the small scale errors to average out in the larger control volume, later to be dealt with by the fine mesh residuals.

Errors in the simulation can occur in any control volume element in the domain, and similar to the variables for which we are trying to solve, these errors can be diffused to neighboring elements. The neighboring elements may have their own errors that amplify or cancel errors being transmitted to them. The primary method of reducing the inception of error sources is to increase mesh density in regions of the fluid domain that have large gradients of the variables being solved.

2.2 Bulk Flow Analysis

Bulk flow models have been used to model annular seals for more than 40 years [5]. Bulk flow models are an analytical application of the Navier-Stokes equations [1]. These equations are simplified by various assumptions and separated axially into several large control volumes, in which each flow property is assumed to be equal to a "bulk", or average value. Bulk flow models have evolved, presently using 1, 2 or 3 control volumes depending on geometry, working fluid, and preference [1,6,24-26]. The fluid region of the baseline labyrinth seal, from the 8-stage pump shown in Figure 1.1, is shown in Figure 2.1, with a cross-section of one of the seal grooves. As labeled, the flow moves from the high pressure region on the left side into the upstream cavity, between the last pump impeller and the seal, and into the seal's clearance region to exit on the right side. This work selects a single control volume bulk flow model and approximates the semi-circularly grooved labyrinth seal as a smooth walled plain seal. The plain seal simplification was chosen for the simplicity of the analytical model.
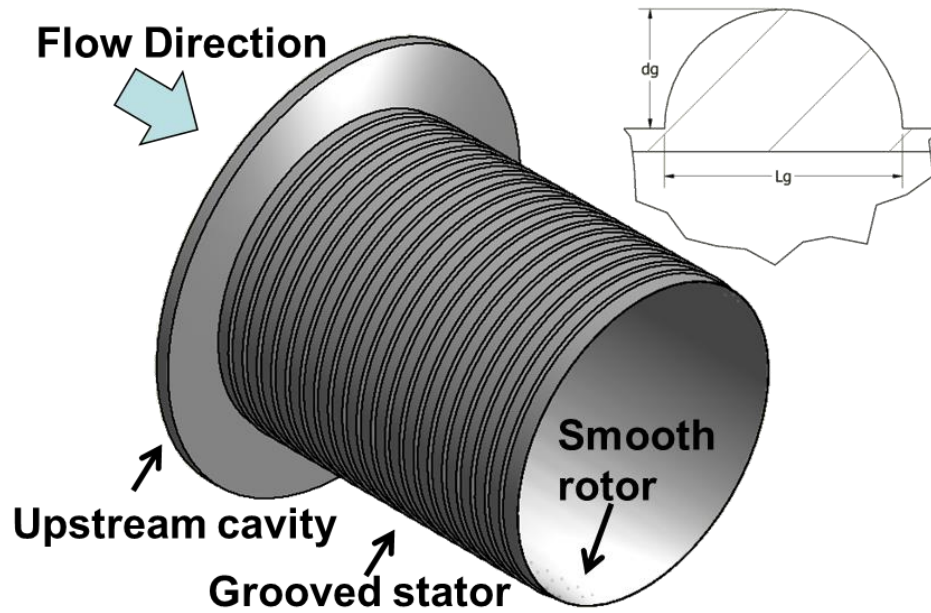
Figure 2.1: Fluid region and groove cross-section of the baseline labyrinth seal

2.2.1 Assumptions

The working fluid and dimensions of a typical plain, or grooved, labyrinth seal allow for some assumptions:

1. The flow is turbulent.

2. Radial pressure variation in a CV is negligible compared to axial pressure variation.

3. Velocity components are averaged radially and over each control volume axially and circumferentially.

4. Curvature of the seal in the circumferential direction may be neglected.

5. The rotor eccentricity is no larger than 10% of the seal's radial clearance.

6. When the rotor is not eccentric, the flow is steady state and fully developed.

7. The working fluid is assumed to be a Newtonian incompressible fluid.

The first assumption of turbulence can easily be demonstrated by calculating an approximate Reynolds number for the example labyrinth seal. A low estimate for velocity is obtained by temporarily neglecting the pressure differential and assuming Couette flow

between two infinitely long and concentric cylinders with the inner cylinder (of radius a) rotating at 3455 RPM, specified as the operating speed of the nominal seal from industry, with the outer cylinder (of radius b) held stationary [27, 28]. This method gives an estimated Reynolds number on the order of 13,000, defined by Equation 4 below [9]. The Reynolds number is based on twice the clearance region height representing the two wetted surfaces. Reynolds numbers greater than 2,000, for pipe flow, are assumed turbulent, thus the flow in the seal is assumed turbulent.

$$Re = \frac{2\rho Uc}{\mu} \qquad (4)$$

The second and third assumptions define the "bulk" flow approach by assuming a bulk value for the flow variables. These second and third assumptions also define velocity as a function of only circumferential coordinate (θ), axial coordinate (x), and time ($v = v(\theta, x, t)$). The fourth assumption is justified by the ratio of seal clearance to radius being on the order of 0.003 [1]. The ratio indicates that the difference between integrating circumferentially on the rotor surface and the stator surface can be neglected. The fifth assumption, limiting the assumed scale of rotor eccentricity, is not necessary for the formulation of the modified Navier-Stokes equations; however, it becomes necessary for the estimation of both the wall shear stresses and the seal's rotordynamic coefficients. The small eccentricity assumption supports a further assumption of linear perturbation of the rotor's eccentricity. The sixth assumption, of steady state conditions, applies only to the initial solutions of the governing equations without rotor eccentricity. The last assumption, that the working fluid is Newtonian and incompressible, is only relevant to our particular example seal with its working fluid of water. It is assumed that

16

the water temperature does not change significantly along the length of the seal, thus allowing

the energy equation to be omitted [29].

2.2.2 One Control Volume

The one-control-volume bulk flow model is primarily for smooth rotor/smooth stator

annular seals. The simplification of modeling the labyrinth seal as plain makes for a simple

formulation of the Navier-Stokes equations for the problem. The single control volume fluid

element is illustrated in Figure 2.2, and free body diagrams of the CV are shown in Figure 2.3. In

the free body diagrams the shear stresses on the rotor and stator walls are represented by τ's,

methods for approximating the shear stress will be discussed in a later section. The mass, axial

momentum and circumferential momentum equations are shown in order as Equations 5-7 [1,

6]. From the left the terms in the continuity equations represent the gradient of flow

circumferentially across the fluid element, the axial flow along the seal, and the change in

clearance with respect to time as the fluid whirls around the eccentric rotor and the rotor

rotates about its axis.
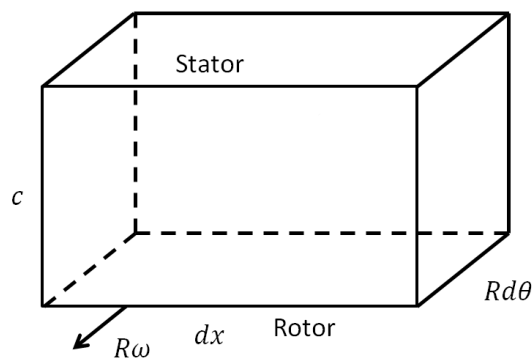
Figure 2.2: Single Control Volume Fluid Element
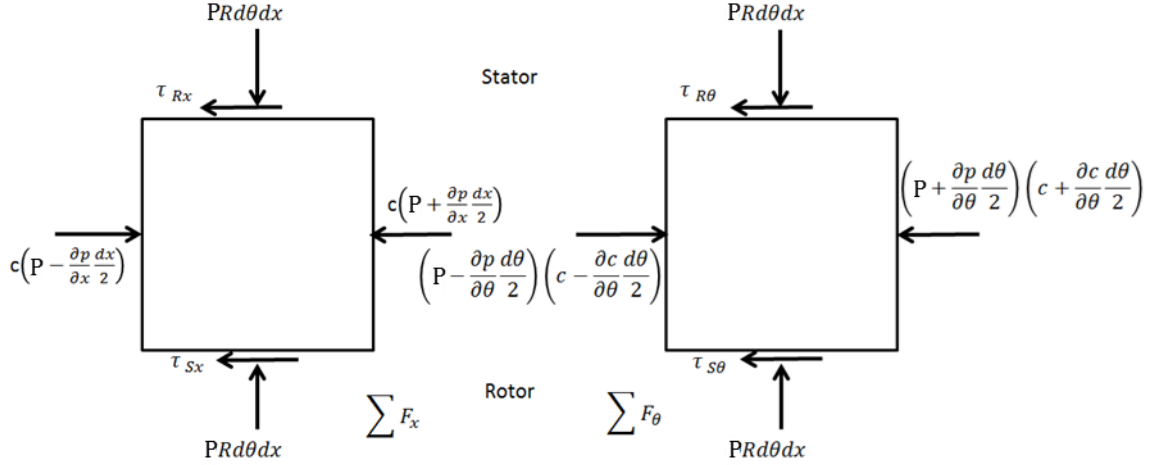
Figure 2.3: Free Body Diagrams, with $\sum \boldsymbol{F_x}$ on the left, and $\sum \boldsymbol{F_\theta}$ on the right

$$0 = \frac{\partial}{\partial t}(c) + \frac{\partial}{\partial x}(cu) + \frac{1}{R}\frac{\partial}{\partial \theta}(cw) \tag{5}$$

$$-c\frac{\partial P}{\partial x} - (\tau_{Rx} + \tau_{Sx}) = \frac{\partial}{\partial t}(\rho cu) + \frac{\partial}{\partial x}(cu^2) + \frac{1}{R}\frac{\partial}{\partial \theta}(cuw) \tag{6}$$

$$-\frac{c}{R}\frac{\partial P}{\partial \theta} - (\tau_{R\theta} + \tau_{S\theta}) = \frac{\partial}{\partial t}(\rho cu) + \frac{\partial}{\partial x}(cwu) + \frac{1}{R}\frac{\partial}{\partial \theta}(cw^2) \tag{7}$$

2.2.3 Shear Stress Models

Wall shear stress is modeled with an empirical friction factor, relating the resultant shear stresses to the resultant relative velocities, as seen in Equation 8. This friction factor can then be estimated in many ways; however, all of the estimates are functions of Reynolds number, defined above in Equation 4. Hirs and Childs use a Blasius friction factor model, Equation 9, where n and m are the empirical coefficients [1, 5]. However, Childs also uses a Moody friction factor, Equation 10, where the a's and b's are empirical coefficients, and e is the absolute roughness of the wall [1, 30]. Other potential friction factor models include Fanning and Darcy-Weisbach friction factors [1, 5].

18

$$f = \frac{\tau}{1/2 \rho U^2} \tag{8}$$

$$f_B = n(\text{Re})^m \tag{9}$$

$$f_M = a_1 \left[1 + \left(\frac{b_2 e}{2c} + \frac{b_3}{\text{Re}} \right)^{1/3} \right] \tag{10}$$

2.2.4 Rotordynamic Coefficients

The rotordynamic coefficients represent the terms of the stiffness, damping, and mass matrices in the rotor system's vibrational equations of motion [1]. These matrices are skew-symmetric and homogeneous when written in Cartesian coordinates. The coefficients may be solved for by treating the vibration of the rotor as a small linear perturbation. Perturbation theory allows the solution of differential equations by treating them as slight variations on a known solution. The resulting additional equations allow for the calculation of the flow through the seal for different operating conditions. The rotordynamic stiffness, damping, and mass coefficients are then determined from the perturbed pressure profiles.

2.2.4.a Nondimensionalization and Perturbation of the RANS Equations

Perturbation theory is similar to the idea of Taylor series approximations. The approximation starts at some known value and increasingly higher-order terms are included to approach the true solution. For the purposes of this study, only the zeroth and first-order equations are used. The first step towards setting up the perturbation equations is to nondimensionalize the governing equations. Nondimensionalization is performed to allow the scaling of the rotor's eccentricity to the nominal height of the straight seal clearance region. This is common practice and establishes the small perturbation parameter as the rotor's

nondimensional eccentricity which is not typically analyzed at greater than 10% of the clearance region. The seal length is assumed to be much less than that of the rotor allowing any axial variation in clearance to be neglected. This small perturbation of clearance height is then assumed to create proportional perturbations in axial velocity, circumferential velocity and pressure. Performing these substitutions and separating equations of different orders, after simplification, results in two zeroth-order momentum equations, for the axial and circumferential directions respectively; and three first-order equations, for continuity and axial and circumferential momentum. The zeroth-order equations become ordinary differential equations in nondimensional pressure and circumferential velocity as a function of axial position; for a straight smooth seal the axial velocity is constant. The zeroth-order momentum equations are solved by numerical iteration in conjunction with the boundary conditions. The coefficients of the first-order perturbation equations are dependent on the results of the zeroth-order equations.

The first-order equations are subsequently solved by defining the nondimensional clearance as a harmonic function dependent on the operating speed of the rotor and the amount of fluid whirl assumed [1]. These variables assume similar harmonic solutions with separation of variables techniques. The resulting six real harmonic equations are simplified to a system of three complex ordinary differential equations. The eccentricity of the spinning rotor, and thus the fluid in the seal, precesses around the nominal axis, accounting for the time dependence of the other perturbation variables [1, 31]. Application of homogeneous boundary conditions to the system of complex equations provides the reaction force components in

terms of precession frequency. Least-squares linear regression is then used to fit vibration coefficient matrices to data points generated by the solution of the first-order perturbation equations at multiple precession frequencies [1, 6].

2.3 Design of Experiments

Design of experiments is a branch of statistics concerned with getting the most information out of a minimum number of experiments. This is done by planning the experiments to span the design space efficiently based on the multifactor linear regression model which is selected to fit the data [32-34].

A classic example of DOE is a factorial design, invented by R. A. Fisher in response to the common misconception that to obtain information about the effect of a factor you must hold other factors in a given system at constant levels [26-28]. Instead, a 2^k factorial design not only allows variation of multiple factors at a time, but also allows for calculation of interaction effects between factors. Interaction between two factors occurs when the effect of one factor depends on the level of a second factor. A two-level factorial design in three factors, shown in Figure 2.4, has design points at each corner of a cube in the three-dimensional design space. This design has 2^3, or 8, experiments.
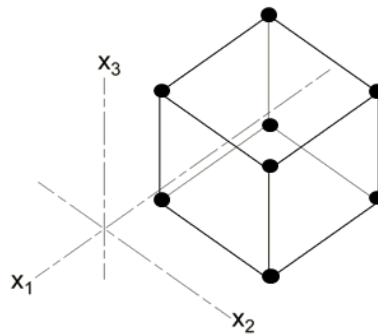
Figure 2.4: 2^3 Factorial Design

An empirical linear regression model to fit results from a 2^3 design might contain three first-order parameters, three two-factor interactions, and an intercept parameter, as shown here:

$$y = \beta_0 + \beta_1 x_1 + \beta_2 x_2 + \beta_3 x_3 + \beta_{12} x_1 x_2$$
$$+\beta_{13} x_1 x_3 + \beta_{23} x_2 x_3 + r \qquad (11)$$

where y is the response being modeled, the x's are the three design factors, and the β's represent the linear parameters estimating each factor effect, or interactions between factors, that define the model. Each experiment in the design provides a degree of freedom (df) for estimating a parameter, thus the 2^3 design has eight total degrees of freedom. With seven parameters in the model, only one degree of freedom is left for estimating residuals (r). Residuals have two sources: lack of fit of the model, and experimental uncertainty. Experiments at additional factor levels provide degrees of freedom for estimating the lack of fit of the model; replicate experiments at previous factor combinations provide degrees of freedom for estimating experimental uncertainty [34, 35]. However, the number of experiments in a factorial design increases exponentially with an increase in the number of factor levels. Thus, typically, few factor levels are used, or fractional factorial designs may be employed [32, 34, 36, 37]. A fractional factorial design incorporates a fraction, usually a negative power of the number of factor levels, of the experimental points in a full factorial design. For example, a 2^{5-2} is a ¼ fraction of a 2^5 factorial design having 8 design points instead of 32. As previously stated, it is only necessary to have more degrees of freedom from performing experiments than the number of parameters in the regression model. However, if only a subset of the experiments in

the full factorial design are performed, some factor interaction effects may be confounded with each other. Confounding means that certain factor effects are indistinguishable from each other. Specific fractional factorial designs, such as the many Placket-Burman designs, exist to minimize the amount of confounding or limit confounding to higher order factor effects, but are not employed herein [32, 34, 38].

Performing experiments at only two levels of each factor does not permit estimation of quadratic, or higher-order, factor effects. To offset this deficiency and still remain relatively efficient for experiments with few factors, the two level factorial design can be combined with a "star" design to make a Box-Wilson "central composite" design, as shown in Figure 2.5 [32, 34, 39]. The star design is a three level design that consists of a central design point around which additional design points are defined by varying one factor at a time to high and low values. The central composite design provides five levels for each factor, enabling the fitting of a model that includes linear effects, quadratic effects, and interaction effects between factors (Equation 12). The resulting empirical equation may be seen to be the equivalent of the first few terms of a Taylor expansion.

$$y = \beta_0 + \beta_1 x_1 + \beta_2 x_2 + \beta_{11} x_1^2 + \beta_{22} x_2^2 + \beta_{12} x_1 x_2 + r \tag{12}$$
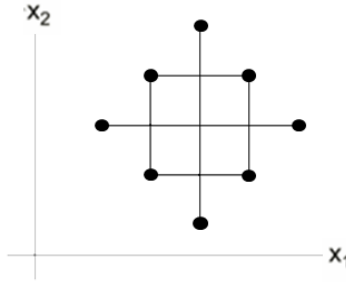
Figure 2.5: Central Composite Design in Two Factors

Factor levels for a central composite design are commonly selected by first choosing the center point and the levels representing the factorial design. These factor levels are coded in terms of an alpha value at -1, 0, and 1. The levels of the star's end points are then selected either by some overriding practical concern or to conform to convention. Three common conventions are (1) to select this alpha for rotatability of the design, (2) to obtain a spherical design, or (3) to obtain a face-centered design [32, 34]. A rotatable design is defined by the variation in response prediction being constant as the design is rotated around the center point at a constant radius. The coded factor level or alpha associated with a rotatable design is calculated by Equation 13. A spherical design indicates that the design points will all lie on the surface of a sphere centered at the central design point, and a face-centered central composite design has only three levels, with the star design's end points centered on the face of each factorial square. Selection of these levels is dependent on the goals of the design and the limitations of the design space.

$$\alpha_{star} = (Number\ of\ Factorial\ Design\ Points)^{1/4} \qquad (13)$$

2.4 Hierarchical Multiple Regression Model Fitting

Multifactor least-squares linear regression analysis was applied to the results of each designed experiment using *Design Expert v.6* (Stat-Ease, Minneapolis, MN). There are several widely accepted statistics that evaluate the quality of a regression model. The most common is the coefficient of determination, R^2, which has values between 0 and 1 and describes the fraction of the variation in the data about its mean that is accounted for by the parameters of the regression model. Because of how it is calculated the coefficient of determination always increases with the addition of terms to the model, until the number of parameters matches the number of experiments and R^2 equals one [34, 35]. Thus, while R^2 represents an important and easily understood metric of model quality, it is not sufficient. In addition to the coefficient of determination, an "adjusted" and "predicted" coefficient of determination are used in this work in conjunction with F-tests based on analysis of variance (ANOVA) of the individual parameter estimates and various graphical methods to select and provide for a judgment of the adequacy of the fitted regression models. It should be noted that a standard F-test for lack-of-fit of the model to the data is excluded in the present situation due to the lack of replicate experiments (experiments at the same factor levels that provide an estimate of experimental uncertainty). No replicate simulation experiments were performed because the CFD simulation converges to the same solution every time when given a set number of iterations and a consistent initial value.

The adjusted R^2 offsets inflation of the coefficient of determination by comparing the number of parameters used in the model to the number of experiments [35]. The adjusted R^2 is

always less than the standard R^2, and decreases as additional parameters are added to the model that do not also proportionally increase the correlation between model and data. The predicted R^2 is calculated by removing one point at a time from the data set, refitting the regression model and predicting the response of the omitted point. The residual differences between the measured responses and the cross-validated predictions are then used to calculate the predicted R^2 [35]. Again, the predicted R^2 value is always less than the standard R^2 and decreases as additional parameters are added to the model that do not also improve prediction of the response. Ideally, all three coefficients of determination are approximately equal to indicate a good model. However, both the adjusted and predicted R^2 values can be negative, indicating that the regression model fails to explain more variation in the observed data than a simple average [35].

Further validation of the fitted model can be achieved by using F-tests to determine the statistical significance of each single model parameter by calculating the ratio of the parameter estimate to its standard error. This approach is equivalent to calculating the confidence interval for each parameter to determine if it is significantly different from zero at a stated level of confidence (e.g., 95%). For the hypothesis test that a parameter is not significantly different from zero, a p-value can be derived that indicates the probability that the outcome for that parameter occurred by chance. Statistical confidence level can be stated as the probability that the outcome did not occur by chance. Thus, p-values less than 0.05 are consistent with the 95% confidence interval for not containing zero and the parameter estimate being different from zero at or above the 95% level of confidence. [32-35].

The coefficients of determination and individual parameter ANOVA are used to judge the fit of a particular regression model, but do not give an indication of what model to begin with. Instead, the method of sequential sum of squares is applied [35]. Beginning with only the regression model's intercept parameter, additional parameters are added to a model in hierarchical groupings provided that sufficient experiments have been performed at multiple factor levels. The change in residual sum of squares is then weighted by the additional experimental degrees of freedom consumed by the new parameters and can be tested for significance at the desired confidence level. Analogously, a combined F-test statistic could be calculated to determine the level of confidence at which the additional parameters are collectively different from zero. For example, if the mean and first-order factor effects are found to be significant, then the first-order two factor interaction effects might be evaluated for inclusion in the model, followed by second order factor effects and second-order (two-factor) interactions, cubic effects and three-factor interaction effects, and so on. Sequential sum of squares analysis describing the modelling power of these added parameters is then used to infer the order of model complexity best suited to the data. The other metrics of model quality may then be used to provide the basis for judging the tradeoff between model complexity and adequacy of prediction.

For example, these metrics may indicate that a quadratic regression model explains slightly more variation in the data about its mean, but fails the sequential sum of squares F-test for increased significance over a linear, or first-order factor effect, model. Parameters that are not significantly different from zero at the desired confidence level (say, 95%) are removed to

27

improve the model's balance of parameters [34, 35]. Occasionally, it is desirable to leave terms in the model that are not individually found significant if there is a physical justification based on the experiment or if they preserve the model hierarchy. For example, if a second order factor effect is found significant the associated first-order factor effect should be included regardless of significance. However the first-order interaction effects associated with it need not be included if found insignificant. This allows the regression model to be refined on a term by term basis to include only, or at least primarily, statistically significant factor effects.

Additional qualitative tests of model quality can be demonstrated by various plots showing randomness of residual patterns. Plotting the actual response value against the predicted response value can demonstrate the fit and lack of bias of the model. Randomized residuals can be demonstrated by plotting the residuals against the actual or predicted response to validate the assumptions of least-squares regression [35].

The present work used the coefficients of determination and single parameter F-tests to select parameters to include in each regression model. The resulting regression models thus reflect only the factor effects that are statistically significant at a high level of confidence, allowing seal designers to ignore factor effects shown to be statistically insignificant.

CHAPTER 3: METHOD

This chapter covers the methodology used in this study. First was the selection of a baseline for the seal design. Multiple methods were examined to parameterize this initial design. The goal was to reduce the parameters to be varied while maintaining as much potential variation in the seal geometry as possible. Computational models were then created in ANSYS CFX, and multiple meshing schemes and densities were tested to balance computational expense and accuracy. As discussed in the next chapter, experimental designs were then selected and performed to evaluate the design parameters. Simulation data were processed using a hybrid bulk flow/CFD method and modeling by multiple least-squares regression. The resulting regression equations were used to map the design spaces and identify design points with minimum leakage rates.

3.1 Selection of Seal Model

The baseline seal CFD model for this investigation was selected from Untaroiu *et al.* [12]. The annular labyrinth seal is a sub component of the 8-stage pump, shown in Figure 1.1, and has a working fluid of water. The labyrinth seal was modeled as a five degree sector to decrease the time required to generate a well meshed model and the time to solve for the seal's flow properties. The fluid region of the seal is shown again below in Figure 3.1 with a highlighted cross section indicating where the five degree sector fits into the full 360° seal model. The five degree sector of the annular labyrinth seal, shown in Figure 3.2, consists of an inlet pre-swirl cavity feeding into the clearance region of the seal. The geometry of the seal itself consists of twenty parallel semi-circular grooves oriented perpendicular to the axis and evenly spaced

axially beginning 9.53 mm from the pre-swirl cavity and ending 9.53 mm before the seal's exit

boundary. This model was selected for the simplicity of its geometry and because it gives all of

the relevant dimensions and flow variables needed to recreate the seal. The flow variables of

the base seal model are listed in Table 1. It should be noted that the original seal was solved as

a full 360 degree model with eccentricity, whereas the fluid model used in the present study is

a five degree sector of an unperturbed seal. Also, the original seal model has specified inlet

velocity components. In combination with the fixed area of the inlet, this defines the flow rate

exactly as given by a mass conservation calculation. A boundary condition that fixes the flow

rate as constant would defeat the purpose of minimizing flow rate. So an inlet pressure was

specified based on the CFD results of Untaroiu, *et al.* [12].
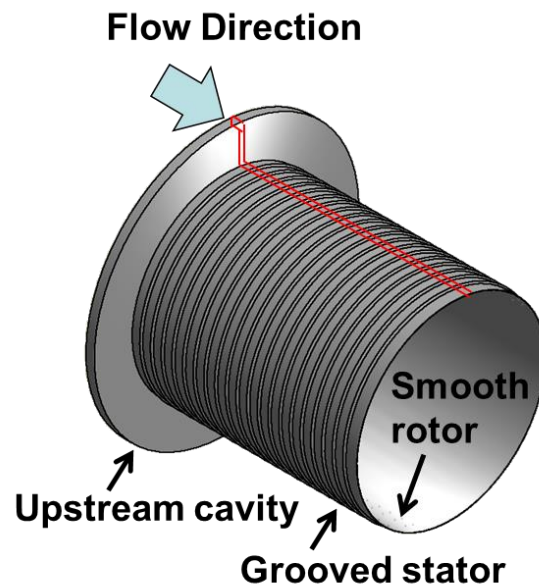
Figure 3.1: Labyrinth seal's fluid region with highlighted seal cross-section
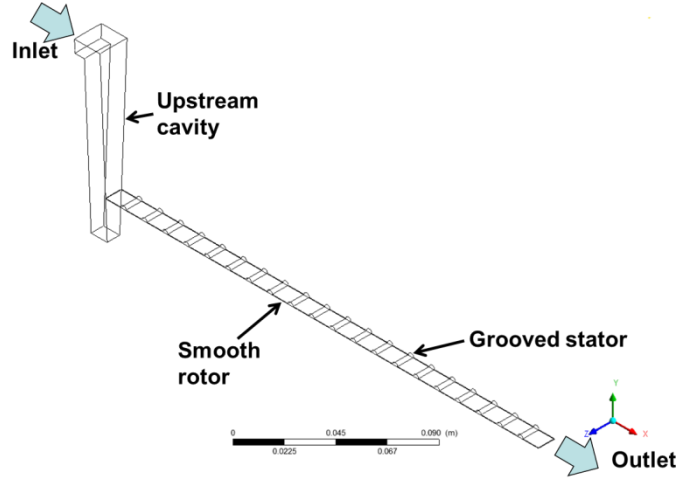
Figure 3.2: Baseline seal geometry, a 5° sector of the full seal

Table 3.1: Baseline seal geometry

L_S [mm]	D [mm]	c [mm]	N [-]	W [mm]	l_i, l_l [mm]	d [mm]
267	111.9	0.0305	20	3.18	9.53	1.59

3.2 Parameterization of Seal Model

The baseline annular labyrinth seal was modeled as a five degree sector model in ANSYS Design Modeler [40], shown in Figure 3.2. A five degree sector was chosen because ANSYS CFX is a 3-dimensional CFD solver. Rather than create a model of one element thickness, a five degree sector allows for potential refinement of the flow in the circumferential direction without as much added solution time as a larger sector or full 360 degree model. This baseline model was then modified to create two reduced parameter models. The first parameterization, shown in Figure 3.3, describes the seal with five factors representing sequential distinct seal groove radii that are repeated four times along the length of the seal. The landing between the grooves was calculated, based on the seal length and groove widths, to set each groove equidistant from each other, as given by Equation 14 and seen in Figure 3.4. This arbitrary

31

parameterization allows investigation of the effect of groove scale along the entire length of the groove without resorting to a 20-factor model to include each radius individually.
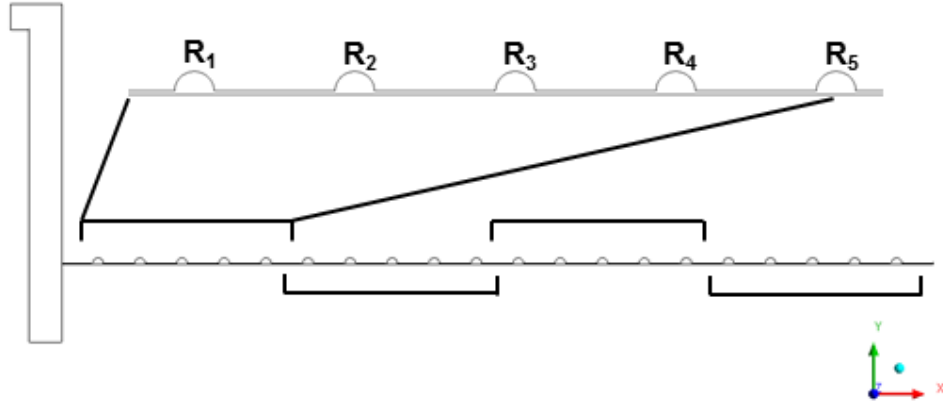
Figure 3.3: Parameterization of seal geometry
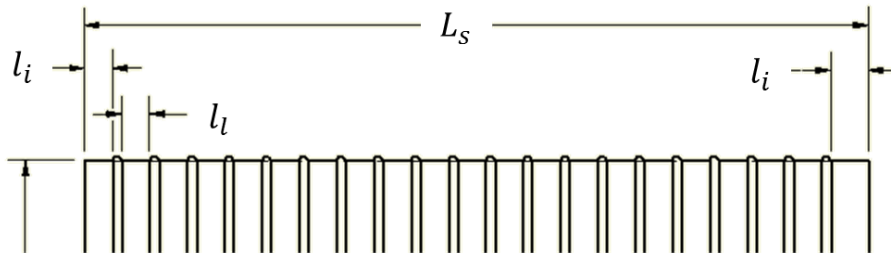
Figure 3.4: Groove axial spacing geometry along the seal

$$l_l = \frac{(L_s - 2l_i - 8\sum_j^5 R_j)}{19} \qquad (14)$$

This parameterization was chosen because a full parameterization, allowing the scale of each groove to vary independently, would consist of 20 parameters. The number of experiments necessary for obtaining information on quadratic and two factor interaction effects must be more than the number of parameters in the resulting linear regression equation, given by Equation 15 [34]. Here, p is the number of parameters and k is the number of factors. 20 factors would require a minimum of 231 experiments, but five factors only needs 21. This makes a study of five parameters much more computationally cost effective. Equation

16 shows the full linear regression model with R_n representing radius number n and r still representing the residuals between measured and predicted response of mass flow rate leakage through the seal (y).

$$p = \tfrac{1}{2}(k + 1)(k + 2) \tag{15}$$

$$\begin{aligned}
y = {} & \beta_0 + \beta_1 R_1 + \beta_{11} R_{11}^2 + \beta_2 R_2 + \beta_{22} R_{22}^2 + \beta_3 R_3 + \\
& \beta_{33} R_{33}^2 + \beta_4 R_4 + \beta_{44} R_{44}^2 + \beta_5 R_5 + \beta_{55} R_{55}^2 + \beta_{12} R_1 R_2 + \\
& \beta_{13} R_1 R_3 + \beta_{14} R_1 R_4 + \beta_{15} R_1 R_5 + \beta_{23} R_2 R_3 + \beta_{24} R_2 R_4 + \\
& \beta_{25} R_2 R_5 + \beta_{34} R_3 R_4 + \beta_{35} R_3 R_5 + \beta_{45} R_4 R_5 + r
\end{aligned} \tag{16}$$

The second parameterization, shown in Figure 3.5, repeats a single "flexible" groove geometry twenty times equally spaced along the length of the seal. The groove geometry is considered flexible because variations in the defining parameters describe a groove whose shape can vary smoothly between triangular, rectangular and semi-circular extremes. The flexible groove shape consists of a trapezoid defined by the groove's width, the width of the flat truncating the groove, the groove depth, and the entrance and exit angles. The radii within the groove cavity are equal to each other and dependent on the five design variables. The extremes are shown in Figure 3.6 through Figure 3.8, with the relevant geometric constraint for each extreme in Equations 17 through 19 below each respective figure. The second parameterization repeats the individual groove shape along the length of the seal because every additional independently variable shaped groove adds five more parameters to the model. Allowing each of the 20 grooves to have independent variable shapes would require at least 100 parameters even without additionally variable spacing between grooves. The parameterizations employed herein are only some of many options for a reduced parameter model. As with all such models,

the parameterization directly affects the meaning that can be derived from the results, and

subsequent simulations with different parameterizations are recommended by this author.
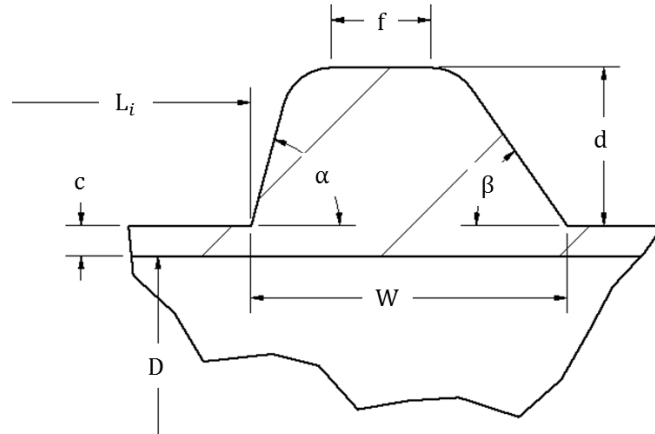
Figure 3.5: Second seal geometry parameterization example groove, intermediate shape
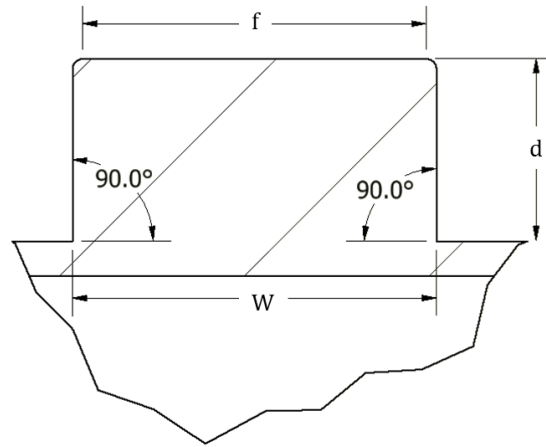
Figure 3.6: Maximum groove flat width constraint, rectangular groove extreme

$$\alpha < \frac{\pi}{2} \ (90°)$$

$$\beta < \frac{\pi}{2} \ (90°)$$

$$W - f \geq 0.01 \tag{17}$$
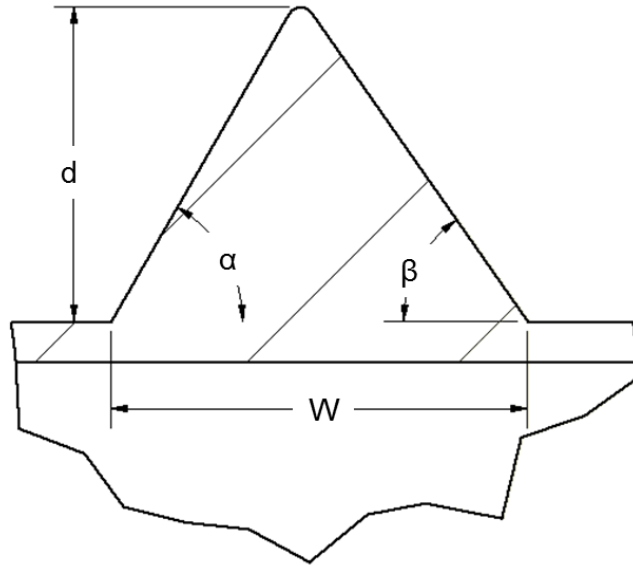
Figure 3.7: Maximum groove depth constraint, triangular groove extreme

$$d_{max} = (W - f)\frac{\sin\alpha \sin\beta}{\sin[\pi-\alpha-\beta]} \qquad (18)$$
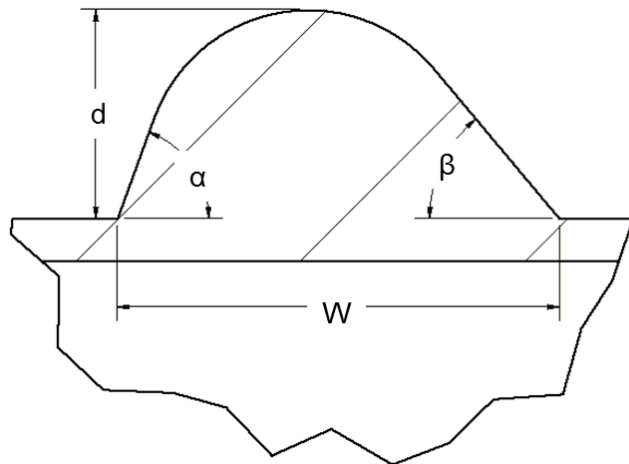
Figure 3.8: Minimum groove depth constraint, arced or semi-circular groove extreme
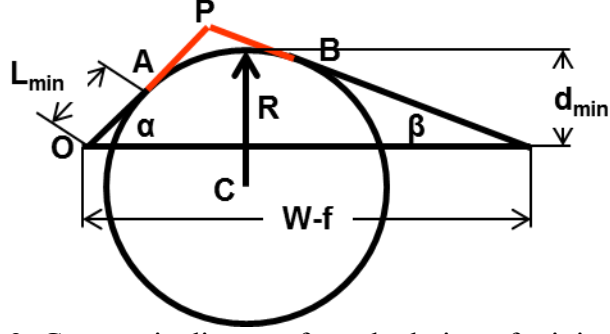
Figure 3.9: Geometric diagram for calculation of minimum depth

$$P_x = \frac{\tan(\beta)(W-f)}{\tan(\alpha)+\tan(\beta)} \qquad\qquad P_y = \frac{\tan(\alpha)\tan(\beta)(W-f)}{\tan(\alpha)+\tan(\beta)}$$

$$A_x = \mathrm{L}_{min}\cos\alpha \qquad\qquad A_y = \mathrm{L}_{min}\sin\alpha$$

$$|\overline{PA}| = \sqrt{(P_x - A_x)^2 + \left(P_y - A_y\right)^2}$$

$$R = \sqrt{|\overline{PA}|^2\,\frac{1-\cos(\pi-\alpha-\beta)}{1-\cos(\alpha+\beta)}}$$

$$d_{min} = A_y + R\left(1 - \sin\left(\frac{\pi}{2} - \alpha\right)\right)$$

$$\text{For } \alpha > \beta \text{ and } 0 \neq \tan\beta + \tan\frac{|\alpha-\beta|}{2} \qquad\qquad (19)$$

3.3 Mesh Generation and Dependence

The mesh for each model was generated automatically in ANSYS Workbench from a parameterized geometry file. The mesh was created with a sweep around the seal's axis, dividing the five degree sector into 30 equal segments circumferentially. The target face of the sweep method was selected as the radially sliced face to the right looking along the seal axis. Element sizing requirements were set for the target face and its boundaries to ensure quality mesh generation. The target face was then inflated along the edges that meet the rotor and stator surfaces respectively to increase the number of elements near the wall. The procedure of

36

applying inflation layers is required to capture more detailed boundary layer effects near the walls. A representative section of the mesh is shown in Figure 3.10.
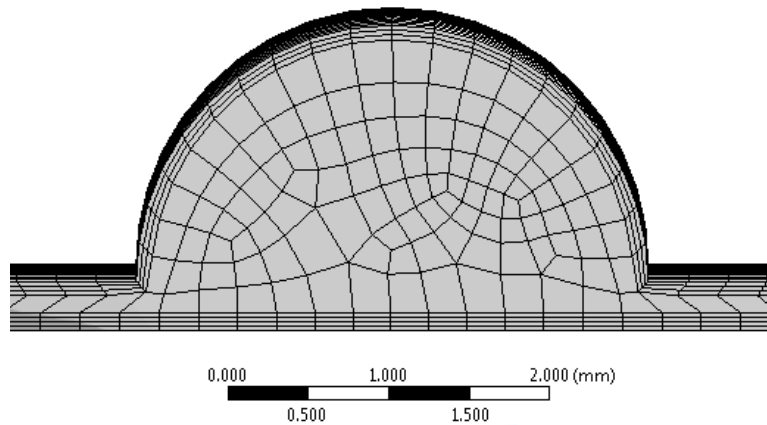
Figure 3.10: First parameterization seal groove mesh

The base model, with all radii equal to 1.59 mm, was simulated with multiple meshes of decreasing mesh element density until the resulting flow properties deviated from the simulations performed with higher mesh densities. Meshes with element densities of about 2.5 million elements down to 570,000 elements were tested. The pressure profile along the length of the seal, Figure 3.11, is qualitatively the same for every simulation. Similarly, the axial velocity profile is qualitatively the same for each mesh density simulation, Figure 3.12. Qualitatively and quantitatively there is no consistent distinction between the flow variables for the different mesh densities. The median density was chosen to balance potential increased accuracy with computing time constraints.
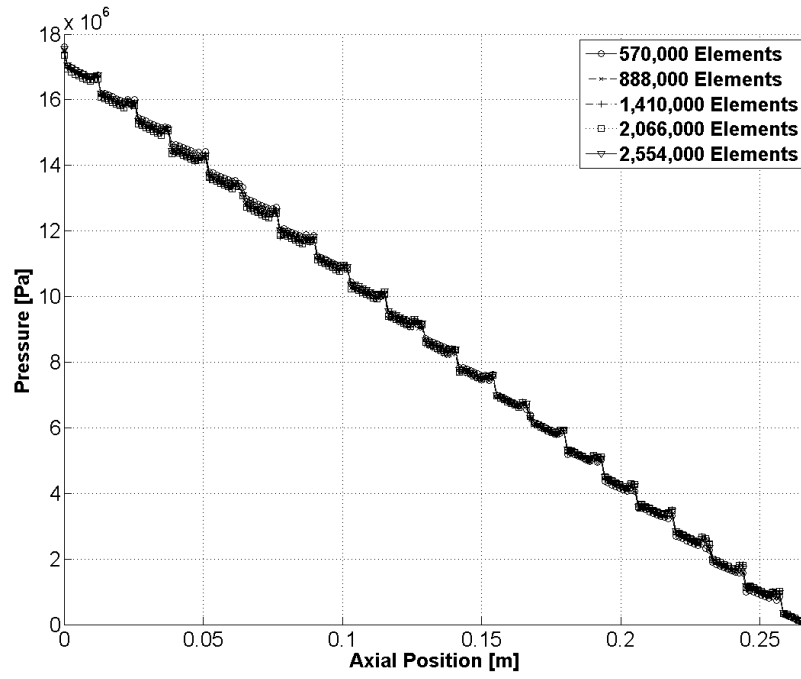
Figure 3.11: Pressure profile mesh dependence
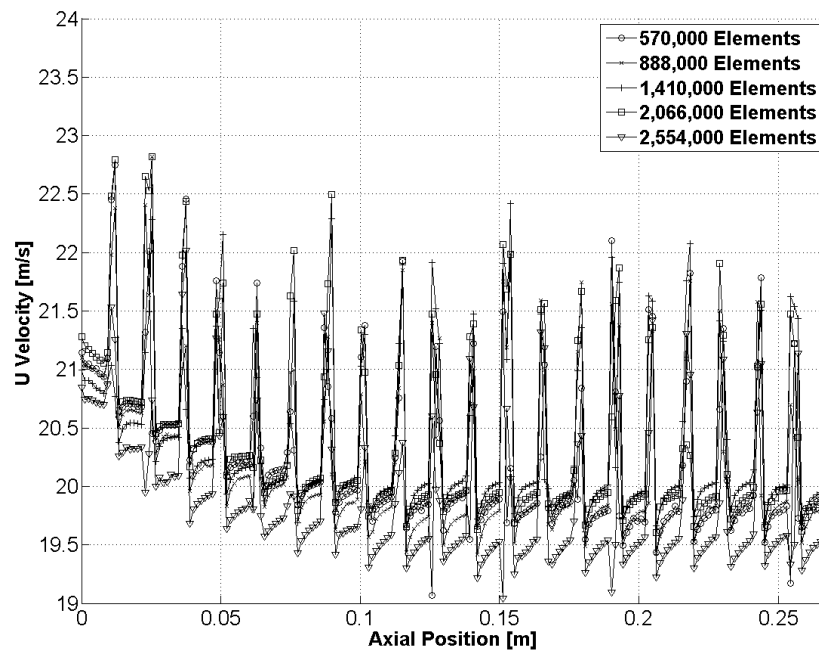
Figure 3.12: Axial velocity profile mesh dependence

For the second parameterization models, a mesh of approximately the same element density (1,538,910 Elements) was created for geometry of the nominal size, as defined by comparison with the base model of parameterization one. This mesh was also swept, however the 2D mesh of the target face was defined differently than that of the first parameterization. Instead of dividing each edge into a fixed number of equal segments, the software was set to automatically generate a new mesh with elements of an approximate size that was specified for each edge. This will result in a larger increase in the number of mesh elements for larger groove geometries. This is necessary because of inconsistent relative sizes of each edge that defines the groove shape. An example of the mesh for a groove defined with the second parameterization is shown in Figure 3.13.
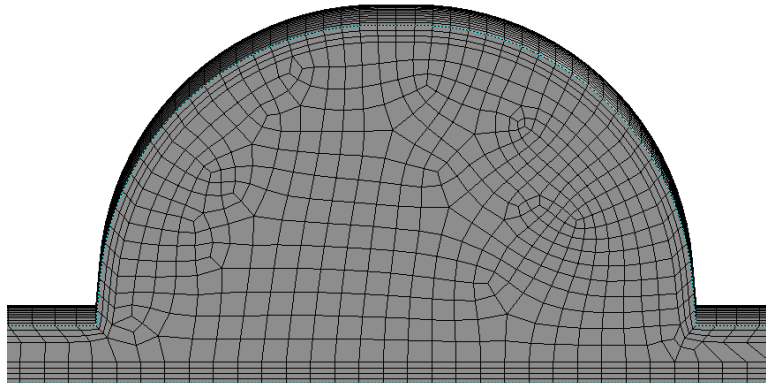
Figure 3.13: Second parameterization seal groove mesh

3.4 CFD Simulation Definition

CFD simulations were performed with ANSYS CFX version 13.0 and 14.0. This commercial software solves the Reynolds averaged Navier-Stokes equations in discrete volumes defined by the mesh of a fluid model. Conservation equations for mass and momentum were applied to each element. The working fluid of the domain was set to be water at 25C. Water

was not expected to change temperature significantly along the length of the seal so the energy equation was omitted. A standard k-ε model was used to resolve turbulence within the seal [13]. The domain was set to be rotating at 3500 RPM about the axis of the seal and the rotor surface was defined as a no-slip wall at rest relative to the domain. A counter rotating no-slip wall boundary condition was applied to the stator surface of the seal. The inlet boundary was defined by a static pressure of 18.575 MPa which corresponds to the pressure drop across the base seal [12]. The flow was specified to be normal to the inlet boundary for a zero pre-swirl flow. Turbulence was set to 5%, or medium intensity, at the inlet and initially throughout the seal. The outlet was set to an average relative, or gauge, static pressure of zero and a blend of 5%. The left and right walls of the seal were defined with a fluid-fluid interface as rotationally periodic boundaries about the axis of the seal. The rotational periodic boundary condition specifies the solution at one interface to be a phase shifted periodic function of the other interface. The simulation was judged to be converged when the mass flow rate remained steady for 300 iterations and the RMS residuals of the Reynolds Averaged Navier-Stokes (RANS) equations reached or fell below values of 10^{-6}. Comparison of the leakage rates between the five degree seal sector model herein and the full 360° seal model simulated by Untaroiu, et al. [40] show that this study's CFD results predict higher leakage rates for the same seal groove geometry. It is assumed that the discrepancy in leakage rate can be explained by the lack of eccentricity in the five degree sector model and lack of prescribed pre-swirl at the inlet. As long as leakage rates for this study are accurate relative to each other, the absolute leakage value is

not relevant, because the same trends associating the geometric factors to the leakage rate response will apply.

3.5 Hybrid Bulk Flow/CFD for Labyrinth Seals

The hybrid bulk flow/CFD method of analysis for annular fluid seals was developed by Migliorini, *et al*. [4]. In this method, a circumferential sector of the full three dimensional seal is analyized using steady state CFD simulations at the nominal clearance of the seal, without rotor eccentricity. The resulting average flow properties and wall shear stresses from the CFD model are taken at 200 locations in the clearance region along the axial length of the seal. The values at these nodes are used in place of the solution to the zeroth-order perturbation of the governing bulk flow equations for a straight and smooth annular seal. This approach has been shown to increase significantly the accuracy of the subsequent bulk flow solutions for the rotordynamic coefficients of the seal over a standard bulk flow analysis. These increases in accuracy also increase the solution time of the entire analysis, however the process is much faster than running an equivilant CFD analysis on multiple full seal models at different whirl speeds. Though originally applied to hole pattern seal geometries, the method is not constrained to any particular seal geometry because the specific geometry of the seal in question is taken into account by the zeroth order solution values provided by the CFD simulation. This hybrid method was employed herein to allow calculation of rotordynamic coefficients for the 187 distinct seal geometries tested in this study. Performing a more traditional CFD simulation of the full seal model at multiple whirl speeds for each geometry would have required a minimum 600% increase in computational time.

3.6 Optimization Techniques

Design space parameters yielding minimum leakage rate were found by running numerical optimization of the predicted least-squares multiple regression equations obtained from each design of experiments cycle. Two distinct methods were used according to the complexity of the regression equation fit to the data. For the first parameterization, the leakage was modeled with a simplified quadratic equation. Without interaction of factor effects and no geometric constraints to consider, an analytical approach to optimization was possible. Also conveniently, the quadratic parabola was concave. The second derivative of the regression equation is positive, so minimum factor values could be obtained by taking the first derivative with respect to each factor and setting it equal to zero.

For more complex regression equations and seal geometries, such as the second parameterization, the interaction of factor effects and the presence of nonlinear geometric constraints prevent the analytical approach to optimization. A nonlinear optimization tool in Matlab 2012a was used to perform the optimization procedure on the multiple regression equation. The function **fmincon** finds minima of constrained nonlinear multivariable functions of generalized form [41]. Despite the regression equation being linear, the function was selected for its ability to accommodate the nonlinear geometric constraints imposed by the second parameterization, see Equations 17 through 19 above. The **fmincon** function can apply one of four distinct optimization algorithms [41]. The optimization algorithm selected for this application was "active-set"; this algorithm is not the fastest algorithm, but has the advantage of being capable of taking larger iterative steps which can be useful when the constraints are

less smooth. This algorithm employs the "sequential quadratic programing" (SQP) method [41]. All optimization methods are subject to becoming stuck around a local minimum of the objective function. To avoid this, the optimization function was initialized with 500 design points randomly generated between the extreme allowed values of each factor, and the design point with the overall minimum leakage among the resulting local minima was selected as the global optimum.

It should be noted that the above optimization procedures only reflect the true optimum design points as much as the leakage rates obtained from the multiple regression equations reflect the true leakage rate of a particular labyrinth seal geometry. No attempts were made to optimize the seal geometry parameterizations for any other objective function. None of the rotordynamic coefficients have objectives that would apply universally to any turbomachine assembly.

CHAPTER 4: DESIGN OF EXPERIMENTS – ITERATION AND RESULTS

The goal of a designed experiment is to maximize the amount of information obtained to describe a given response using a minimum number of experiments. This study selected experimental designs for simulation experiments, in conjunction with the parameterizations, to explore as much of the design space for seal geometry as possible. The resulting data were analyzed by multiple least-squares regression to obtain empirical maps to guide seal geometry design. Thus, simulation outcomes from a set of systematically perturbed seal design parameters were applied to find and verify seal geometries that have minimal leakage rates. The design points and responses for each experimental design are tabulated in Appendices A and B respectively.

4.1 First Parameterization Experimental Design

A non-central composite design was selected to explore the design space of the first parameterization. The non-central composite design differs from a central composite design in that the star design, previously discussed with Figure 2.5, is not centered within the design points of the factorial design. The five levels of each factor for the experimental designs are the same, as they each represent the scale of a groove radius. The radius was allowed to vary from 25% to 300% compared to the nominal base model. The levels of groove radius were 0.3975 mm, 0.99375 mm, 1.59 mm, 3.18 mm, and 4.77 mm. The center of the star design was at 1.59 mm for all factors. These factor levels were selected to combine the assumption that the base seal design from industry was near the optimal geometry with the desire to explore a broader design space.

A model, parameterized using five design variables representing a pattern of groove radial scales along the axial length of the seal, was simulated in ANSYS CFX. Forty-three simulated experiments characterized the leakage rate response of the seal resulting from variations in the parameterized groove radii. All steady-state simulations were started from the same initial conditions in a rotating reference frame. The fluid domain was initialized by the results from the previously performed mesh density study of seal sector model with radii at the nominal dimension of 1.59mm. No replicate experiments were performed, for any experimental design, because ANSYS CFX will reach the same results every time for a given solution residual level and starting position. Hierarchical multiple regression analysis was conducted for each of the desired response variables representing fluid leakage rate through the seal and the rotordynamic coefficients. Analysis of variance (ANOVA) was performed on each fitted model to generate the coefficient of determination, R^2, the F-test for significance of regression (testing the null hypothesis that all factors effects were zero), and single parameter F-tests to find the significance level at which to reject null hypothesis that each parameter is equal to zero [10, 11].

4.1.1 First Experimental Design Results and Discussion

A full quadratic 21-parameter linear regression model was initially proposed to describe the design space for each response. The quadratic model was selected as the minimum level of complexity that could allow prediction of a local optimum and as a model that minimizes aliasing of higher order effects with the effects included in the model. This full quadratic model was found not to best describe the data. The linear regression model was reduced from the full

quadratic to include only factor effects found to be statistically significant, or those necessary to maintain model hierarchy. A cubic model was not considered, for this experimental design, because the chosen design points alias cubic factor effects with higher order terms. Tabulated statistical results are shown in the next section for the first regression analysis; these tables are representative of the statistical results for the subsequent response variables.

4.1.1.a Leakage Rate

For the mass flow leakage response, the linear regression model was reduced to 11 parameters. Figure 4.1, shows the Pareto chart of the relative significance of the factor effects, for the original 21-parameter regression model, based on the sum of squares associated with each parameter [35]. In the Pareto chart, the sum of squares for all of the two factor interaction effects, except the AB interaction relating radii 1 and 2, are significantly smaller than the sum of squares for the first-order and quadratic factor effects. ANOVA was performed on the full quadratic regression model, and the same nine two-factor interaction effects also fail to reject the null hypothesis that their parameters are equal to zero, based on the single parameter F-tests for significance (p-value>0.05). These non-significant interaction factor effects were removed from the regression model. The factor effect AB, representing the interaction between the first and second groove radius in the parameterization pattern, was also removed as there should be no physical mechanism that would cause it to be different from the other interaction effects.
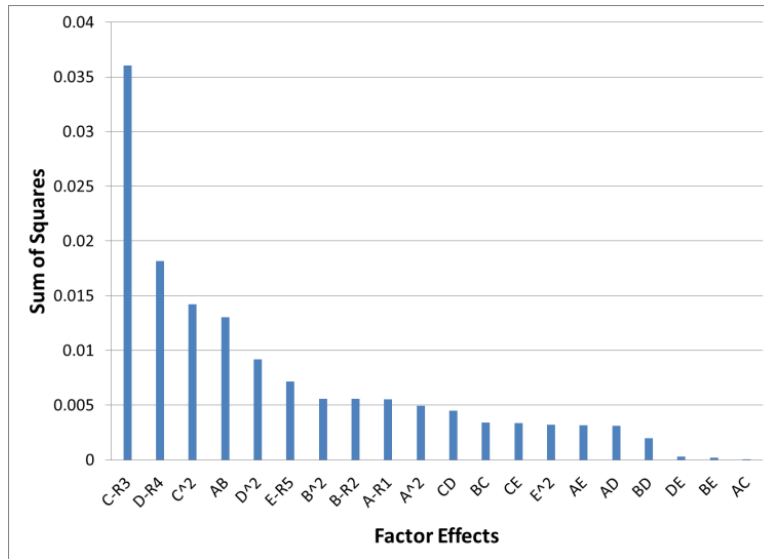
Figure 4.1: Pareto chart showing relative factor effects
based on explained sums of squares of variation

The resulting 11-parameter reduced quadratic regression model included the intercept parameter and the first and second-order single factor effect parameters. ANOVA performed on the model produced an R^2 value of 0.9015, implying a strong linear correlation between the model and the data. The F-test for significance of the regression model rejected the null hypothesis that all parameters are zero at better than 95% confidence and produced an F-value of 29.3 which, with an associated p-value of 0.0001, indicates only a 0.01% chance that an F-value that large could arise from noise in the data. Parameters representing first-order factor effects of each radius individually rejected the null hypothesis that they were equal to zero at or above the 95% level of confidence. The quadratic factor effect parameter for R_3 failed to reject the 95% confidence level hypothesis at a p-value of 0.0731 (i.e., significantly different from zero at only the 92.69% level of confidence). Quadratic factor effects for parameters R_1, R_2, and R_4 have more modest confidence levels ranging from 86.8% to 88.6% with associated p-vales found in Table 4.1. The quadratic factor effect for R_5 only has a confidence level of 69%,

47

but is retained to preserve model hierarchy. Thus, all the parameters of the first-order factor effects and the quadratic effects of the first four radii are significant at or above the 86.8% confidence level. These p-values and the remaining results of the ANOVA are found in Table 4.1.

Table 4.1: ANOVA Results

Source	Sum of Squares	df	Mean Square	Calculated Value of F	p-value Prob > F
Model	0.93	10	0.093	29.3	< 0.0001
A-R1	0.025	1	0.025	7.81	0.0087
B-R2	0.025	1	0.025	7.84	0.0086
C-R3	0.035	1	0.035	11	0.0023
D-R4	0.022	1	0.022	6.9	0.0131
E-R5	0.014	1	0.014	4.33	0.0456
A^2	7.62E-03	1	7.62E-03	2.39	0.1316
B^2	8.42E-03	1	8.42E-03	2.65	0.1136
C^2	0.011	1	0.011	3.43	0.0731
D^2	8.05E-03	1	8.05E-03	2.53	0.1216
E^2	3.42E-03	1	3.42E-03	1.07	0.3076
Residual	0.1	32	3.18E-03		
Corrected Total	1.03	42			

The sum of squares of residuals cannot be split into lack of fit and purely experimental uncertainty because no replicate experiments were included. However, CFD simulations with the same mesh and started from the same initial values will converge to the same result for a given convergence criteria. This makes the experimental uncertainty effectively zero. Without sum of squares of residuals for a formal lack of fit test, evidence of model quality can be demonstrated with plots of normalized residuals against predicted response and predicted response against actual response. Figure 4.2, shows randomly distributed residuals above and below zero without systematic bias, thus suggesting the model cannot be further improved.

Figure 4.3, shows a linear relationship between predicted and actual values of response, also indicating no significant model bias due to lack of fit. In these figures, the actual values refer to the results obtained from the CFD simulations and the predicted values refer to the values estimated from the empirical model. Parameter estimates and their standard errors are given in Table 4.2, and the resulting model is shown in Equation 20.

$$Q = 9.88 - 0.13R_1 + 0.016R_1^2 - 0.13R_2 + 0.017R_2^2 - 0.16R_3 + 0.019R_3^2$$
$$-0.12R_4 + 0.017R_4^2 - 0.10R_5 + 0.011R_5^2 \qquad (20)$$

Table 4.2: Parameter estimates and standard errors

Factor	Parameter Estimate	Standard Error	95% CI Low	95% CI High
Intercept	9.878	0.140	9.592	10.163
A-R1	-0.132	0.0474	0.229	0.0359
B-R2	-0.133	0.0474	0.229	0.0362
C-R3	-0.157	0.0474	0.254	0.0607
D-R4	-0.125	0.0474	0.221	0.0280
E-R5	-0.0986	0.0474	0.195	0.00206
A^2	0.0162	1.04E-02	0.00511	3.75E-02
B^2	1.70E-02	1.04E-02	0.00428	0.0383
C^2	1.94E-02	1.04E-02	1.92E-03	0.0406
D^2	1.66E-02	1.04E-02	0.00467	3.79E-02
E^2	1.08E-02	1.04E-02	-1.05E-02	0.0321
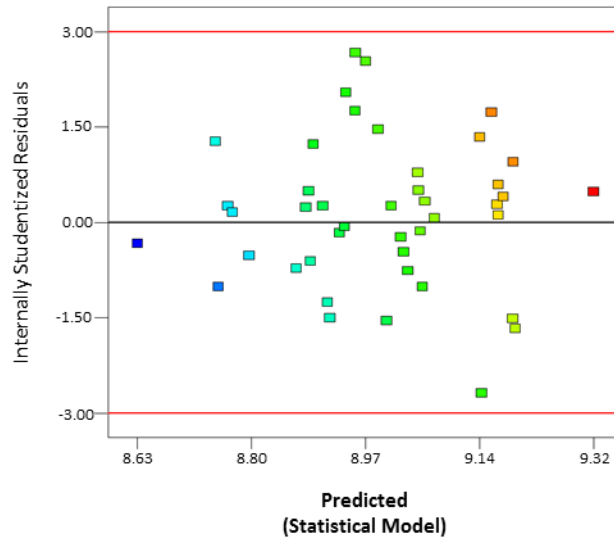
Figure 4.2: Residuals vs. predicted response
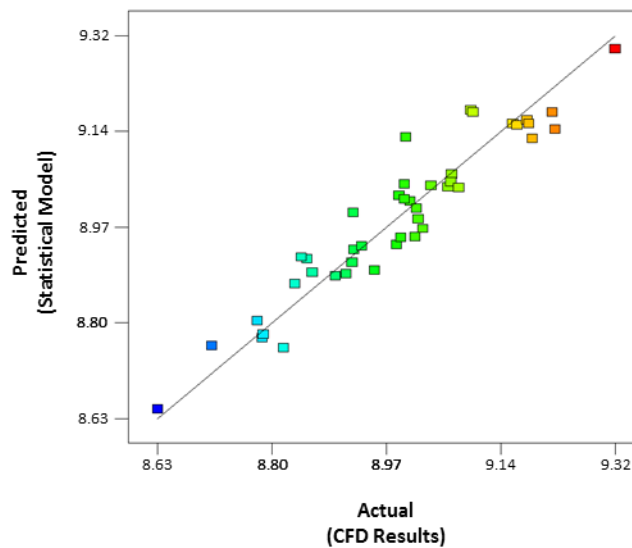
Figure 4.3: Predicted vs. actual response

Visualizations of the design space are shown in Figure 4.4 and Figure 4.5. The response surface looks similar from the perspective of the factors not shown. Factors kept constant are shown centered on the optimum response predicted by the regression model. The predicted optimum occurs at radii of 4.10, 3.91, 4.06, 3.75, and 4.55 mm for the design factors respectively, Figure 4.6. The predicted mass flow rate is 8.57 kg/sec, an 8.25% improvement

over the highest flow rate simulated, 9.34 kg/s, and 0.54% improvement from the lowest, 8.62 kg/s. The predicted minimum flow rate in this design space is also 5.58% improved over the leakage of the sector representing the base model, all radii set to 1.59 mm. The response surfaces suggest reduced leakage rates as the radii are increased. The model indicates that increasing a single groove radius lowers flow rate by an average 0.129 kg/s per mm of radius, but the square of the radius raises flow rate by an average 0.0160 kg/s per mm^2. The Pareto chart, Figure 4.1, suggests that the third parameterized groove radius has a larger effect on leakage rate than the other radii. However, the parameters for each radius are approximately the same suggesting that all radii affect the response equally. Any indication of an individual radius being more significant is likely a function of this parameterization rather than evidence of a physical mechanism at work. The removal of interaction factor effects from the model suggests that no specific pattern of varying groove radii would yield a significant decrease in leakage rate. The effect of each groove is individual and distinct from its neighbors. Because flow only travels from high pressure to low pressure through the seal this result makes sense.
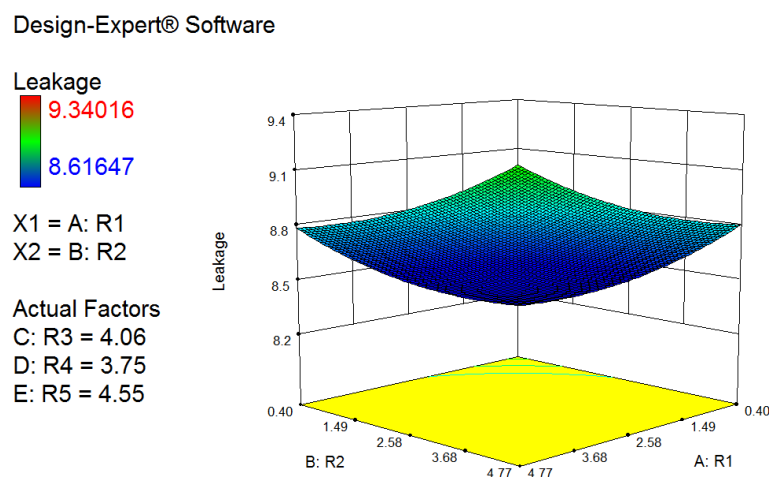
Figure 4.4: Response surface of fluid leakage rate vs. R$_1$ and R$_2$

Leakage
9.34016

8.61647

X1 = A: R1
X2 = C: R3

Actual Factors
B: R2 = 3.91
D: R4 = 3.75
E: R5 = 4.55
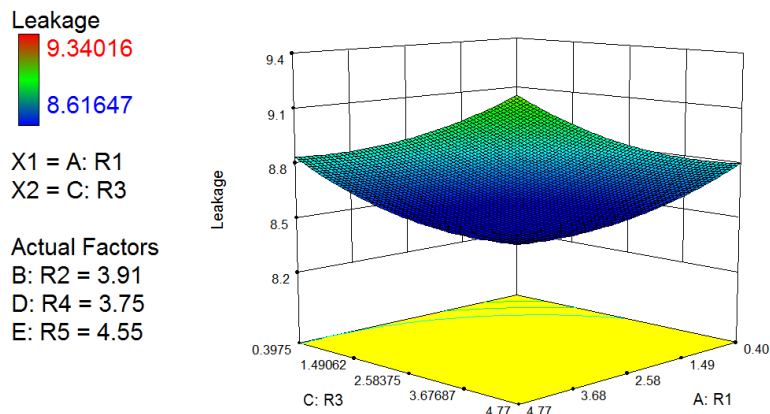
Figure 4.5: Response surface of fluid leakage rate vs. R_1 and R_3
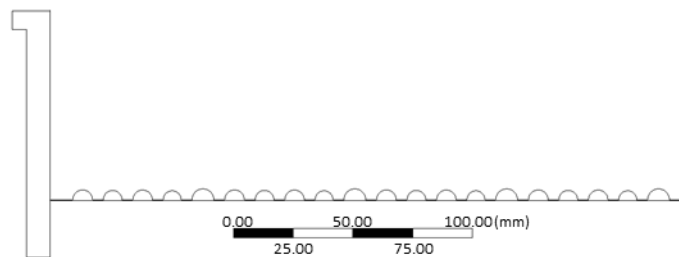
Figure 4.6: Design point geometry for predicted optimal leakage rate
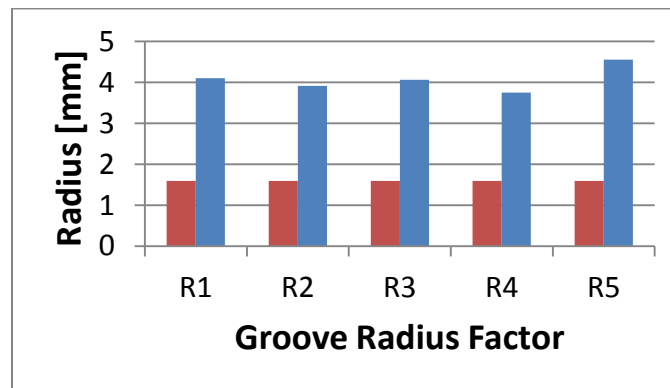
Figure 4.7: Radii of grooves for
base model (left) vs. optimal design point (right)

4.1.1.b Rotordynamic Coefficients

A quadratic regression model was not found to adequately model the data for any of the rotor dynamic coefficients. The responses of cross-coupled stiffness and direct damping coefficients were found to exhibit strong linear correlation with a simple 6-parameter first-order model. Coefficients for direct stiffness and direct mass are also best represented by a 6-parameter model, but display weaker correlations with the data. The remaining two coefficients for cross-coupled damping and cross coupled mass terms display no significant linear correlation. These responses are discussed individually below, except for those relating to the cross-coupled mass coefficient which would duplicate the explanation of the cross-coupled damping coefficient. With only first-order factor effect models and no universal target for the rotordynamic coefficients there is no reason to attempt optimization of these responses.

Direct Stiffness Coefficient

The sequential sum of squares F-test failed to find that a full quadratic model, or a two factor interaction model, explained the variation in the data better than the first-order factor effect model. Additionally, ANOVA for the parameters of a full quadratic model failed to reject the null hypothesis that the parameters representing first-order interaction effects were equal to zero, at the 90% confidence level. Upon removing the interaction effects and testing first and second order factor effect, as in the above leakage model, three second-order factor effects were found significant at or above the 90% confidence level. Unfortunately, the first and second-order factor effect model's predicted R^2 was -0.61, which indicates poor linear correlation and prediction ability of the model.

When second-order factor effects were removed, the resulting 6-parameter model included an intercept parameter and the first-order factor effects. Interestingly, ANOVA showed that not all of the first-order factor effects were significant either. Only radii 3 and 5 first-order effects were significant at or above the 90% confidence interval. The 3-parameter model, Equation 21, including the intercept and the R3 and R5 factor effects only explains 28.68% of the variation in the data based on the R^2. The diagnostic plots qualitatively confirm the assumption of linearity and the weak correlation between actual simulated response and the model predictions.

$$K_{XX} = 2.013 \times 10^7 - 1.086 \times 10^5 (R_3) - 2.172 \times 10^5 (R_5) \tag{21}$$

Clearly this parameterization of the seal geometry is not adequate to show the true relationship between direct stiffness and groove size, if any. The parameter estimates for R3 and R5 factor effects indicate that the stiffness decreases with increasing radii at an average rate of 1.5×10^5 N/m per millimeter for those grooves. The lack of significance of radii 1, 2 and 4 suggest that if groove scale is significant at all it may be related to groove axial position along the length of the seal.

Cross-coupled Stiffness Coefficient

The sequential sum of squares F-test found a first-order factor effect model for cross-coupled stiffness to be more descriptive than the mean at a 99.99% confidence level. The full quadratic model and two factor interaction models both failed to improve the model with p-values of 0.8391 and 0.9582. This means that there is only a 16% and 4% confidence that the interaction and second-order effect parameters are significant. Predictably, ANOVA performed

on the full quadratic model found no terms hierarchically higher than the first-order factor effects to be significant, while every first-order factor effect was found significant at better than 99.99% confidence. This results in a 6-parameter regression model, with parameter estimates shown in Equation 22, having an R^2 of 0.94. Adjusted and predicted R^2 values of 0.93 and 0.92, respectively, further demonstrates great linear correlation.

$$K_{XY} = 5.39 \times 10^8 + 9.60 \times 10^6(R_1) + 1.01 \times 10^7(R_2)$$
$$+9.97 \times 10^6(R_3) + 7.73 \times 10^6(R_4) + 9.61 \times 10^6(R_5) \tag{22}$$

The general trend is that increased groove size increases the cross-coupled stiffness by an average of approximately 9.4×10^6 N/m per millimeter. The individual parameter estimates are not equal at a glance, however their error margins are sufficiently overlapping that more data would be required to be sure. Thus there is no indication that the parameterization significantly affected this response or that axial position of the groove is a likely contributor.

Direct Damping Coefficient

As with cross-coupled stiffness, a first-order factor effect model was found by sequential sum of squares to be the best fit regression model, significant at a 99.99% confidence level. The first-order factor effects all satisfied the ANOVA tests at a 99.99% confidence level, and higher order effects failed to reject the null hypothesis. The parameters of the model are given in Equation 23. The coefficients of determination were 0.936, 0.927, and 0.913 respectively for the standard, adjusted and predicted values. These R^2 values indicate strong linear correlation and good prediction of the data's variance about the mean by the model.

$$C_{XX} = 3.168 \times 10^5 + 5101(R_1) + 5483(R_2)$$

$$+5267(R_3) + 4048(R_4) + 5239(R_5) \tag{23}$$

On average, increases in groove radii appear to increase direct damping by 5027.6 N-s/m per mm. The parameter estimates for each radius are roughly equal, with overlapping error estimates. As with cross-coupled stiffness, this seems to indicate that axial position of the grooves and the parameterization used had minimal effect on this response.

Cross-coupled Damping Coefficient

The sequential sum of squares F-tests were performed for the cross-coupled damping coefficient response. No regression model was found to reject the null hypothesis that all parameters aside from the intercept were zero at a 90% confidence level. Additionally, coefficients of correlation were calculated for each hierarchical regression model. Every potential model shows poor correlation in the standard and adjusted R^2; however all of the predicted R^2's are negative. When the first-order factor effect parameters were added to the model, and removed one by one, the factor effect for R5 was found significant at better than a 99% confidence level. This indicates that the cross coupled damping coefficient has some minor dependence on groove radius scale, but it is likely being obscured by the parameterization or is dependent on the axial location of the groove. The coefficients of determination were 0.19, 0.17 and 0.11 respectively for the standard, adjusted and predicted values. The regression equation has only two parameters and is given in Equation 24. With such low correlation an additional test was performed by attempting to replace the factor effect associated with radius 5 with any other first-order factor effect one at a time. If a single first-order factor effect was

found interchangeable it would suggest that the significance of the remaining factor effect was due to chance. Each first-order factor effect associated with radii 1 to 4 produced negative adjusted and predicted R^2 values. The effect of the fifth groove radius remains significant at this time.

$$C_{XY} = 28265.84 - 94.66(R_5) \qquad (24)$$

Direct Mass Coefficient

Based on the sequential sum of squares F-tests for the direct mass coefficient response, adding the two factor interaction effect parameters to the regression model was significant at a 92% confidence interval. The first-order individual factor effects were all significant above a 99% confidence interval. However, all but two of the two factor interaction effects were not significant at the 90% confidence level. The remaining two interactions between the second and third radii and the third and fourth radii were judged significant with p-values of 0.047 and 0.08 respectively. There were no similar interaction effects between the first and second radius, the second and third, or the first and fifth. There is no physical mechanism in the flow to explain two groupings of adjacent grooves interacting but not the others. Therefore, the two interaction factor effects were neglected and assumed to be caused by a peculiarity in the mesh or an artifact of the method used to parameterize the geometry. Only the 6-parameter regression model consisting of an intercept and the first-order factor effects was used to model the direct mass coefficient, shown in Equation 25. This regression model explains approximately 73% of the variance in the data about the mean.

$$M_{XX} = 14.39 - 0.038(R_1) - 0.047(R_2)$$
$$-0.066(R_3) - 0.037(R_4) - 0.045(R_5) \tag{25}$$

The individual parameter estimates are approximately the same and have very similar confidence intervals. This implies that there is minimal effect on this response from the geometric parameterization. The direct mass coefficient decreases by an average of 0.0466 kg per millimeter increase in groove radius.

Cross-Coupled Mass Coefficient

The sequential sum of squares F-tests were performed for the cross-coupled mass coefficient response. No regression model was found to reject the null hypothesis that all parameters aside from the intercept were zero at a 90% confidence level. Additionally, coefficients of correlation were calculated for each hierarchical regression model. Every potential model shows poor correlation in the standard and adjusted R^2; however all of the predicted R^2 values are negative. This indicates that the models are unable to predict the location of observed data points. There is no confidence that a linear regression model of the factors included by this parameterization of the seal's geometry explains more variation in the cross-coupled mass coefficient response than the mean alone.

4.1.2 Investigation of the Design Point of Predicted Optimal Leakage Rate

As discussed above, the first parameterization and first experimental design regression model for leakage rate predicted a minimum leakage of 8.57 kg/sec at respective radii of 4.1 mm, 3.91 mm, 4.06 mm, 3.75 mm, 4.55 mm. A single simulation experiment was performed at this location in the design space to verify the accuracy of the selected regression models. Table 4.3 contrasts the actual responses found in the simulated experiment and the responses

predicted by the regression equations above. Impressively, even the regression models that were found to display weak correlation produced accurate predictions for the predicted optimum design point. The leakage rate prediction in particular was extremely accurate; however this is also affected by how flat the response surface is in the region of the selected design point. No prediction is shown for the cross-coupled mass coefficient because no regression model was found to better explain the variation in the response than the mean alone.

Table 4.3: Actual response vs responses predicted by regression,
at the predicted optimum design point

	Actual Response	Predicted Response	Percent Error
Leakage, Q [kg/sec]	8.540	8.570	0.36%
Direct Stiffness, K_{XX} [N/m]	1.914E+07	1.884E+07	1.61%
Cross-Coupled Stiffness, K_{XY} [N/m]	7.229E+08	7.309E+08	1.10%
Direct Damping, C_{XX} [N-s/m]	4.137E+05	4.195E+05	1.40%
Cross-Coupled Damping, C_{XY} [N-s/m]	2.865E+04	2.784E+04	2.84%
Direct Mass, M_{XX} [kg]	13.740	13.443	2.16%
Cross-Coupled Mass, M_{XY} [kg]	0.155		

4.2 First Parameterization Second Experimental Design

A second experimental design was performed on the same ANSYS CFX model and initial conditions used for the first parameterization. The first experimental design indicated that the baseline seal design is not near the optimum design point for minimal leakage rate. The predicted optimum radii, from the regression model of the first study, were found to be 4 mm on average. In order to confirm this predicted optimum location, and perform a sensitivity

study around the optimum, the second study is centered at 4 mm for each groove radius. The second study of 43 experiments was also selected to be a central-composite experimental design with five levels. The new factor levels were selected based on the variation in value for the individual radii at the previous predicted optimum location, radii of 4.10, 3.91, 4.06, 3.75, and 4.55 mm for the design factors respectively. The goal no longer being to explore a large volume of the design space, and having chosen a central composite design, an alpha value of 2.378 was selected to create a rotatable experimental design [32]. Based on the most extreme predicted optimum location of 4.55 mm a maximum was selected at 4.59mm. This placed the five levels of the central composite design at 3.41, 3.75, 4.00, 4.25, and 4.59 mm. The factorial design will be at the corners of the five-dimensional cube defined by 3.75 and 4.25 at each level, conveniently on or bracketing the original design's predicted optimum locations.

4.2.1 Second Experimental Design Results and Discussion

As with the first experimental design, a 21-parameter full quadratic model was initially posited to model each of the seven responses. However, the majority of the responses from the design points had little to no correlation with the five factors that describe the parameterized geometry. This is likely due to the fact that the factor levels are much closer to each other, implying that the differences in responses between design points are proportionally smaller. This reduction in response range allows "noise", or effects not taken into account by the factors used to parameterize the geometry, to overwhelm any effects from tested factors.

4.2.1.a Leakage Rate

Only a 6-parameter linear regression model was found significant at a 98% confidence level, based on sequential sum of squares analysis. However, the ANOVA results suggest that this model only accounts for 30% of the variation in the response and, many of the individual factor effects were found significant only at confidence levels of 60-80%. When the adjusted and predicted regression coefficients, of 0.2 and 0.055 respectively, are also taken into account there is minimal confidence in this regression model. Removing the insignificant factor effect parameters leaves the intercept and the factor effects for radii 1 and 5. This lowers the coefficient of determination to 0.233, does not change the adjusted R^2, and raises the predicted R^2 to 0.097. This is still a very poor regression model, especially when contrasted to the success of the original experimental design's regression model consisting of the first and second-order factor effects. However, the regression model from the first experimental design does predict that this region of the design space should produce rather flat leakage responses. As discussed above, a region of lower response variation may allow noise to overwhelm the regression model. This model has a signal to noise ratio of 6.69 (a ratio of 4 is considered minimum [42]), compared to a ratio of 23.9 for the original experimental design's response. This potentially confirms that effects masked or unaccounted for by the groove radii scale parameterization are more significant than the tested factors nearer the predicted optimum design point. As there is no expectation that this regression model represents reality, the equation is not provided herein.

4.2.1.b Rotordynamic Coefficients

Similarly to the leakage rate for this experimental design, the regression models for the rotordynamic coefficients were not found to be as well correlated as with the first experimental design. Only the coefficients for cross-coupled stiffness, direct damping and direct mass were found significantly different from the mean by the sequential sum of squares F-Test at a 90% confidence level. These three coefficient responses exhibited moderate to weak correlation with the data and were each fit with a simple linear 6-parameter model. The regression models for the remaining coefficients were not found to have coefficients that differed from zero. The adjusted and predicted correlation coefficients for these regression models were all negative. A negative adjusted R^2 indicates that the parameters added to the model provide no additional explanation of the variation in the data beyond the mean, and as above, a negative predicted R^2 indicates that the model is incapable of predicting the location of existing data points with any accuracy. For this experimental design, only the responses with significant regression models will be discussed further. In the case of each response the first regression model investigated corresponded to the parameters found to be significant in the original experimental design.

Cross-coupled Stiffness Coefficient

A 6-parameter model consisting of the intercept and first order factor effect parameters was found to best represent this response with a model F statistic of 13.68, suggesting less than 0.01% odds that such a model would apply by chance. Each first-order factor effect parameter was found to be significant at or above a 95% confidence level. The sequential sum of squares F-test and predicted R^2 values for higher-order regression models provide no evidence that the

model would be improved with additional parameters. The chosen regression model is given in Equation 26, and has coefficients of determination of 0.649, 0.602, and 0.522 respectively. The individual parameter estimates averaged higher for this experimental design, being greater than or approximately equal to the upper 95% confidence interval estimates of the same parameters from the original study. This is likely due to a greater standard error associated with each parameter estimate and not due to any physical mechanism. Additionally the signal to noise ratio was 14.29, indicating less noise for this response than for leakage rate. This provides an expectation that the cross-coupled stiffness coefficient is less affected, than leakage rate, by unknown variables that are not represented in this parameterization.

$$K_{XY} = 4.72 \times 10^8 + 2.03 \times 10^7 (R_1) + 1.10 \times 10^7 (R_2)$$
$$+1.16 \times 10^7 (R_3) + 7.74 \times 10^6 (R_4) + 1.14 \times 10^7 (R_5) \tag{26}$$

Direct Damping Coefficient

The direct damping coefficient response also continued to show a moderate linear correlation to the same factor effect parameters modeled in the first experimental design. The 6-parameter linear regression model, shown in Equation 27, was found to best fit the data with each first-order factor effect significant at better than 95% confidence. The coefficients of determination were found to be 0.619, 0.568, and 0.482 respectively, showing an acceptable correlation explaining 62% of the variation in the data about the mean. Similar to the cross-coupled stiffness coefficient, the parameter estimates average higher than those found for the original experimental design. However, the 95% confidence interval for each parameter estimate does overlap with the old estimates, except for the parameter associated with the

factor effect of radius 1 which is much higher. As before, the standard error associated with each parameter is also increased for this experimental design, nearly four times that of the original regression model for this parameterization. The increase in standard error makes the differences in the parameters most likely due to increased noise in this design rather than the different groove size levels being investigated.

$$C_{XX} = 2.8 \times 10^5 + 10882(R_1) + 6171(R_2)$$
$$+6421(R_3) + 4253(R_4) + 5559(R_5) \tag{27}$$

Direct Mass Coefficient

Like the regression model for the first experimental design, the first-order parameter model was found significant by the sequential sum of squares F-tests. The full quadratic and two factor interaction models failed with p-values of 0.93 and 0.86 respectively. ANOVA was then performed on the 6-parameter linear regression model, finding only the factor effect parameters associated with radii 1 and 2 to be significant at a better than 90% confidence level. The final 3-parameter model, including the intercept and the two significant radii, was found to have a coefficient of determination of 0.286, explaining about 29% of the data's variation about the mean. The adjusted and predicted R^2 values of 0.25 and 0.166 confirm this model to be acceptable, if weakly correlated to the response data. Similarly to the leakage rate response for this experimental design, the ratio of signal to noise in this response was only 8, compared to 17.57 for the original experimental design's response. The differences in regression model are assumed to be caused by other untested factors whose significance is relatively greater in the second experimental design because of the smaller variations in radius scale.

4.3 First Parameterization Combined Experimental Designs

While separately the results from the second experimental design produced less statistically significant regression models, when the data from these experiments was combined with the data from the first design in most cases it improved the significance of each regression model for those results. The same procedure was followed to determine the significance of individual factor effect parameters to be included in the regression models for each response. This resulted in the same factor effect parameters being included for every response except for the direct stiffness and cross-coupled damping coefficient responses. The direct mass coefficient was distinguished by the addition of a factor effect parameter that was not included in the original regression model from the first experimental design. Each of the regression models that did include the same factor effect parameters did experience a change in the parameter estimates, typically slight. This generally reinforces the validity of the regression models found from analyzing the responses of the first experimental design study. Table 4.3 is reproduced below, as Table 4.4, with the addition of the updated regression equations from the combination of the two data sets. Every regression model created with the combined set of data performed better at correctly predicting the actual response of the seal model simulated at the optimum design point predicted by the regression models from the first experimental design. No new optimum point was tested because the leakage regression models for the combined design were not greatly changed from the original regression models.

Table 4.4: Regression predictions vs actual simulation experiment responses

	Actual Response	First Experimental Design		Combined Experimental Design	
		Predicted Response	Percent Error	Predicted Response	Percent Error
Leakage, Q [kg/sec]	8.540	8.570	0.36%	8.551	0.14%
Direct Stiffness, K_{XX} [N/m]	1.914E+07	1.884E+07	1.61%	1.900E+07	0.73%
Cross-Coupled Stiffness, K_{XY} [N/m]	7.229E+08	7.309E+08	1.10%	7.247E+08	0.25%
Direct Damping, C_{XX} [N-s/m]	4.137E+05	4.195E+05	1.40%	4.154E+05	0.40%
Cross-Coupled Damping, C_{XY} [N-s/m]	2.865E+04	2.784E+04	2.84%	2.843E+04	0.76%
Direct Mass, M_{XX} [kg]	13.740	13.443	2.16%	1.365E+01	0.65%
Cross-Coupled Mass, M_{XY} [kg]	0.155				

4.3.1 Results and Discussion

4.3.1.a Leakage Rate

The desire to have a regression model complex enough to optimize, led to fitting a quadratic model to the present data (as was done for the first experimental design). Unlike the leakage rate response for the first experimental design, the sequential sum of squares F-tests found the full quadratic model to be significant at better than a 96% confidence level. ANOVA results indicated all of the two factor interaction effects failed significance at a 90% confidence level, except for the two factor interaction between radii 1 and 2. No physical mechanism was found to explain this exception, so the regression model was benchmarked with the simulated experimental response from the first experimental design's predicted optimal design point. The regression model performed worse at predicting the leakage rate response accurately, for the single test data point, with the two-factor interaction factor effect parameter included, thus it

was removed. The final regression model chosen contained the same factor effect parameters as those in the original experimental design's regression model, each significant at a 90% confidence level. The first-order and second-order factor effect parameters make up an 11-parameter least-squares regression model, with parameter estimates shown in Equation 28. The parameter estimate values were within the 95% confidence intervals for the values found from the original experimental design, thus not statistically different from the original stochastic values. The individual parameter estimates of each order of factor effect are approximately equal and have overlapping 95% confidence intervals. This suggests that each groove radius scale is equally influential and that axial position of grooves of varying scales has minimal effect on leakage rate, though there remains the possibility that the parameterization is obscuring other effects.

$$Q = 9.82 - 0.11R_1 + 0.012R_{11}^2 - 0.12R_2 + 0.014R_{22}^2 - 0.15R_3 + 0.018R_{33}^2$$
$$-0.11R_4 + 0.013R_{44}^2 - 0.084R_5 + 0.0077R_{55}^2 \tag{28}$$

The new regression model for leakage rate was characterized by a signal to noise ratio more than doubling from 23.9 to 52.3, an approximately halved standard error for each parameter estimate, and improvements in the three respective correlation coefficients of approximately 7%, 10%, and an astounding 47%. The actual R^2 values were 0.976, 0.973, and 0.962 for the standard, adjusted and predicted correlation coefficients. The associated model's F statistic was 303.83, with a p-value suggesting less than 0.01% probability that the estimated parameters are due to chance.

4.3.1.b Rotordynamic Coefficients

As found in the regression models from the first experimental design, a 6-parameter, or less, first-order factor effects model was determined best to fit the responses for the rotordynamic coefficients. The full first order factor effect model was applied to the coefficient responses for cross-coupled stiffness and direct damping. The direct mass coefficient included the same first-order factor effects, but adds a single second order factor effect. Notably, the cross-coupled damping coefficient response regression model was previously unable to be fit, but exhibited moderate correlation with a 4-parameter model of the first-order factor effects excluding those associated with radii 4 and 5. The cross-coupled mass coefficient remained unable to be fit by the available linear models. The only other regression model to not gain statistical significance and show improved correlation was the model for the direct stiffness coefficient response. The selected least-squares regression models for the responses are discussed below, again excluding the response for cross-coupled mass coefficient, and no attempt is made to optimize the rotordynamic coefficients to a particular target value.

Direct Stiffness Coefficient

With only the first-order factor effects found significant at a 90% confidence level by sequential sum of squares F-tests, ANOVA was performed to determine the significance of the individual parameters. Every parameter, except the intercept and the factor effect associated with radius 5, failed to be found significant at a 90% confidence level. Thus the direct stiffness coefficient response is the only coefficient response to have fewer parameters and lower coefficients of determination than originally modeled in the first experimental design. The 2-

parameter model, with parameter estimates shown in Equation 29, presented with standard, adjusted, and predicted coefficients of determination of 0.261, 0.252, and 0.219 respectively.

$$K_{XX} = 1.986 \times 10^7 - 1.886 \times 10^5 (R_5) \tag{29}$$

The model only explains 26% of the response data's variation about its mean. The signal to noise ratio did increase, less impressively than for leakage rate, from the original 8.35 to 13.28 with the combination of the data from the first and second experimental designs. As with the regression model, the low linear correlation implied by the R^2 values suggests that groove radius scale may not be a factor in the determination of direct stiffness of an annular seal. This is reinforced by only one groove radius being found significant. To test the correlation of the regression model further it was decided to attempt to replace the factor effect associated with radius 5 by the factor effects associated with each other radius one at a time and observe the changes in model quality. While, the factor effect representing radius 5 displays the strongest correlation, any of the other factor effects were found statistically significant at a 90% or better confidence level. With any single radius producing a weakly correlated, but statistically significant regression model, interchangeably, there is no confidence that these regression models represent any physical mechanism relating groove radius scale and the direct stiffness stability coefficient response.

Cross-coupled Stiffness Coefficient

Based on sequential sum of squares and ANOVA, the same 6-parameter factor effect model was chosen to fit the response for the cross-coupled stiffness coefficient response as originally selected to fit the same response from the first experimental design. The model and

its individual parameters were each found significant at a confidence level better than 99.99%.

As with the leakage rate response, the signal to noise ratio was approximately doubled from the original 43.6 to 86.3. The updated regression model was found to explain 98.3% of the data's variation about its mean, with both adjusted and predicted R^2 values above 0.98. Such a strong correlation suggests that all the major factors affecting the response have been accounted for. The regression model, Equation 30, gives the individual parameter estimates. Though the parameter estimates are apparently different for the radius 4 and 5 factor effects, the 95% confidence intervals for all of the parameter estimates overlap. Also, there is no physical mechanism to suggest that they should have different values, so it is assumed the effect of each groove radius scale is equal at an average positive correlation of 8.84×10^6 N/m per mm. There was no large change in the standard error associated with each parameter estimate, though there was a uniform minor decrease from the addition of the data points in the second experimental design.

$$K_{XY} = 5.44 \times 10^8 + 9.43 \times 10^6 (R_1) + 9.41 \times 10^6 (R_2)$$
$$+9.34 \times 10^6 (R_3) + 7.02 \times 10^6 (R_4) + 8.99 \times 10^6 (R_5) \tag{30}$$

Direct Damping Coefficient

Like the response for the cross-coupled stiffness coefficient, the direct damping coefficient response was found to be fit by the same six regression parameters used for the first experimental design data. Sequential sum of squares and individual parameter ANOVA F-tests were all found significant at better than 99.99%. The signal to noise ratio was improved from 41.9 to 80.5 by the addition of the second experimental design data to the data from the first

design. After the parameter estimates were updated to fit the additional data, the new regression model explained 98.1% of the response's variation about its mean. The adjusted and predicted R^2 values confirm the model's linear correlation and prediction ability with values greater than 0.97. As with the last coefficient's response, these coefficients of determination suggest that the primary factors influencing the direct damping coefficient only include the scales of the groove radii. The first-order factor effect parameter estimates are shown in Equation 31 with the intercept parameter.

$$C_{XX} = 3.202 \times 10^5 + 4943(R_1) + 5483(R_2)$$
$$+5267(R_3) + 4048(R_4) + 5239(R_5) \tag{31}$$

The parameter estimates and their associated standard errors were found to differ by less than 11%, except for the intercept parameter which experienced an approximately 50% reduction in standard error when compared to the model from the first experimental design. The parameter estimates associated with groove radii continued to have overlapping 95% confidence intervals, implying no likely difference in the effects of different groove radii's scale. The average effect of groove radius on the direct damping stability coefficient is 4996 N-s/m per mm.

Cross-coupled Damping Coefficient

There was no regression model for the cross coupled damping coefficient response from the first experimental design data. With the addition of the data from the second experimental design and beginning with the sequential sum of squares analysis, the first-order, two factor interaction and quadratic effects were all found to be significant models above a 95%

confidence level. However, the adjusted R^2 for the full quadratic only improved from 0.524, for

the first-order and two factor interactions model, to 0.568; the predicted R^2 only increased

from 0.4176 to 0.4183. This implies that the second-order factor effects of the full quadratic

regression model do not significantly add to the model's ability to explain variation in the data

or predict response values accurately. ANOVA was performed on the full quadratic model for

confirmation and the least significant terms, not required for model hierarchy, were removed

one at a time. All second-order factor effects and all but two two-factor interaction effects

failed the test for significance at a 90% confidence level. The remaining two-factor interaction

effects related the effects of radii 2 and 3 with those of radius 5. Because there is no physical

mechanism to explain interaction between groove radii, let alone non-adjacent groove radii,

these two-factor interaction effects were removed from the regression model. ANOVA was

then performed with the 6-parameter first-order factor effect model and only the effects of

radii 1, 2 and 3 were found significant at or above a 90% confidence level. The new regression

model for the cross-coupled damping coefficient response explains 41.3% of the data's

variation about its mean, roughly twice the explanatory power of the first experimental

design's regression model for the same response variable. This weak correlation is confirmed by

adjusted and predicted R^2 values above 0.348. The parameter estimates are given in the

regression model, shown in Equation 32.

$$C_{XY} = 2.78 \times 10^4 + 60.45(R_1) + 57.22(R_2) + 45.42(R_3) \qquad (32)$$

The factor effects included in the model are significant, supported by the proximity of

the second two coefficients of determination to the standard R^2. However, it is clear by the

ratio of the factor effect parameter estimates to the intercept parameter that the groove radii scale does not change the cross-coupled damping coefficient by any large amount. This suggests that either the parameterization is interfering with fitting the true factors relating groove size to cross-coupled damping coefficient, or there are additional unknown factors that play a significant role in determining this response.

Direct Mass Coefficient

Unlike the regression model from the first experimental design, sequential sum of squares analysis found a full quadratic model, for the direct mass coefficient response, to be significant at a better than 99% confidence level. The coefficients of determination suggested that any model whose complexity was between a 6-parameter first-order model and a 21-parameter full quadratic model would explain at least 80.9% of the data's variation about its mean. However, the predicted R^2 values for each model showed small gradations between the three hierarchical levels of model: first-order predicted R^2 of 0.766, first-order and two-factor interactions predicted R^2 of 0.806, and full quadratic predicted R^2 of 0.826. This suggests that a more complex model may not significantly increase the ability to predict the response, and may instead "over fit" the data. If the model is over fit then it includes more factor effects than necessary and begins to model the noise as well as the signal of the response. ANOVA was performed on the full quadratic model which resulted in all of the two-factor interaction effects and all but one of the second-order factor effects failing to be found significant at a 90% confidence level. A 7-parameter model results, containing all five first-order factor effect parameters and the second-order factor effect parameter associated with radius 3. There is no

physical mechanism that explains the inclusion of a single radius and not the others so this second order factor effect is removed from the final regression model. However, it should be noted that this may be some indication that groove axial position along the seal could affect this response. The selected 6-parameter regression model, with parameter effects shown in Equation 33, contained only the first-order factor effects.

$$M_{XX} = 14.21 - 0.022(R_1) - 0.029(R_2)$$
$$-0.043(R_3) - 0.018(R_4) - 0.026(R_5) \tag{33}$$

As stated above, this regression model explains 80.9% of the variation in the data about the mean, and the correlation and prediction capability are further confirmed by adjusted and predicted R^2 values of 0.797 and 0.766 respectively. The parameter estimates all decreased slightly when compared to those found for the response from the first experimental design, but like every other response they remained within the original 95% confidence intervals and are not necessarily statistically different from previous values or each other.

4.4 Second Parameterization Factorial Experimental Design

The experimental design for the second parameterization of the seal geometry was more complicated due to the nonlinear constraints defining valid shapes. Defining a central composite design where more than half of the design points were valid geometries proved difficult. Instead a five level full factorial design was investigated. Nominally this would involve 5^5, or 3125, experiments, however of the 3125 experiments only 98 were found to represent groove geometries within the constraints. Five levels were maintained to minimize the aliasing of the factor effects under investigation with higher order effects. 98 experiments were more

than enough to allow a full quadratic 21-parameter model or even a full cubic regression model. Unlike our previous parameterization the levels of each factor are distinct and shown in Table 4.5. The individual factor levels were selected to span the design space as widely as possible, but maintain the flexibility of investigating as many distinct shapes as possible. This is assisted by applying a full five level factorial design as every factor's level was combined with every other factor's level within the geometric constraints.

Table 4.5: Factor levels for the second parameterization variables

Alpha Index	Groove Width [mm]	Flat Width [mm]	Angle In [degrees]	Angle Out [degrees]	Depth [mm]
2.38	4.80	4.60	80	80	8.00
1	3.50	3.30	60	60	5.80
0	2.60	2.40	45	45	4.20
-1	1.70	1.50	30	30	2.60
-2.38	0.40	0.20	10	10	0.40

4.4.1 Results and Discussion

A different model, again parameterized with five design variables, was simulated in ANSYS CFX. The design variables allowed the seal's groove shape to vary widely between the extremes that define the geometric constraints. 98 simulated experiments were performed to characterize the leakage rate and rotordynamic coefficients for the intermediate shapes. The additional experiments and their distribution in the design space allowed the investigation of cubic regression models in addition to the previous quadratic models. A full cubic model was unavailable previously, for the experimental designs applied to the first parameterization, due to the degrees of freedom it requires, 56, and the central composite arrangement of design points, which aliases terms of higher than quadratic order. With 98 experimental degrees of freedom, even using a full 56-parameter cubic model would leave 42 degrees of freedom for

calculation of residuals. As above, the linear regression model for each response was reduced to include only those factors necessary to maintain the regression model hierarchy or found to be statistically significant at least a 90% confidence level. However, the sequential sum of squares F-tests found both full quadratic and full cubic models to be significant at greater than 94% confidence levels for every response except those representing the mass matrix coefficients. Cubic models are seldom applied to regression analysis, unless there is a physical mechanism supporting that analysis, for fear of over fitting the data. As previously explained, over fitting is when the additional factor effects added to a regression model begin to fit noise as well as signal. An over fit model would appear accurate based on its coefficients of determination, and would only be exposed as flawed by failing to accurately predict a response from a new data point, not included in the regression analysis. Thus it was not known whether a quadratic or cubic regression model would better fit the variation in the response variables. The first step to investigate whether a cubic regression model would be valid is to plot each response against each factor and look for indications of an "S" pattern characteristic to cubic polynomials. Figure 4.8 is a representative sample of these plots, showing the direct damping coefficient response plotted against each variable of the parameterization.
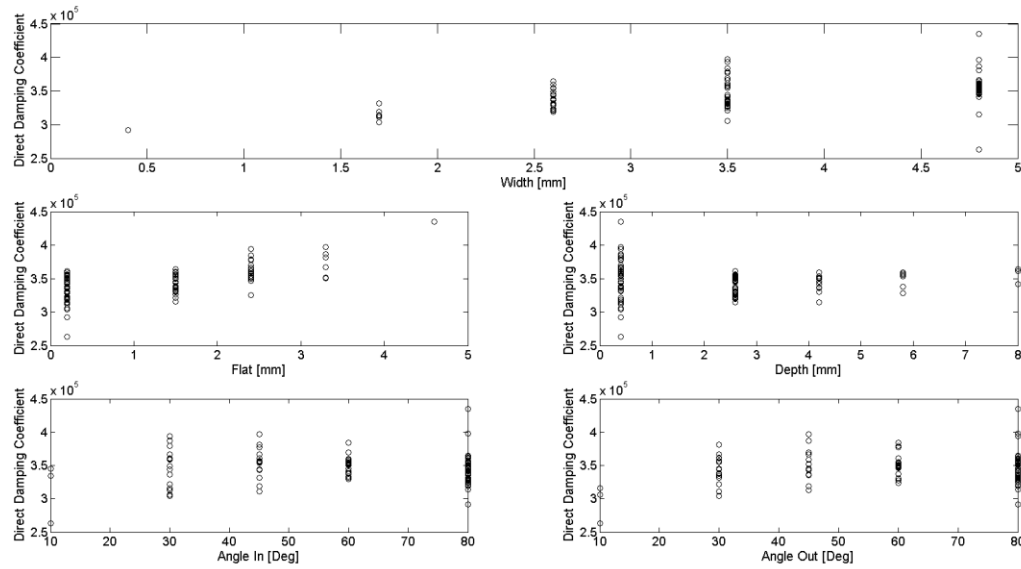
Figure 4.8: Direct damping coefficient response vs each factor

None of the plots has a clear "S" curve, however the plots against the leading and trailing groove angles have a potential flattened and backwards "S" shape to them. Equally significant, there is no clear indication of a parabola in any of the sub-plots to indicate a strong quadratic correlation. The one thing every plot has in common is the large variation in response at each factor level. Keeping in mind that the CFD simulations have a theoretical experimental error of zero, this variation at individual factor levels is likely due to the influence of various two or three-factor interactions. Multi-factor interactions are reasonable to assume for this parameterization. The geometric constraints on the groove shape alone provide some potential for factor interaction. Physically it also makes sense that the factors defining an individual groove's shape can and will interact to affect the flow. For example, the width factor when combined with depth can measure an approximate cross-sectional area of the groove cavity which is a factor in the size of the recirculating vortex that could occupy that region. Further,

77

the periodic nature of any physical analysis for the factors that describe the intake and exit angles of a groove supports model parameters of cubic hierarchy to act as Taylor series replacements of a sine or cosine function. In short, both quadratic and cubic regression models are feasible and should be tested further.

Thus for each response, when the sequential sum of squares analysis and ANOVA warrants, both quadratic and cubic least-squares regression models were fit to the data. The leakage rate response was optimized, over the nonlinear design space, for minimum response using both quadratic and cubic regression models as the objective function. An additional simulation experiment was then performed at each of the design points found by optimization of the quadratic and cubic regression models respectively. Comparison of the responses of these additional simulation experiments with the values predicted by the quadratic and cubic regression equations for each response was then used as an additional metric for selecting the final regression model. Tables showing the sequential sum of squares, model summary statistics, and ANOVA results were be shown for the leakage rate response analysis as a representative sample for this parameterization. The regression model found to best fit each response was visualized with multiple three-dimensional response surface generated with Design Expert. Only variation in two factors is shown per figure, the other three factors held constant in each figure were set to values that represent a design point of predicted minimum leakage rate, because this is the area most likely to interest a seal designer. The five-dimensional nature of the full design space limits the ability to visualize the complete relationship between the model factors and responses. When reading these figures it should

also be noted that the response surfaces shown represent predictions of response for all continuous factor values between the minimum and maximum domain boundaries. Not all combinations of these factors will produce a valid geometric groove shape based on the nonlinear constraints. In addition to the empirical regression modeling, eight simulations were selected to discuss the relationship between their responses and figures representing the streamlines and pressure profiles for the first groove cross-section.

4.4.1.a Leakage Rate

The mass flow leakage rate response was modeled with a 14-parameter quadratic and a 35-parameter cubic least-squares regression model. The sequential sum of squares analysis, Table 4.6, shows both the full quadratic and cubic models to be significant at better than 99.99% confidence. The model summary statistics, Table 4.7, display the coefficients of determination, and either potential model explains more than 95% of the variation in the response data about its mean. The cubic model will always have a larger standard R^2 value because it includes more parameters to explain the model, consuming more degrees of freedom. However, it also has adjusted and predicted R^2 values that are similarly increased. These coefficients of determination imply excellent linear correlation between the model and the response values and a high degree of prediction accuracy. On the other hand, the quadratic model has the advantage of being less complex without sacrificing very much linear correlation or prediction accuracy. The selection process of the quadratic regression model will be discussed first, followed by the cubic model, the optimization for minimal leakage, and the final choice of regression model.

Table 4.6: Leakage rate response sequential sum of squares analysis

Source	Sum of Squares	df	Mean Square	Calculated Value of F	p-value Prob > F
Mean vs Total	9515.45	1	9515.45		
Linear vs Mean	26.43	5	5.29	33.73	< 0.0001
2FI vs Linear	12.05	10	1.2	41.66	< 0.0001
Quadratic vs 2FI	1.4	5	0.28	22.01	< 0.0001
Cubic vs Quadratic	0.83	35	0.024	7	< 0.0001
Residual	0.14	42	3.40E-03		
Total	9556.31	98	97.51		

Table 4.7: Leakage rate response hierarchical model statistics

Source	Std. Dev.	R^2	Adjusted R^2	Predicted R^2
Linear	0.4	0.647	0.6278	0.5798
2FI	0.17	0.9419	0.9313	0.9085
Quadratic	0.11	0.9761	0.9699	0.9568
Cubic	0.058	0.9965	0.9919	0.9683

To select the statistically significant terms for the quadratic regression model ANOVA was performed on the full 21-parameter quadratic model and individual factor effects were removed one at a time in order of least significant. This process removed the second-order factor effects corresponding to groove width, flat width, and exit angle. Additionally four two-factor interaction effects were removed. The remaining 14 factor effects are significant at better than a 90% confidence level, many of them better than 99.99%. The ANOVA results for this 14-paramter model are given in Table 4.8 and the parameter estimates shown in Table 4.9. The regression model is shown in Equation 34.

Table 4.8: ANOVA for leakage rate response surface of a reduce quadratic regression model

Source	Sum of Squares	df	Mean Square	Calculated Value of F	p-value Prob > F
Model	39.84	13	3.06	254.18	< 0.0001
A-Width	0.59	1	0.59	48.59	< 0.0001
B-Flat	0.54	1	0.54	44.49	< 0.0001
C-Angle In	2.63	1	2.63	217.95	< 0.0001
D-Angle Out	0.11	1	0.11	8.82	0.0039
E-Depth	0.075	1	0.075	6.21	0.0147
AB	0.56	1	0.56	46.58	< 0.0001
AC	0.33	1	0.33	27.48	< 0.0001
AD	0.34	1	0.34	28.45	< 0.0001
AE	0.24	1	0.24	19.57	< 0.0001
CD	0.29	1	0.29	24.01	< 0.0001
DE	0.24	1	0.24	20.3	< 0.0001
C^2	1.86	1	1.86	154.13	< 0.0001
E^2	0.71	1	0.71	59.15	< 0.0001
Residual	1.01	84	0.012		
Corrected Total	40.85	97			

Table 4.9: Parameter estimates for the 14-parameter reduced quadratic regression model

Factor	Parameter Estimate	df	Standard Error	95% CL Low	95% CL High
Intercept	12.457	1	0.190	12.078	12.835
A-Width	0.284	1	0.0404	0.201	0.362
B-Flat	-0.387	1	0.0580	-0.502	-0.271
C-Angle In	-0.0643	1	0.00435	-0.0729	-0.0556
D-Angle Out	-0.0119	1	0.00401	-0.0199	-0.00394
E-Depth	-0.177	1	0.0711	-0.319	-0.0358
AB	0.0860	1	0.0126	0.0609	0.111
AC	-0.00429	1	0.000818	-0.00592	-0.00266
AD	-0.00482	1	0.000905	-0.00662	-0.00303
AE	0.0362	1	0.00818	0.0199	0.0524
CD	0.00021	1	4.281E-05	0.000125	0.000295
DE	0.00372	1	0.000826	0.00208	0.00536
C^2	0.00049	1	3.955E-05	0.000412	0.000570
E^2	-0.0298	1	0.00388	-0.0375	-0.0221

$$Q = 12.46 + 0.28W - 0.39f - 0.064\alpha - 0.012\beta - 0.18d$$
$$+0.086Wf - 0.00429W\alpha - 0.00483W\beta + 0.036Wd$$
$$+0.00021\alpha\beta + 0.00372\beta d + 0.00049\alpha^2 - 0.030d^2 + r \tag{34}$$

This reduced quadratic regression model explains 97.5% of the response's variation about its mean. The adjusted and predicted R^2 values are 0.971 and 0.963 respectively, and the signal to noise ratio is 90.6 well above the minimum of 4. This model fits the response data extremely well and can be used to navigate the design space.

Similarly, the ANOVA was performed on the full cubic model. 21 factor effects, of the original 56, failed to be found significant at a 90% or better level of confidence. All 21 of the terms that make up the full quadratic model were retained regardless of significance to preserve the model's hierarchy. For example, if the three factor interaction effect ABC is significant then any lower-order combination of those terms must be a part of the model, such as AB, AC, BC, A, B, and C. One third-order single factor effect (associated with exit angle), three quarters of the third-order two-factor interaction effects, for example A^2D, and half the three-factor interaction effects were removed. The ANOVA for the remaining factor effects is given in Table 4.10. They make up a 35-parameter reduced cubic regression model, shown in Equation 35, whose parameter estimates are provided in Table 4.11.

$$Q = 16.12 - 2.40W + 0.52f - 0.14\alpha - 0.043\beta + 0.82d - 0.25Wf$$
$$+0.024W\alpha + 0.0027W\beta - 0.59Wd - 0.0099f\alpha - 0.0013f\beta + 0.39fd$$
$$+0.00055\alpha\beta - 0.010\alpha d + 0.0032\beta d + 0.70W^2 - 0.077f^2 + 0.0013\alpha^2$$
$$+0.00010\beta^2 + 0.10d^2 + 0.0026Wf\alpha - 0.067Wfd - 0.00012W\alpha\beta + 0.0055W\alpha d$$
$$-0.0012f\alpha d + 0.034W^2f - 0.0045W^2\alpha + 0.061W^2d - 0.027Wd^2 - 0.0016\alpha d^2$$
$$-0.058W^3 + 0.017f^3 - (5.8 \times 10^{-6})\alpha^3 + 0.0088d^3 + r \tag{35}$$

This reduced cubic model explains 99.48% of the leakage rate response variation about its mean, with adjusted and predicted R^2 values of 0.992 and 0.98 respectively. The signal to noise ratio is also higher than the quadratic model at 110.4. These regression metrics indicate very strong linear correlation and good ability to accurately predict response values in the design space.

Table 4.10: ANOVA for leakage rate response surface of a reduced cubic regression model

Source	Sum of Squares	df	Mean Square	Calculated Value of F	p-value Prob > F
Model	40.64	34	1.2	351.63	< 0.0001
A-Width	0.075	1	0.075	22.09	< 0.0001
B-Flat	9.96E-03	1	9.96E-03	2.93	0.0919
C-Angle In	0.22	1	0.22	63.35	< 0.0001
D-Angle Out	0.091	1	0.091	26.91	< 0.0001
E-Depth	0.028	1	0.028	8.37	0.0052
AB	0.01	1	0.01	3.07	0.0848
AC	0.059	1	0.059	17.29	< 0.0001
AD	5.82E-03	1	5.82E-03	1.71	0.1955
AE	0.091	1	0.091	26.91	< 0.0001
BC	0.017	1	0.017	5.04	0.0283
BD	8.05E-03	1	8.05E-03	2.37	0.1289
BE	0.062	1	0.062	18.12	< 0.0001
CD	0.073	1	0.073	21.41	< 0.0001
CE	0.022	1	0.022	6.39	0.014
DE	0.036	1	0.036	10.54	0.0019
A^2	0.081	1	0.081	23.74	< 0.0001
B^2	9.41E-03	1	9.41E-03	2.77	0.1012
C^2	0.088	1	0.088	26.03	< 0.0001
D^2	0.03	1	0.03	8.97	0.0039
E^2	0.023	1	0.023	6.91	0.0108
ABC	0.027	1	0.027	7.87	0.0067
ABE	0.061	1	0.061	17.8	< 0.0001
ACD	0.042	1	0.042	12.49	0.0008
ACE	0.11	1	0.11	31.86	< 0.0001
BCE	0.01	1	0.01	2.95	0.0908
A^2B	0.014	1	0.014	4.15	0.0458
A^2C	0.11	1	0.11	31.55	< 0.0001
A^2E	0.081	1	0.081	23.81	< 0.0001
AE^2	0.1	1	0.1	30.3	< 0.0001
CE^2	0.038	1	0.038	11.22	0.0014
A^3	0.062	1	0.062	18.36	< 0.0001
B^3	0.014	1	0.014	4.09	0.0475
C^3	0.05	1	0.05	14.61	0.0003
E^3	0.09	1	0.09	26.44	< 0.0001
Residual	0.21	63	3.40E-03		
Corrected Total	40.85	97			

Table 4.11: Parameter estimates for the 35-parameter reduced cubic regression model

Factor	Parameter Estimate	df	Standard Error	95% CL Low	95% CL High
Intercept	16.120	1	0.698	14.726	17.514
A-Width	-2.399	1	0.510	-3.419	-1.379
B-Flat	0.522	1	0.305	-8.75E-02	1.131
C-Angle In	-0.136	1	1.71E-02	-0.170	-0.102
D-Angle Out	-4.26E-02	1	8.21E-03	-0.059	-2.62E-02
E-Depth	0.815	1	0.282	0.252	1.378
AB	-0.255	1	0.145	-0.545	3.60E-02
AC	2.43E-02	1	5.85E-03	1.26E-02	3.60E-02
AD	2.69E-03	1	2.06E-03	-1.42E-03	6.80E-03
AE	-0.592	1	0.114	-0.820	-0.364
BC	-9.87E-03	1	4.40E-03	-1.87E-02	-1.09E-03
BD	-1.28E-03	1	8.32E-04	-2.94E-03	3.82E-04
BE	0.393	1	9.24E-02	0.209	0.578
CD	5.47E-04	1	1.18E-04	3.11E-04	7.84E-04
CE	-1.02E-02	1	4.02E-03	-1.82E-02	-2.13E-03
DE	3.20E-03	1	9.86E-04	1.23E-03	5.17E-03
A^2	0.698	1	0.143	0.412	0.984
B^2	-7.68E-02	1	4.61E-02	-0.169	1.54E-02
C^2	1.27E-03	1	2.48E-04	7.71E-04	1.76E-03
D^2	1.04E-04	1	3.49E-05	3.48E-05	1.74E-04
E^2	0.100	1	3.82E-02	2.40E-02	0.177
ABC	2.57E-03	1	9.15E-04	7.38E-04	4.40E-03
ABE	-6.72E-02	1	1.59E-02	-9.91E-02	-3.54E-02
ACD	-1.17E-04	1	3.30E-05	-1.83E-04	-5.07E-05
ACE	5.47E-03	1	9.69E-04	3.53E-03	7.41E-03
BCE	-1.18E-03	1	6.88E-04	-2.55E-03	1.93E-04
A^2B	3.38E-02	1	1.66E-02	6.55E-04	6.70E-02
A^2C	-4.54E-03	1	8.08E-04	-6.15E-03	-2.92E-03
A^2E	6.13E-02	1	1.26E-02	3.62E-02	8.63E-02
AE^2	-2.73E-02	1	4.96E-03	-3.72E-02	-1.74E-02
CE^2	-1.65E-03	1	4.92E-04	-2.63E-03	-6.65E-04
A^3	-5.75E-02	1	1.34E-02	-8.43E-02	-3.07E-02
B^3	1.73E-02	1	8.55E-03	1.99E-04	3.44E-02
C^3	-5.84E-06	1	1.53E-06	-8.89E-06	-2.79E-06
E^3	8.84E-03	1	1.72E-03	5.41E-03	1.23E-02

Having created two high correlation regression models to predict leakage rate, the next step was to use them as objective functions to minimize the response. This procedure was done in Matlab as discussed in Chapter 3. Random design points were generated until 500 were found that met the non-linear geometric constraints. These 500 design points were then used as initial guesses for the optimization algorithm. The optimized design point with minimal leakage was selected for each of the two regression model objective functions. Both optimal design points predicted by the regression models have similar geometries. Figure 4.9 shows the seal geometry obtained from optimization of the quadratic regression model and shows an enlarged view of the geometry of an individual groove. The geometry is defined by a width of 4.79 mm, a flat width of 3.66 mm, an entrance angle of 70°, an exit angle of 80°, and a depth of 0.55 mm. As seen in the figure, this groove shape is squat and spread out. The quadratic regression model predicted a leakage rate of 8.8923 kg/sec for this groove geometry, while the cubic regression model expected 8.462 kg/sec of leakage. Optimization of the cubic regression model predicted the minimum leakage to occur from a similar groove shape, seen in Figure 4.10, with a width of 4.8 mm, flat width of 3.6 mm, inlet and exit angle of 80°, and a depth of 0.59 mm. For this potential optimum geometry the quadratic regression model predicted a leakage rate of 8.956 kg/sec and the cubic regression model estimated 8.230 kg/sec. The potential optimum designs were simulated in ANSYS CFX by the same procedure as the simulations performed for the experimental design. The actual simulation experiment results for these two designs are shown in Table 4.12 and Table 4.13 for the quadratic and cubic

regression models' predicted design point respectively. Additional comparisons for each of the

other responses are included in these tables and will be discussed in following sections.
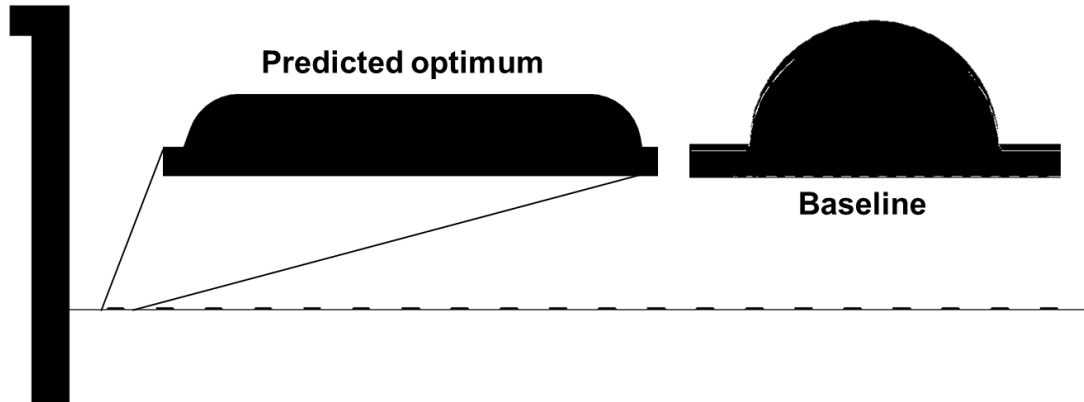
Figure 4.9: Baseline vs. predicted optimum seal groove geometry,
based on the reduced quadratic regression model

Table 4.12: Actual responses vs predicted responses for the design point predicted by the reduced
quadratic model

Response Label	Actual Response	Quadratic Predicted Response	Percent Error	Cubic Predicted Response	Percent Error
Leakage, Q [kg/sec]	8.5865	8.89235	3.56%	8.4623	1.45%
Direct Stiffness, K_{XX} [N/m]	1.721E+07	1.726E+07	0.32%	1.741E+07	1.18%
Cross-Coupled Stiffness, K_{XY} [N/m]	7.683E+08	7.056E+07	8.17%	1.263E+08	64.44%
Direct Damping, C_{XX} [N-s/m]	4.399E+05	4.017E+05	8.69%	4.194E+05	4.66%
Cross-Coupled Damping, C_{XY} [N-s/m]	2.780E+04	2.727E+04	1.89%	2.709E+04	2.54%
Direct Mass, M_{XX} [kg]	13.44775	13.63325	1.38%	13.4627	0.11%
Cross-Coupled Mass, M_{XY} [kg]	0.19036	0.11148	41.44%		
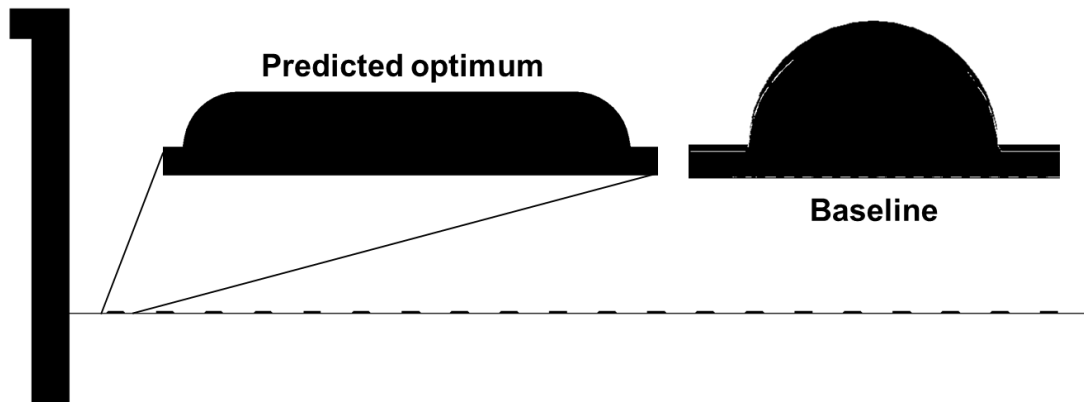
Figure 4.10: Baseline vs. predicted optimum seal groove geometry, based on the reduced cubic
regression model

Table 4.13: Actual responses vs predicted responses for the design point predicted by the reduced cubic model

Response Label	Actual Response	Quadratic Predicted Response	Percent Error	Cubic Predicted Response	Percent Error
Leakage, Q [kg/sec]	8.386	8.956	6.80%	8.230	1.86%
Direct Stiffness, K_{XX} [N/m]	1.634E+07	1.854E+07	13.48%	1.806E+07	10.53%
Cross-Coupled Stiffness, K_{XY} [N/m]	7.722E+08	6.938E+08	10.15%	1.455E+09	88.41%
Direct Damping, C_{XX} [N-s/m]	4.433E+05	4.017E+05	9.40%	4.110E+05	7.29%
Cross-Coupled Damping, C_{XY} [N-s/m]	2.742E+04	2.751E+04	0.33%	2.753E+04	0.38%
Direct Mass, M_{XX} [kg]	13.508	13.690	1.35%	13.692	1.37%
Cross-Coupled Mass, M_{XY} [kg]	0.202	0.142	30.08%		

The cubic regression model for leakage outperformed the quadratic regression model at predicting the mass flow leakage rate for both simulated experiments. Also, the optimum design point found from the cubic regression model resulted in a lower leakage rate than the design point from the quadratic model. For mass flow leakage rate the cubic regression model better fits the response data, better predicts leakage rates within the design space, and predicts a lower minimum for leakage rate. The simulated leakage rate response of 8.3862 kg/sec, at the predicted optimal design point, represents a 1.8% improvement over the leakage rate found from the first parameterization and DOE, and a 7.28% improvement over the leakage rate of the baseline seal geometry. Figure 4.11 is a Pareto chart showing the sum of squares of variation for each factor effect. Larger absolute values indicate that the factor effect explains more of the response's variation about the mean. Positive values indicate a direct correlation and negative values an inverse correlation. The higher order and interaction factor effects make it difficult to assign priority to the effects of a particular design variable; however, the groove flat width appears to have the least impact on leakage rate performance. Figure 4.12 through

Figure 4.14 show three-dimensional response surface plots of the leakage rate response represented by the chosen reduced cubic regression model.
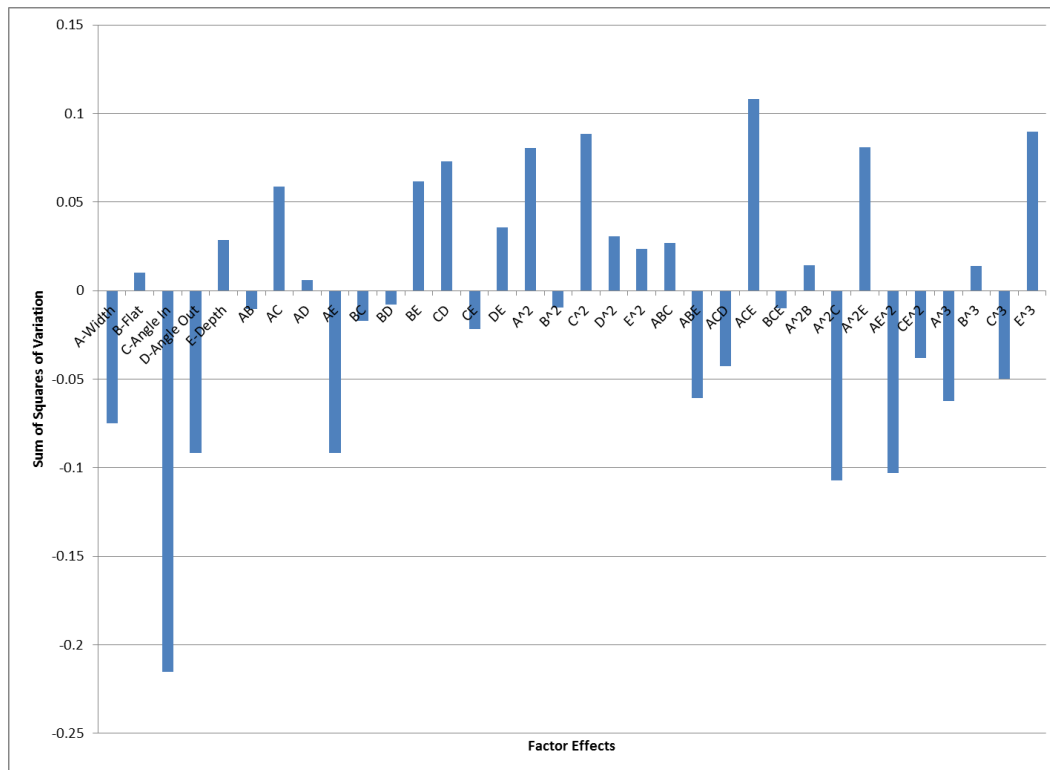
Figure 4.11: Pareto chart showing relative factor effects from the regression model for leakage rate response based on explained sums of squares of variation
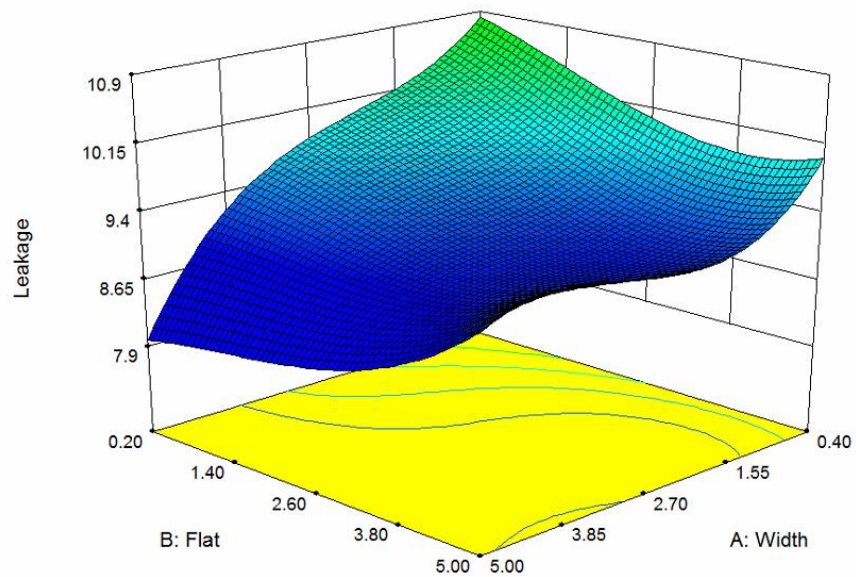
Figure 4.12: Cubic Regression model response surface of leakage rate sensitivity near the predicted optimal design point, in terms of groove width and flat width
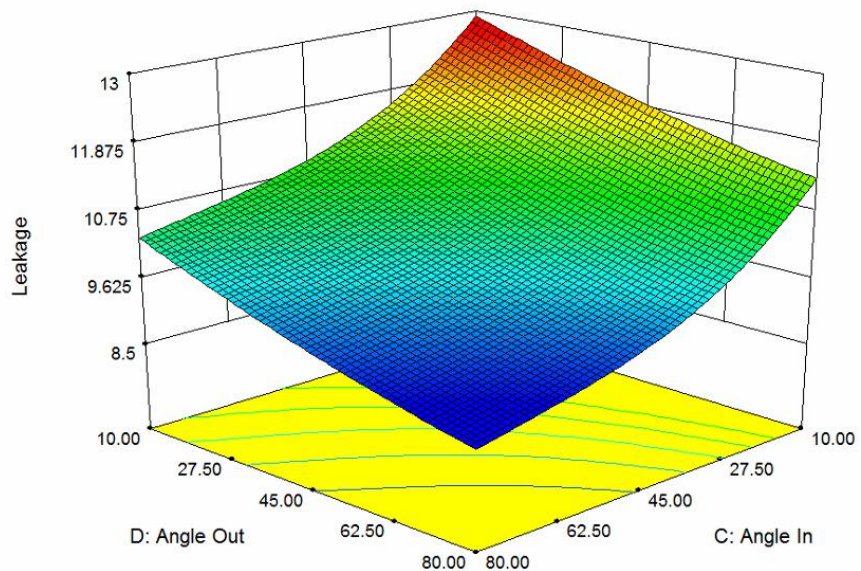
Figure 4.13: Cubic Regression model response surface of leakage rate sensitivity near the predicted optimal design point, in terms of the groove entrance and exit angles
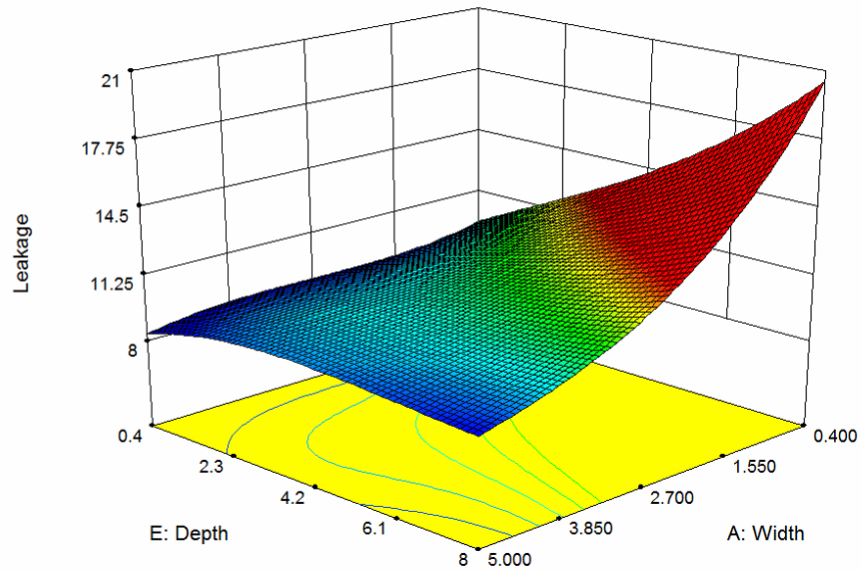
Figure 4.14: Cubic Regression model response surface of leakage rate sensitivity near the predicted optimal design point, in terms of groove width and depth

Having selected the reduced cubic regression model to fit the leakage rate response data, the flow visualizations within the first axial groove of the seal were compared between the optimum groove geometry, the baseline groove geometry, and six other geometries from the experimental design. The six additional geometries were selected to be similar to the optimal geometry in all but one or two design variables to discuss the effects of changing each variable on the flow visualization, and ultimately, the leakage rate response. The design points of the example geometries are listed in Table 4.14, and their associated responses are given in Table 4.15. The flow visualizations include streamlines and pressure profiles for each of the selected groove geometries and are shown in Figure 4.15 and Figure 4.16 respectively.

Table 4.14: Design point geometries selected for flow visualization

Run #	Width	Flat Width	Angle In	Angle Out	Depth
Baseline	3.18	1.59	90	90	1.59
Optimum	4.8	3.6	80	80	0.59
(Δf) 7	4.8	4.6	80	80	0.40
(Δα, Δβ) 27	4.8	3.3	30	30	0.40
(Δd) 28	4.8	3.3	80	80	2.60
(ΔW) 36	3.5	3.3	80	80	0.40
(Δα) 74	4.8	3.3	45	30	0.40
(Δβ) 81	4.8	3.3	30	45	0.40

Table 4.15: Responses for the design points selected for flow visualization

Run #	Q [kg/sec]	K_{XX} [N/m]	K_{XY} [N/m]	C_{XX} [N-s/m]	C_{XY} [N-s/m]	M_{XX} [kg]	M_{XY} [kg]
Baseline	9.076	1.981E+07	6.053E+08	3.546E+05	2.810E+04	14.067	0.122
Optimum	8.386	1.634E+07	7.722E+08	4.433E+05	2.742E+04	13.508	0.202
(Δf) 7	8.941	1.756E+07	7.621E+08	4.347E+05	2.705E+04	13.342	0.428
(Δα, Δβ) 27	10.956	2.055E+07	6.539E+08	3.668E+05	2.988E+04	13.848	-0.107
(Δd) 28	9.312	2.100E+07	5.954E+08	3.508E+05	2.841E+04	14.209	-0.001
(ΔW) 36	8.929	1.714E+07	6.874E+08	3.975E+05	2.717E+04	13.782	0.134
(Δα) 74	10.314	1.972E+07	6.718E+08	3.813E+05	2.865E+04	13.702	0.020
(Δβ) 81	10.541	1.772E+07	6.897E+08	3.868E+05	2.868E+04	13.792	0.280

Flow Direction

Velocity
Streamline 1

6.500e+001

4.875e+001

3.250e+001

1.625e+001

0.000e+000
[m s^-1]

a)   Baseline geometry streamlines

b)   Optimum geometry streamlines

c)   Run # 7 geometry streamlines

d)   Run # 27 geometry streamlines

e)   Run # 28 geometry streamlines

f)   Run # 36 geometry streamlines

g)   Run # 74 geometry streamlines

h)   Run # 81 geometry streamlines

Figure 4.15: Velocity streamlines for flow visualization
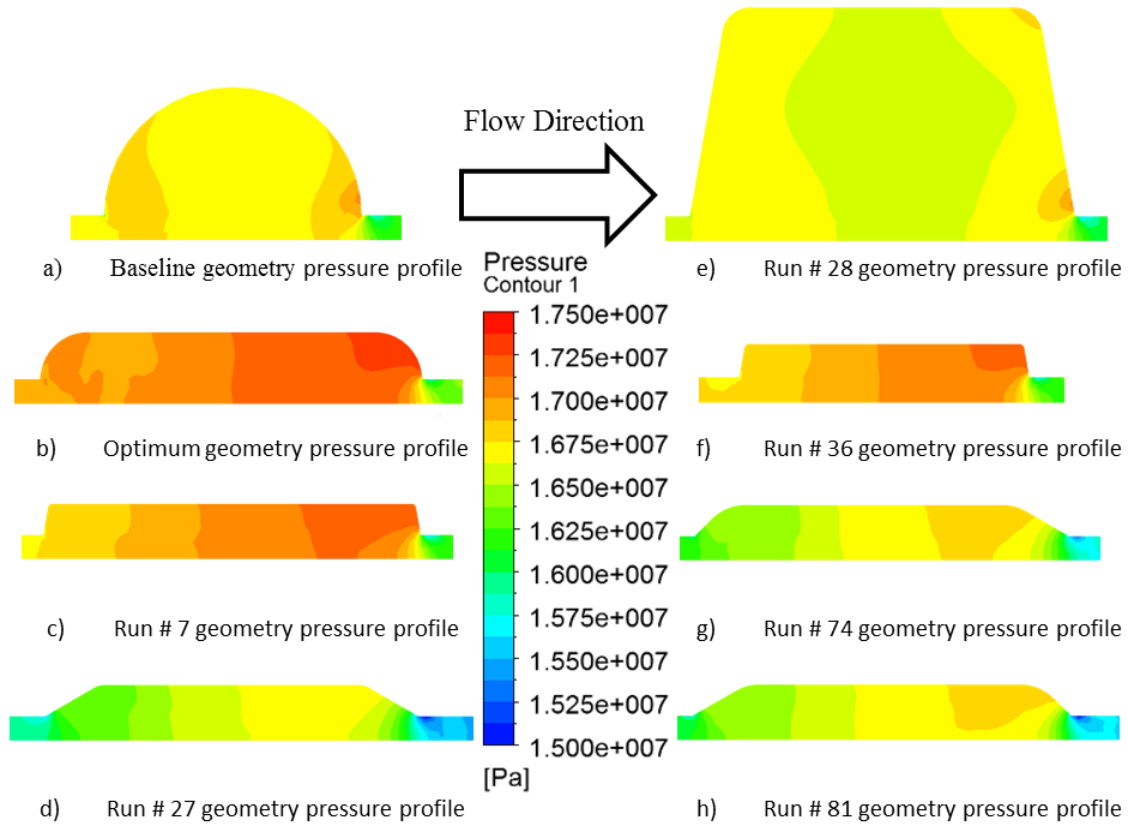
Figure 4.16: Pressure profiles for flow visualization

The optimum groove geometry streamlines exhibit a wide flat vortex, mirroring the groove shape, which spans approximately three quarters of the groove width. The jet flow region enters from the clearance region at the front and expands into the rear of the groove cavity starting at about half the width. The abrupt contraction of the flow back into the annular clearance region slows the flow as it leaves the groove. This slowing of the exit flow and the long contact with the recirculating vortex contribute to the minimum leakage rate response from this seal geometry. Additionally, the exiting flow in the groove cavity follows the curve of the groove wall closely.

The highest leakage rate response of the example geometries was exhibited by groove geometry number 28, followed by runs 74 and 81. Each of these geometries is differentiated

from the optimum seal geometry by reduction of the groove entrance and exit angles. Smaller

entrance angles reduce the effect of the recirculation vortex and smaller exit angles smooth the

changes in flow direction contracting into the clearance region. These physical mechanisms

agree with the conclusions from the reduced cubic regression model, and its response surfaces,

that steep entrance and exit angles reduce the leakage rate response. Also, the highest leakage

rate from any simulation was observed from groove geometry number 13, shown in Figure

4.17. This further confirms that reducing the abruptness of fluid directional changes increases

leakage rate.
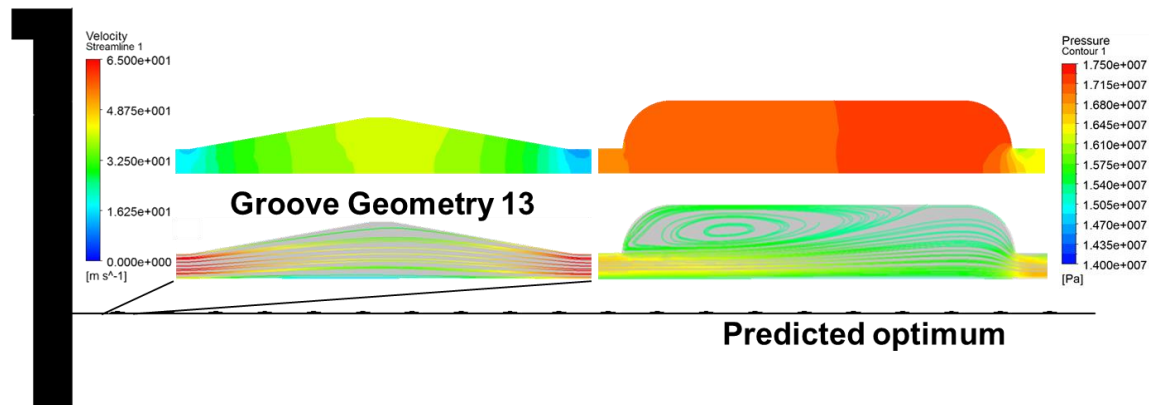
Figure 4.17: Groove geometry number 13, streamlines and pressure profile

The next highest leakage rate responses are observed in the baseline and groove

geometry number 28 simulations. These simulations also are characterized by deeper grooves

with aspect ratios nearer to unity. This allows for large recirculation vortices, to the point of

filling the groove cavity. However this leaves jet flow in the seal without room for directional

changes, because there is minimal room for it to expand into the groove behind the vortex. This

effect would be more pronounced for more narrow grooves as expected based on the response

surfaces. With sufficiently wide grooves there is the potential for multiple vortices, explaining

the slight down trend in the leakage rate response as depth increases with wider grooves, as seen in the response surface.

The remaining flow visualizations for simulation runs 7 and 36 are differentiated from the optimum geometry by decreasing groove width and increasing flat width respectively. These changes result in wide sharp cornered nearly rectangular grooves. The sharper corners reduce the size of the recirculation vortices, allowing the incoming jet flow to expand more gradually into the remaining portion of the groove cavity. Any reduction in the abruptness of changes in flow direction reduces the loss of kinetic energy from expansion or contraction. The response surface relating groove width to flat width is the most complex, exhibiting the most cubic curvature of the surfaces shown. This makes assigning physical mechanisms more difficult; however, these flow visualizations do not contradict the regression model.

4.4.1.b Rotordynamic Coefficients

Sequential sum of squares analysis and coefficients of determination for full quadratic and cubic regression models suggest either model would be reasonable to apply to the rotordynamic coefficient responses, except the cross-coupled mass coefficient response. The same comparison, between the ability of a reduced quadratic or cubic regression model to predict the responses of the simulation experiments performed at the design points for predicted optimum leakage rate, was used to determine the appropriate regression model for each relevant response. For each analysis, the potential regression models are given, as above with leakage rate, and their quality and prediction ability will be compared and discussed. Representative tables of the detailed results from each statistical analysis method are shown

for the leakage rate response above. A model with statistical significance of greater than 99% confidence was obtained for each response. Each regression model, except the one modeling the cross-coupled mass coefficient response, was found to explain more than 75% of the variation about the mean of its respective response. Despite the ability to optimize the quadratic and cubic regression models representing the stability coefficients for maxima and minima, no optimization study was performed for these responses as no universally desirable target can be applied to all turbomachine systems.

Direct Stiffness Coefficient

The full 21-parameter quadratic regression model was found significant at above a 97% confidence level a by sequential sum of squares F-test. Initially, the discrepancy between the standard R^2, 0.829, and predicted R^2, 0.562, was larger than the rule of thumb allowed difference of 0.2 [42]. ANOVA and backwards elimination of factor effects not found significant at above a 90% confidence level resulted in a 13-parameter model. The second-order factor effect for groove entrance angle was eliminated from the regression model along with seven out of ten two-factor interaction effects. The remaining interaction effects include groove width with exit angle, flat width with entrance angle, and entrance and exit angle. The only factor effect included in the model but not significant above a 98% confidence level was the first-order factor effect for groove width. This factor effect was not eliminated to maintain regression model hierarchy, despite only being found significant above a 74% confidence level. The 13-parameter reduced quadratic regression model was found to explain 81.2% of the response's variation about its mean. The reduction of the original full quadratic model also

resulted in an increase in predicted R^2 to 0.638. The parameter estimates of the reduced quadratic regression model are given in Equation 36.

$$K_{XX} = 3.351 \times 10^7 - (7.888 \times 10^5)\text{W} - (1.541 \times 10^6)\text{f} - (1.349 \times 10^5)\alpha$$
$$-(2.370 \times 10^5)\beta - (8.995 \times 10^5)\text{d} - 22381w\beta + 25614f\alpha + 1982\alpha\beta$$
$$+(2.920 \times 10^5)w^2 - (2.595 \times 10^5)\alpha^2 + 1402\beta^2 - (1.261 \times 10^5)\text{d}^2 \qquad (36)$$

The competing reduced cubic regression model consisted of 40 parameters. Like the full quadratic model for this response, the full 56-parameter cubic regression model had a noticeable discrepancy between its standard R^2 value of 0.982, and the predicted R^2 value of 0.678. The backwards elimination reduction of the full cubic model, based on ANOVA results, increased the predicted R^2 value to 0.839. The 40-parameter reduced cubic regression model was found to explain 97.7% of the response's variation about the mean. The adjusted R^2 value of 0.962 implies that the parameters added to the model in addition to the full quadratic model do in fact add significant explanatory value to the end regression model. While the cubic regression model is expected to have a higher correlation to the response because of the extra parameters, this predicted R^2 value is closer to the standard R^2 value of 0.977 than the associated coefficients of determination for the reduced quadratic regression model. Three factor effects not found significant above a 90% confidence level were included in the regression model to preserve model hierarchy. The included insignificant factor effects are the single factor effect representing exit angle and the two-factor interaction effects between flat width and exit angle, and between groove width and exit angle. All the included factor effects

and their parameter estimates are given in the reduced cubic regression model, shown in Equation 37.

$$
\begin{aligned}
K_{XX} = {}& 5.64 \times 10^7 - (2.45 \times 10^7)W + (1.66 \times 10^7)f \\
& -(5.69 \times 10^5)\alpha - (1.14 \times 10^5)\beta + (6.29 \times 10^6)d - (7.05 \times 10^6)Wf \\
& +(2.06 \times 10^5)W\alpha + 46778W\beta - (4.26 \times 10^6)Wd - (2.12 \times 10^5)f\alpha - 48875f\beta \\
& +(4.39 \times 10^6)fd + 10210\alpha\beta - (1.71 \times 10^5)\alpha d + (1.29 \times 10^5)\beta d + (6.40 \times 10^6)W^2 \\
& +(1.47 \times 10^6)f^2 + 2282\alpha^2 - 7646\beta^2 + (9.17 \times 10^5)d^2 + 27841Wf\alpha + 40950Wf\beta \\
& -(3.51 \times 10^5)Wfd + 41840W\beta d - 35202f\beta d + (3.63 \times 10^5)W^2f - 29854W^2\alpha \\
& -24555W^2\beta + (3.25 \times 10^5)W^2d - (1.53 \times 10^5)Wd^2 - 19665f^2\beta + 627f\alpha^2 - 75\alpha^2\beta \\
& +1189\alpha^2 d - 1484\beta^2 d - 13430\beta d^2 - (3.44 \times 10^5)W^3 - 62.78\beta^3 + 56084d^3 \quad (37)
\end{aligned}
$$

Based on the comparison of the test simulation results with the reduced quadratic and cubic predictive regression models shown in Table 4.12 and Table 4.13 above, the reduced quadratic regression model was selected to best fit the direct stiffness coefficient response. Each of the potential regression models was better at predicting the response around their own predicted optimal design point. The reduced quadratic regression model had a prediction accuracy of 0.32% vs the reduced cubic regression model's 1.18% for the design point predicted to produce optimal leakage rate by the quadratic regression model for leakage response; while, for the design point predicted by the cubic regression model for leakage response, the reduced quadratic regression model's prediction accuracy was 13.48% vs the reduced cubic model's 10.53%. However, the reduced quadratic model is less complicated and runs less risk of accidentally fitting noise in the response data. The Pareto chart in Figure 4.18 shows the relative explanatory power of each of the factor effects. The response surfaces representing the reduced quadratic model are shown in Figure 4.19 through Figure 4.21.
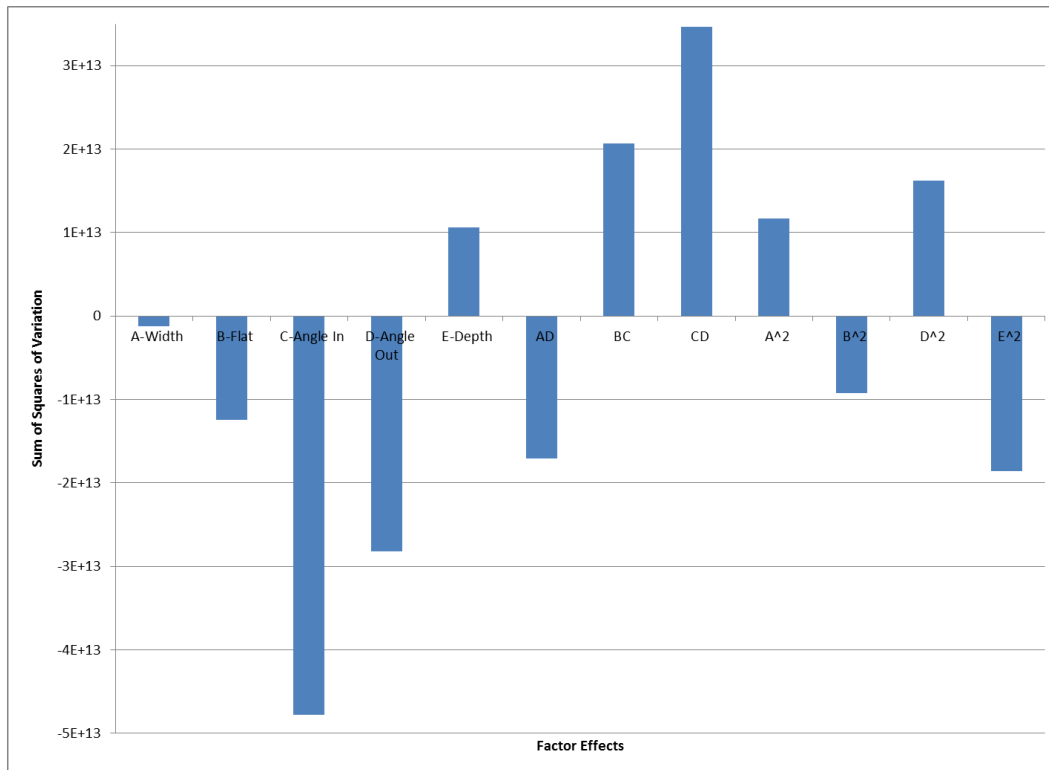
Figure 4.18: Pareto chart showing relative factor effects from the regression model for direct stiffness coefficient response based on explained sums of squares of variation
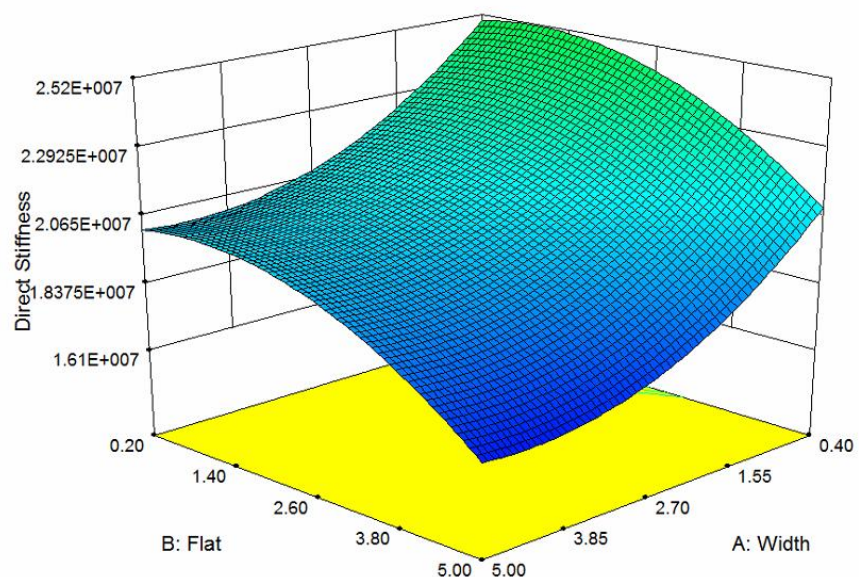
Figure 4.19: Response surface of direct stiffness coefficient sensitivity near the predicted optimal design point, in terms of groove width and flat width

99
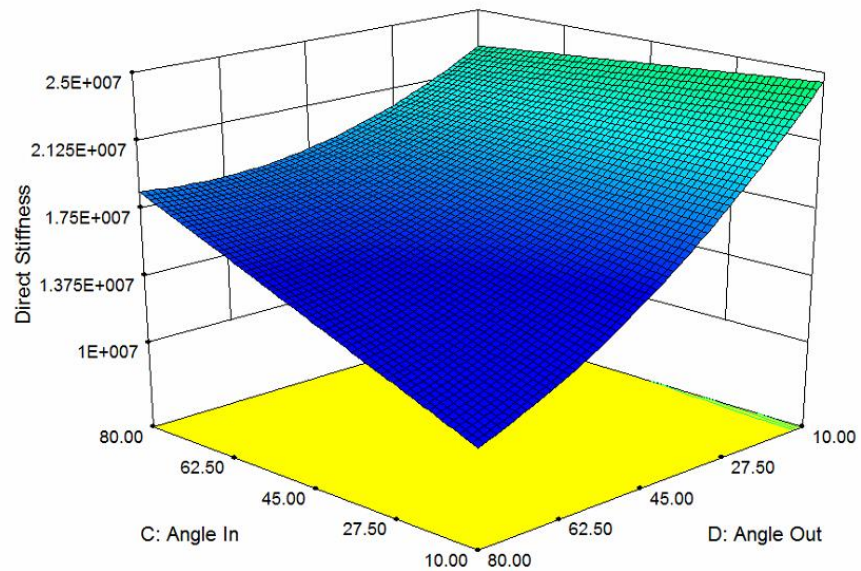
Figure 4.20: Response surface of direct stiffness coefficient sensitivity near the predicted optimal design point, in terms of groove entrance and exit angles
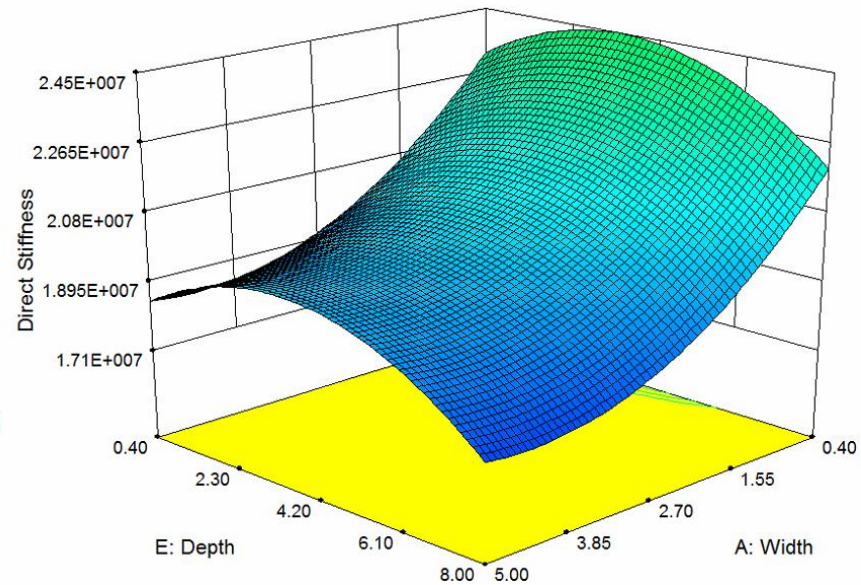
Figure 4.21: Response surface of direct stiffness coefficient sensitivity near the predicted optimal design point, in terms of groove width and depth

The groove geometry optimized for minimum leakage rate also exhibited a low direct stiffness coefficient, the lowest of the seal geometries selected for flow visualization. The minimum direct stiffness coefficient response simulated was found to correspond to test groove geometry number 41, depicted below in Figure 4.22. This geometry of minimum direct stiffness is described by a width of 4.8mm, flat width of 0.2 mm, depth of 0.4 mm and entrance and exit angles of 10°. The geometry is distinguished from the geometry associated with minimum leakage rate by decreases in groove width, flat width and entrance angle. These trends are not reflected in the response surface relating groove width and flat width above, however those response surfaces are only displayed for values of the other design variables fixed at the optimal leakage rate design point. The response surface in Figure 4.20 is supported by the geometry associated with minimum stiffness, showing that for large exit angles decreasing the entrance angle decreases the direct stiffness. This also explains the low direct stiffness coefficient responses of groove geometry numbers 7 and 36.
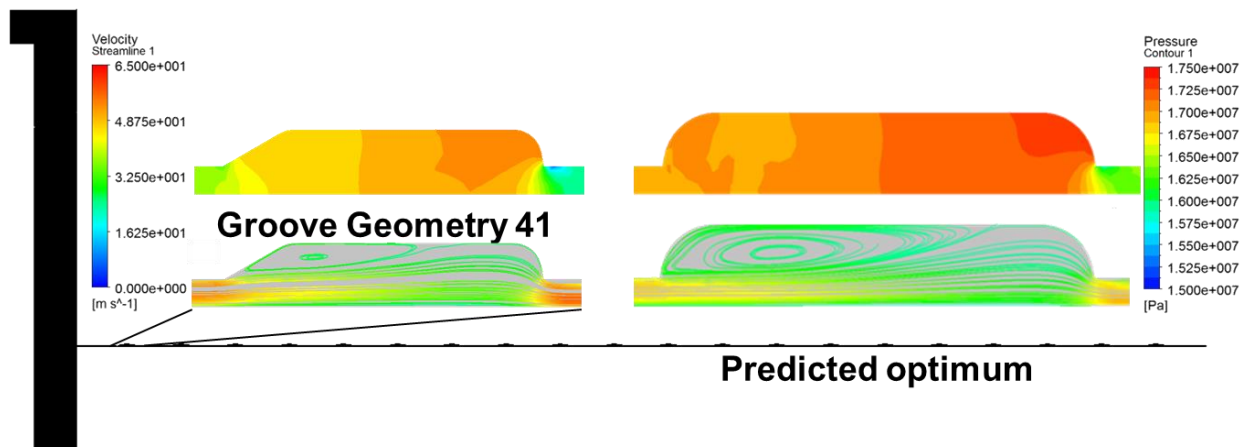
Figure 4.22: Groove geometry number 41, streamlines and pressure profile

The response surface in Figure 4.20 shows the effect of the interaction factor effects. While the direct stiffness coefficient decreases with decreasing entrance angle at high to mid-range values of exit angle, the opposite is true at low exit angles. This relationship is supported by the response of groove geometry number 74. Figure 4.20 is further supported by the decrease in direct stiffness coefficient response with increasing exit angle comparing the responses of groove geometry number 81 to groove geometry number 27. Figure 4.19 and Figure 4.21 show a concave parabolic relationship between groove width and the direct stiffness of the seal. The direct stiffness decreases with increasing groove width, with the effect becoming less pronounced from wider grooves. This correlation is supported by the slight increase in direct stiffness response in run 36 as compared to the seal geometry associated with minimum leakage rate. Figure 4.19 also depicts a decrease in direct stiffness with increasing flat width. The response of groove geometry number 7 does not appear to support such a correlation; however the reduced quadratic regression model predicts the response within 4.46% of the simulation result for the geometry of groove geometry number 7. This suggests that the failure is not in the regression model; merely that the response surface centered on the groove geometry of minimum leakage rate does not represent the flow behavior in groove geometry with additionally different flat width and groove depth. As previously mentioned, the response surfaces depicted in this work are two dimensional slices of a larger five dimensional design space and should not be expected to apply when the design variables held fixed in the figure are different from those describing the geometry of interest.

The highest direct stiffness coefficient response was found to be caused by wide and shallow triangular grooves. Wide and shallow triangular grooves also correspond to a maximum leakage rate response. This is observed in the simulations selected for flow visualization with the response of groove geometry number 27, and in groove geometry number 13 from the full data set. Interestingly, the highest direct stiffness, from the flow visualization examples, results from groove geometry number 28. The deeper groove and higher volume groove cavity contribute to increased direct stiffness by confining the jet flow to the clearance region, making the flow similar to a plain annular seal or journal bearing. The response surface in Figure 4.21 is in agreement with the increased direct stiffness when comparing groove geometry number 28 to the geometry of minimum leakage rate. The direct stiffness peaks at groove depths of approximately 3.5 mm and decreases for larger and smaller depths at all groove widths. The groove geometry showing the highest direct stiffness response corresponded to the highest leakage rate response. Similarly, the groove geometry associated with minimum leakage rate exhibited a low direct stiffness; however, the geometry of minimum direct stiffness did not have a particularly low leakage rate. This suggests that while the causation of these effects may be related, the physical mechanisms explaining each response are not identical.

Cross-coupled Stiffness Coefficient

Both the full quadratic and full cubic regression models fit the cross-coupled stiffness coefficient response data with greater than 99% confidence. ANOVA and backwards elimination of insignificant factor effects was performed on the initial 21-parameter full quadratic regression model. This resulted in a 12-parameter reduced quadratic regression model

consisting of the intercept, the first-order factor effects, two two-factor interaction effects, and four of the five second-order factor effects. Each of these factor effects was found to be individually significant by the ANOVA at above a 90% confidence level, except for the first order factor effect corresponding to the flat width which only met a 71% confidence level, but was included to preserve model hierarchy. The parameter estimates that make up the regression model are given in Equation 38 and explain 90.97% of the response's variation about its mean. The adjusted and predicted coefficients of determination are 0.898 and 0.863 respectively, indicating that the few if any of the parameters fail to add explanatory power to the regression model and that it has reasonable accuracy for predicting the responses of existing data points.

$$
\begin{aligned}
K_{XY} = \ & 3.74 \times 10^8 + (3.53 \times 10^7)W + (6.32 \times 10^6)f + (8.27 \times 10^5)\alpha \\
& + (4.00 \times 10^6)\beta - (2.02 \times 10^7)d - (5.05 \times 10^6)fd - 20429\alpha\beta \\
& - (2.15 \times 10^6)W^2 + (5.49 \times 10^6)f^2 - 19845\beta^2 + (2.58 \times 10^6)d^2
\end{aligned}
\qquad (38)
$$

ANOVA and backwards elimination of insignificant terms was also performed on the full 56-parameter cubic regression model, resulting in a 39-parameter reduced cubic regression model. Enough higher order combinations of factor effects were found significant and included in the model that all 21 of the factor effects that would make up a full quadratic model are included to preserve model hierarchy, despite the first-order factor effect corresponding to entrance angle to the groove, and the two-factor interactions combining the effects of groove entrance angle with groove depth, and groove width with exit angle. The parameter estimates of this reduced cubic regression model are given in Equation 39. There is high linear correlation between the model and the response variable, explaining 98.5% of the response's variation

about its mean. The adjusted and predicted R^2 values are correspondingly high at 0.976 and 0.936 respectively.

$$\begin{aligned}
K_{XY} &= 2.58 \times 10^8 + (2.96 \times 10^8)W - (1.80 \times 10^8)f \\
&\quad -(3.25 \times 10^6)\alpha + (3.45 \times 10^6)\beta - (9.60 \times 10^7)d + (9.42 \times 10^7)Wf \\
&\quad -(1.64 \times 10^6)W\alpha - (1.06 \times 10^6)W\beta + (5.28 \times 10^7)Wd + (1.15 \times 10^6)f\alpha + \\
&\quad (1.40 \times 10^6)f\beta - (7.13 \times 10^7)fd - 20815\alpha\beta + 44167\alpha d + (7.25 \times 10^5)\beta d \\
&\quad -(7.74 \times 10^6)W^2 - (2.09 \times 10^7)f^2 + (1.24 \times 10^5)\alpha^2 - 13543\beta^2 - (8.70 \times 10^6)d^2 \\
&\quad -(4.84 \times 10^5)Wf\alpha - (2.74 \times 10^5)Wf\beta + (4.97 \times 10^6)Wfd - (4.00 \times 10^5)W\alpha d \\
&\quad -(1.75 \times 10^5)W\beta d + (6.63 \times 10^5)f\alpha d - (6.22 \times 10^6)W^2f + (3.66 \times 10^5)W^2\alpha \\
&\quad +(2.26 \times 10^5)W^2\beta - (3.59 \times 10^6)W^2d + (1.92 \times 10^5)Wd^2 + (3.66 \times 10^5)f^2\alpha \\
&\quad -(2.20 \times 10^6)f^2d - 9586f\alpha^2 + (1.99 \times 10^5)\alpha d^2 \\
&\quad +(4.81 \times 10^6)W^3 - 690\alpha^3 - (9.81 \times 10^5)d^3
\end{aligned} \tag{39}$$

Both the reduced quadratic and reduced cubic regression models display high linear correlation between the models and the response. Referencing Table 4.12 and Table 4.13 above, however, makes it clear that when compared with the experimental simulation results around the design points of optimal leakage rate, only the reduced quadratic regression model appreciably represents reality with an 8.17% and 10.15% difference from the simulation responses. The reduced cubic model reports predicted values for the cross-coupled stiffness coefficient with 64.44% and 88.41% error from the actual simulation responses. This indicates that a regression model of more than quadratic complexity is likely overfitting the data. Figure 4.23 shows the proportional strengths and signs of the correlations between the various factor effects and the cross-coupled stiffness response. The exit angle and groove depth are the

design variables with the most explanatory power. Figure 4.24 through Figure 4.26 show

response surface representations of the cross-coupled stiffness coefficient response based on

the chosen reduced quadratic regression model.
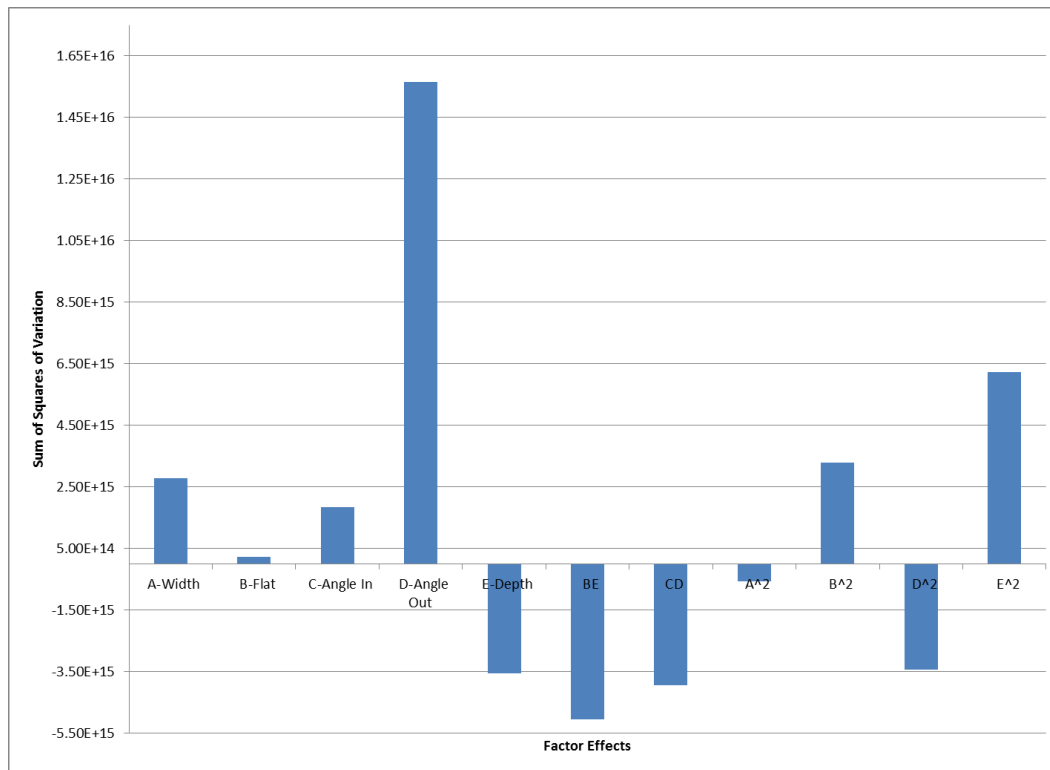
Figure 4.23: Pareto chart showing relative factor effects from the regression model for the cross-coupled stiffness coefficient response based on explained sums of squares of variation
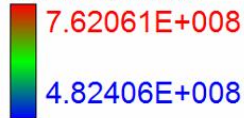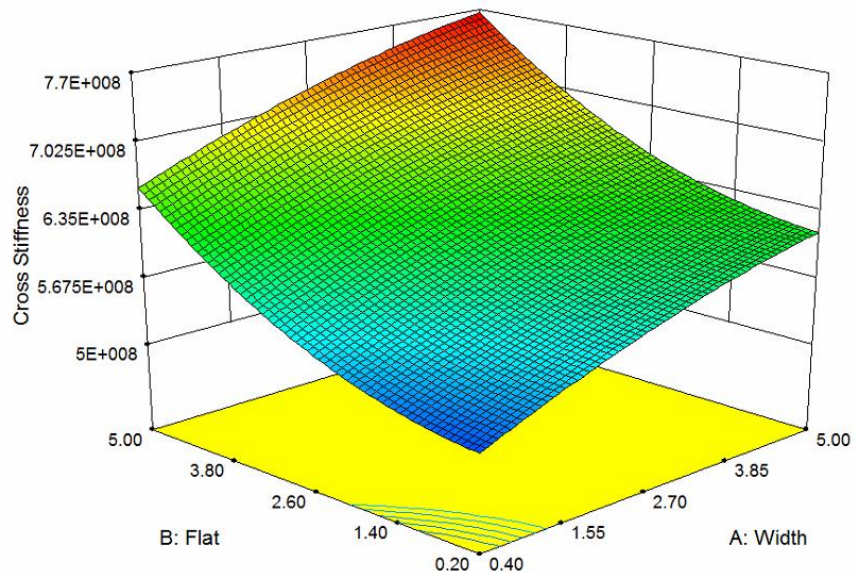
Figure 4.24: Quadratic regression model response surface of cross-coupled stiffness coefficient sensitivity near the predicted optimal design point, in terms of groove width and flat width
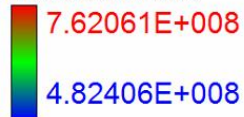
Figure 4.25: Quadratic regression model response surface of cross-coupled stiffness coefficient sensitivity near the predicted optimal design point, in terms of groove entrance and exit angles

Figure 4.26: Quadratic regression model response surface of cross-coupled stiffness coefficient sensitivity near the predicted optimal design point, in terms of groove width and depth

The largest cross-coupled stiffness response occurred in the simulation with the seal geometry optimized for minimum leakage rate. The smallest cross-coupled stiffness response occurred in the simulation of groove geometry number 13. Groove geometry 13 also corresponds to the highest observed leakage rate and direct stiffness. This, along with general trends in the data, suggests that any attempt to minimize leakage rate through changing seal groove geometry may be likely to increase the cross-coupled stiffness coefficient of the seal. Thus there is a tradeoff between efficiency of the turbomachine and its vibrational stability. This trend is also opposite to the trend just discussed for the direct stiffness coefficient response, which was reduced near the seal geometry of optimum leakage rate.

The second highest cross-coupled stiffness among the flow visualized simulations was the result of the geometry used in groove geometry number 7. The geometry of groove geometry number 7 has a much larger flat width, than the geometry of minimum leakage rate,

and a smaller groove depth. Based on the response surfaces shown above, this would suggest an increase in cross-coupled stiffness rather than the slight decrease actually observed. However, the reduced quadratic regression model predicts within 2.89% of the actual response resulting from the simulation. Thus interaction factor effects between design variables not connected in the above response surfaces are responsible for the seemingly unexpected behavior.

The trends, seen in Figure 4.25, relating reduction in groove entrance and exit angles to a reduction of the cross-coupled stiffness coefficient are supported by the responses of groove geometry numbers 27, 74 and 81. The geometry, with reduced entrance angle and a middle value of exit angle, in groove geometry number 81 is the next highest response of cross-coupled stiffness. This larger increase in response from groove geometry number 27 to 81, compared to the increase between 27 and 74, supports indications in the Pareto chart, Figure 4.23, that the effect of groove exit angle is stronger than the other design variables. REASON WHY

The lowest cross-coupled stiffness responses, observed in the flow visualization examples, occur when the fluid in the jet flow region is not allowed to expand very far into the groove cavity. The baseline simulation and groove geometry number 28 are examples of this, where the large recirculation vortices create flow boundaries approximating a plain seal instead of a labyrinth seal.

Direct Damping Coefficient

At better than a 99% confidence level, sequential sum of squares analysis supports the potential effectiveness of both a quadratic and cubic regression model. The full 21-parameter quadratic model was analyzed and refined first with ANOVA and backwards elimination of factor effect parameters individually found not significant at a confidence level greater than 90%. The resulting 13-parameter model, shown in Equation 40, includes the intercept parameter, all five first-order factor effect parameters, two two-factor interaction effect parameters and four of the five second-order factor effect parameters. The three coefficients of determination for this reduced quadratic model are 0.902, 0.888, and 0.846 respectively for the standard, adjusted and predicted values. These R^2 values indicate that the fitted model is explaining the variation in the response well.

$$C_{XX} = 2.23 \times 10^5 + 14478\text{W} + 4477\text{f} + 697.91\alpha$$
$$+ 2058\beta - 9542\text{d} + 82.83\text{W}\beta - 2645\text{fd} - 13.35\alpha\beta$$
$$-1268\text{W}^2 + 2676\text{f}^2 - 10.73\beta^2 + 1418\text{d}^2 \tag{40}$$

The same model reduction procedure was performed on a full cubic regression model. A reduced cubic regression model, shown in Equation 41, was formulated of the 37 parameters found individually significant at or above a 90% confidence level, or necessary to maintain model hierarchy. The six insignificant factor effect parameters included for hierarchical reasons represent the second-order factor effect of groove entrance angle, the two-factor interaction effects of groove depth with the entrance and exit angles, the two-factor interaction effects combining the groove width and flat width with the exit angle, and the first-order factor effect representing groove depth. Together the individually significant and insignificant parameters of

the reduced cubic regression model explain 98.2% of the variation in direct damping coefficient about the mean response. Adjusted and predicted R^2 values of 0.972 and 0.917 respectively, demonstrate that the majority of the parameters add value and accuracy of prediction to the regression model.

$$\begin{aligned}
C_{XX} = {} & 81662 + (1.83 \times 10^5)W - 98100f + 1965\alpha + 1097\beta - 16908d \\
& + 50622Wf - 1121W\alpha - 322W\beta + 22484Wd + 899f\alpha + 353f\beta - 32824fd - 8.85\alpha\beta \\
& - 65\alpha d - 105\beta d - 48650W^2 - 9488f^2 + 2.30\alpha^2 - 4666d^2 - 182Wf\alpha - 155Wf\beta \\
& + 2090Wfd - 238W\beta d + 162f\alpha d + 152f\beta d - 3835W^2f + 160W^2\alpha + 150W^2\beta - 1921W^2d \\
& + 1088Wd^2 + 155f^2\alpha - 776f^2d - 5.48f\alpha^2 + 143\beta d^2 + 3360W^3 - 736d^3
\end{aligned} \qquad (41)$$

Similarly to the cross-coupled stiffness coefficient response, the reduced quadratic and cubic regression models for the direct damping coefficient response are both highly linearly correlated with the response data. The benchmarking of these regression models shown in Table 4.12 and Table 4.13 above suggests that the reduced cubic model's predictions might be slightly more representative of the true response. The third-order model appears to enjoy an accuracy margin of a few percent over the reduced quadratic model, though the error of the quadratic model in prediction of the direct damping coefficient response was more consistent over both simulations. Some care should be taken in case the chosen reduced cubic model's prediction accuracy continues to diverge as other areas in the design space are investigated. Figure 4.28 through Figure 4.30 show response surface plots of the reduced cubic regression model over the domain and Figure 4.27 shows the relative contributions of the factor effects to explaining the data's variation about its mean. The groove entrance and exit angles appear to have the least effect on the direct damping coefficient response.

Figure 4.27: Pareto chart showing relative factor effects from the regression model for the direct damping coefficient response based on explained sums of squares of variation
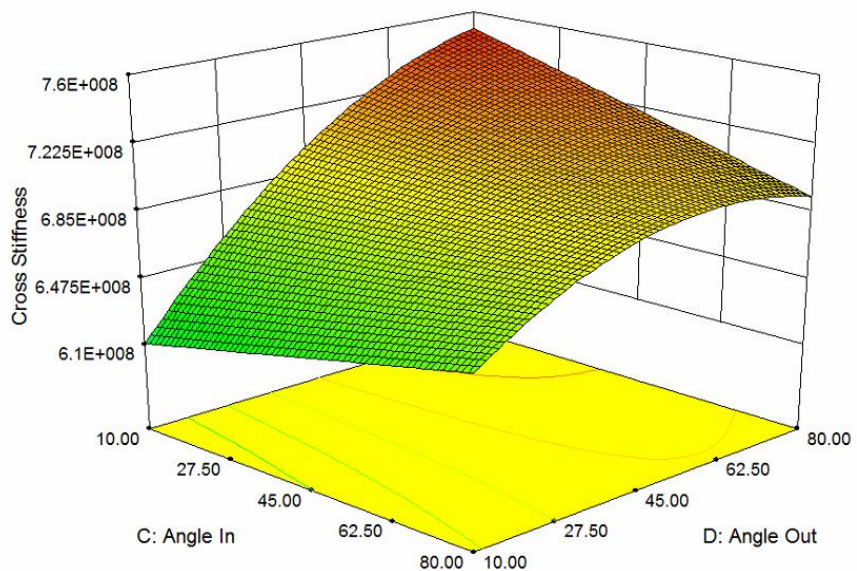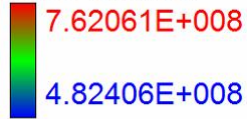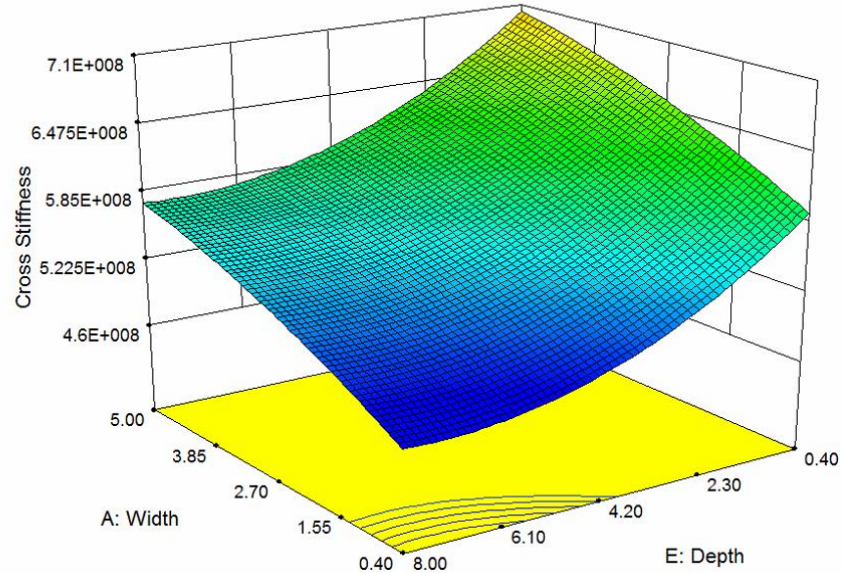

Figure 4.28: Cubic regression model response surface of direct damping coefficient sensitivity near the predicted optimal design point, in terms of groove width and flat width

Figure 4.29: Cubic regression model response surface of direct damping coefficient sensitivity near the predicted optimal design point, in terms of groove entrance and exit angles

Figure 4.30: Cubic regression model response surface of direct damping coefficient sensitivity near the predicted optimal design point, in terms of groove width and depth

As with the cross-coupled stiffness response, the largest direct damping response corresponded to the seal groove geometry that causes minimum leakage rate. The minimum direct damping response also was observed in the simulation for groove geometry number 13. The previously mentioned tradeoff of reduced leakage rate, and direct stiffness, increasing the cross-coupled stiffness appears to also include increasing direct damping. However, the response surface plots for describing the two responses exhibit mostly different curvature, and in a few cases different general trends. Only the groove entrance angle response curvature is the same between the responses. Despite the differences in response surfaces, the ranking of the responses of the simulations chosen for flow visualization is nearly identical.

The second highest direct damping response is observed for groove geometry number 7, with an increased flat width compared to the geometry of minimum leakage rate. The third highest from groove geometry number 36, the fourth through sixth highest from geometries 81, 74 and 27, and the lowest response from the baseline geometry and groove geometry number 28. This ranking of the geometries also corresponds to the ranking of the apparent average groove pressure from Figure 4.16.

Cross-coupled Damping Coefficient

The sequential sum of squares F-test only found the quadratic model for the cross-coupled damping coefficient response significantly different from zero at or above the 94% confidence level. Like the direct stiffness coefficient response the three coefficients of determination, for the full quadratic regression model, also cover a broader range from the standard R^2 of 0.877 to the predicted value of 0.681. ANOVA and backwards elimination of

individual terms not significant at above 90% confidence levels results in a decrease in the standard R^2 to only explaining 86.6% of the response's variation about its mean, but an increase of the predicted R^2 to 0.734. The 14-paramter reduced quadratic regression model is shown in Equation 42 with the calculated parameter estimates.

$$C_{XY} = 32700 + 684W - 1530f - 67.20\alpha - 48.20\beta$$
$$- 849.69d - 10.68W\alpha - 16.53W\beta + 17.72f\beta + 0.68\alpha\beta$$
$$+ 16.06\beta d + 146.96W^2 + 0.57\alpha^2 - 67.95d^2 \qquad (42)$$

The full cubic regression model was found significant by the sequential sum of squares analysis at better than 99% confidence. Refining of the cubic model to only include terms statistically significant above a 90% confidence level reduced the number of regression parameters to 41. The selected parameters formulate a reduced cubic regression model given by Equation 43. Accounting for model hierarchy requirements, six factor effect parameters were retained by the model despite failure to be found individually significant above a 90% confidence level. These parameters correspond to groove exit angle, groove depth, the two-factor interactions of the groove width and flat width with the exit angle, the two factor interaction of the entrance angle and the depth, and the squared entrance angle. Despite the individual insignificance of six parameters, the entire 41-parameter model displays good linear correlation and fit to the response data. The three coefficients of determination for the reduced cubic regression model range from 0.985 to 0.847.

$$C_{XY} = 45504 - 15262W + 8472f - 186\alpha + 85.2\beta + 605d$$
$$- 4485Wf + 124W\alpha + 18.29W\beta - 3189Wd - 115f\alpha - 0.81f\beta + 2770fd + 0.97\alpha\beta$$
$$- 21.29\alpha d + 95.24\beta d + 4452W^2 + 1111f^2 + 0.14\alpha^2 - 3.94\beta^2 + 744d^2 + 29.56Wf\alpha$$

$$+9.42Wf\beta - 167Wfd + 12.05W\alpha d + 17.95W\beta d - 11.22f\alpha d - 14.31f\beta d - 0.43\alpha\beta d$$
$$+253W^2f - 22.34W^2\alpha - 10.69W^2\beta + 195W^2d - 71.02Wd^2 - 14.56f^2\alpha + 0.30f\alpha^2$$
$$-0.42\beta^2 d - 10.42\beta d^2 - 263W^3 + 0.025\beta^3 + 27.72d^3 \qquad (43)$$

Upon comparison of the two regression model's predictions of the cross-coupled damping coefficient response to the actual responses of the two additional simulation experiments, in Table 4.12 and Table 4.13, the two regression models appear to have approximately equal predictive capability. Occam's razor and the exact errors between the predicted and simulated responses suggest that the reduced quadratic regression model should be used to model this response. The chosen regression model is shown as a response surface in Figure 4.32 to Figure 4.34 below, with a Pareto chart showing the relative explanation of the response's variation about its mean from each factor effect, Figure 4.31. Based on the Pareto chart, the most significant design variables relating to this response are the groove flat width and the groove depth. The trends observed in the response surfaces below are similar to those for the direct stiffness coefficient and the subsequent direct mass coefficient responses. Additionally, the simulations characterized by maximum and minimum direct stiffness coefficient responses correspond to near maximum and minimum cross-coupled damping and direct mass coefficient responses. Because the remaining rotordynamic coefficients are not critical to stability, and because of the similarities to previously discussed results, the response surface trends will not be discussed separately.
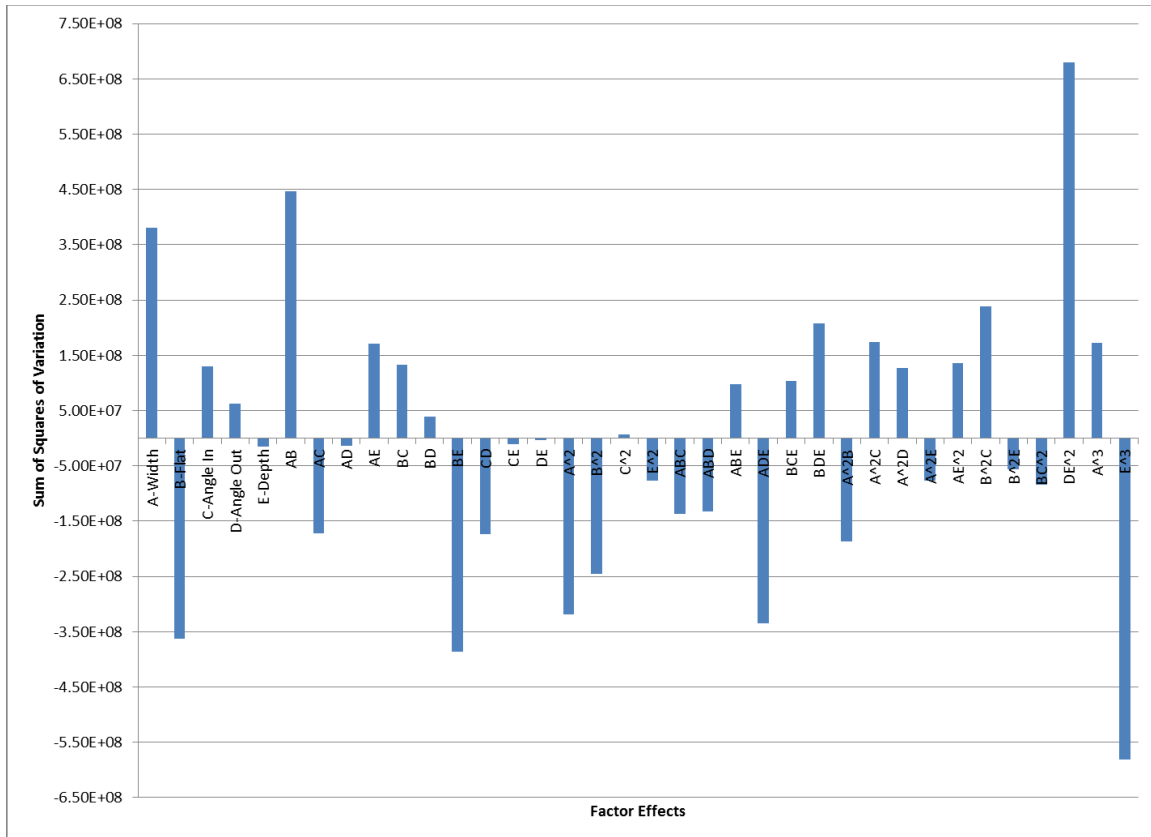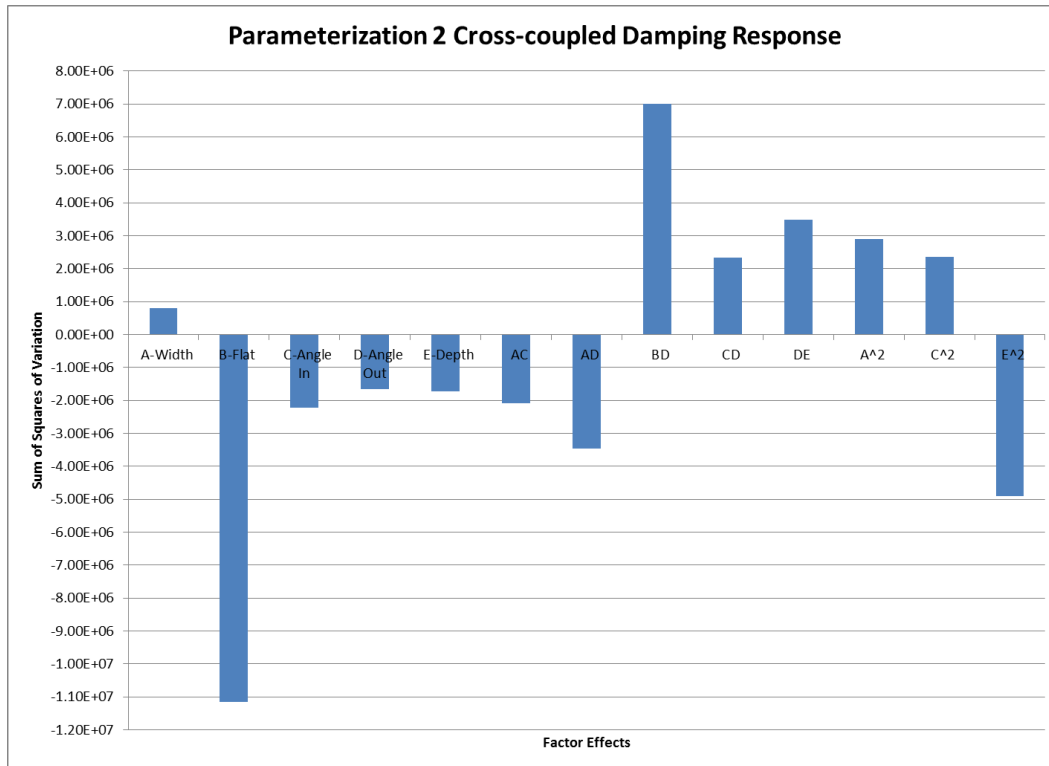
Figure 4.31: Pareto chart showing relative factor effects from the regression model for cross-coupled damping coefficient response based on explained sums of squares of variation
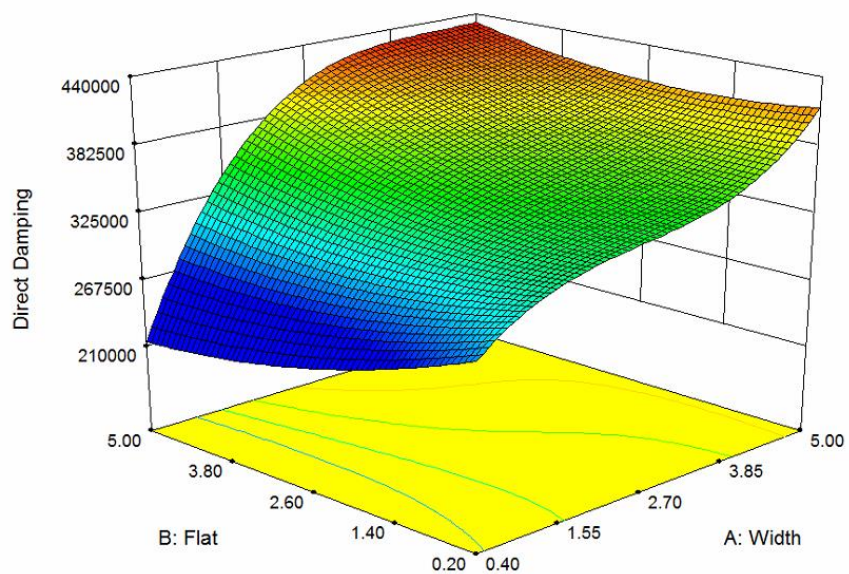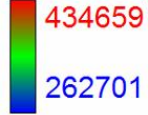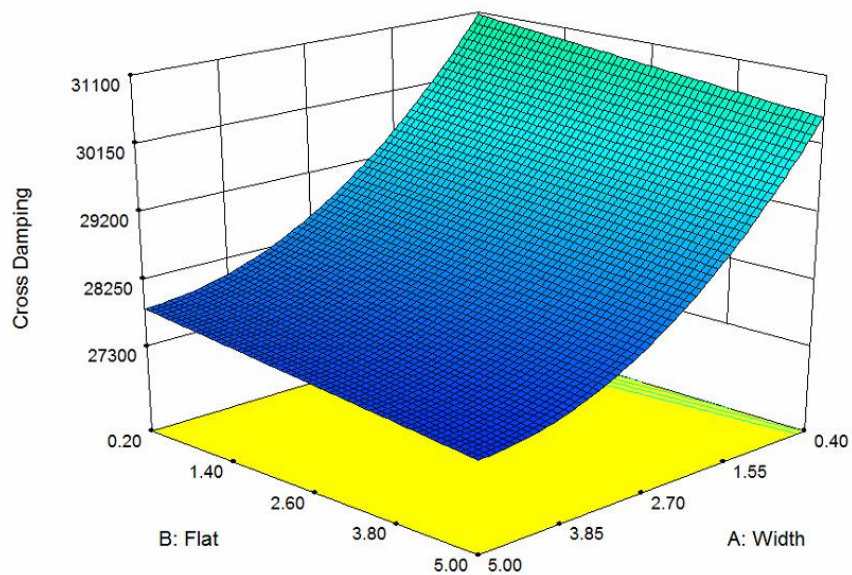

Figure 4.32: Quadratic regression model response surface of cross-coupled damping coefficient sensitivity near the predicted optimal design point, in terms of groove width and flat width
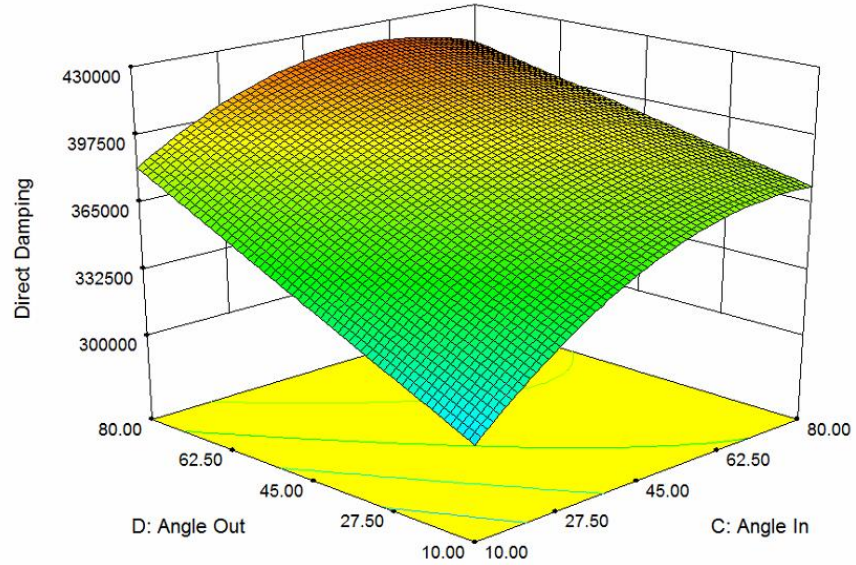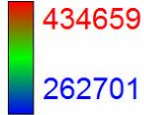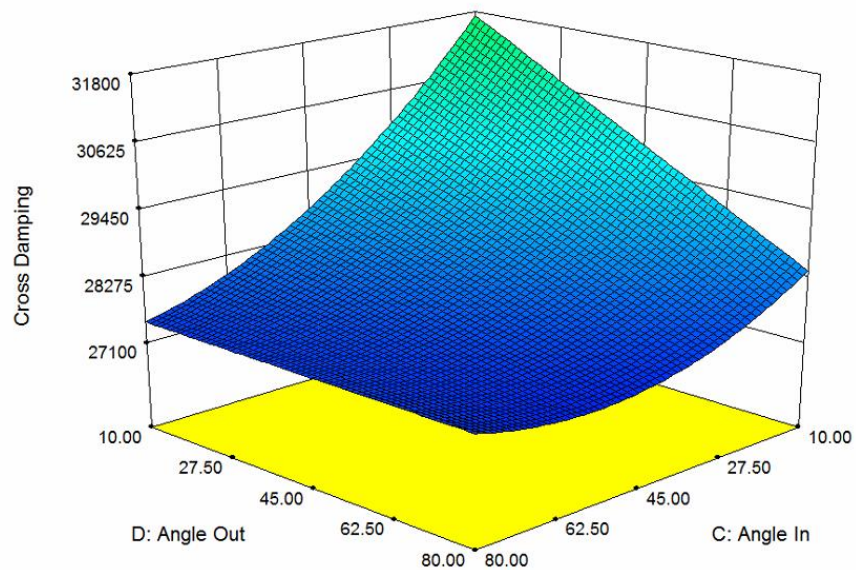
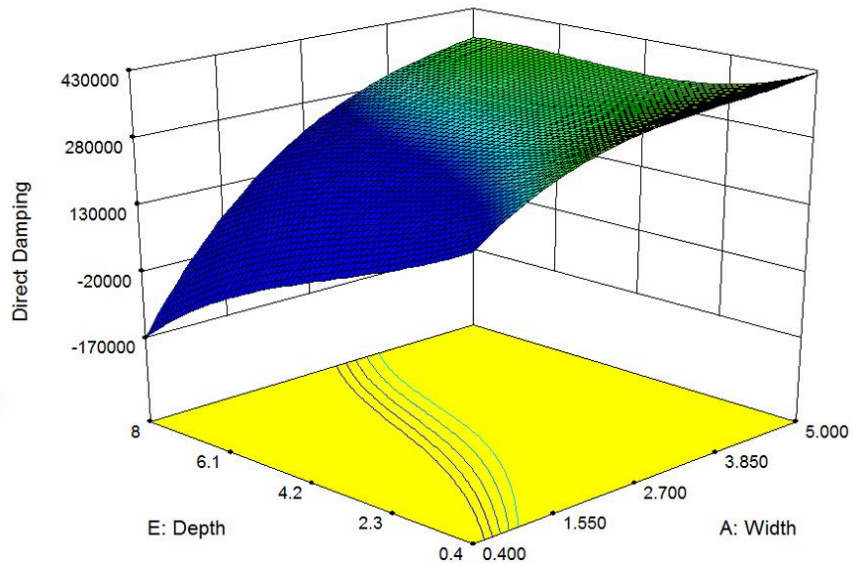Figure 4.33: Quadratic regression model response surface of cross-coupled damping coefficient sensitivity near the predicted optimal design point, in terms of groove entrance and exit angles
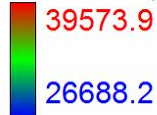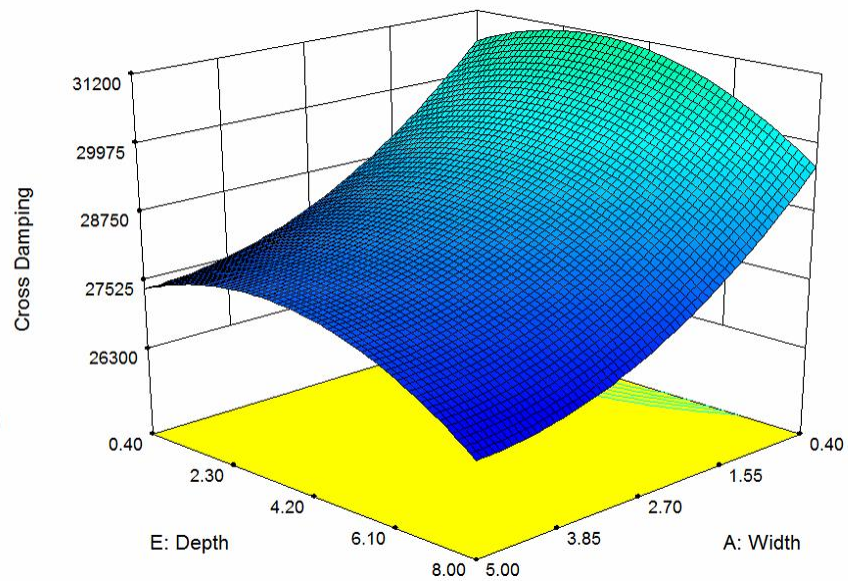
Figure 4.34: Quadratic regression model response surface of cross-coupled damping coefficient sensitivity near the predicted optimal design point, in terms of groove width and depth

Direct Mass Coefficient

Unlike the previously analyzed responses, the sequential sum of squares F-test did not find that the full quadratic regression model was significant except above a 56% confidence level. However, a model consisting of the first-order factor effects and all two-factor interactions the full cubic regression model was found significant at better than 99% confidence. Because both higher and lower hierarchy models are potentially significant, a full quadratic model was still investigated through ANOVA and backwards elimination of terms that fail to be found significant at a 90% confidence level. Expectedly, the majority of the second-order factor effect parameters were not found significant. Neither were seven out of the ten two-factor interaction effect parameters. The resulting 10-parameter reduced quadratic regression model is given in Equation 44 and consists only of terms found individually significant. This model fits the response data with reasonable linear correlation, explaining 75.6% of the variation in the response about its mean. The adjusted and predicted coefficients of determination are acceptably close to the standard R^2 to confirm the model's reasonableness.

$$M_{XX} = 14.65 + 0.043W - 0.18f - (1.33 \times 10^{-3})\alpha - 0.012\beta + 0.032d$$
$$-(1.33 \times 10^{-3})W\alpha + 0.043fd + (1.71 \times 10^{-4})\alpha\beta - (8.86 \times 10^{-3})d^2 \qquad (44)$$

A 39-parameter reduced cubic model was also produced by the same methodology, shown in Equation 45. Again four factor effect parameters are included in the regression model to maintain hierarchy, having failed to be found significant at a minimum confidence level of 90%. These rejected factor effect parameters correspond to the first-order factor effect

parameter associated with groove exit angle and three two-factor interaction effect parameters. The reduced cubic regression model proposes to explain 96.4% of the variation in direct-mass coefficient response about its mean. The adjusted R^2 of 0.941 indicates that there are few parameters included which do not carry their own weight and a predicted R^2 of 0.822 suggests an acceptable ability to predict the response of the tested data points.

$$\begin{aligned}
M_{XX} = {}& 16.39 - 2.58W + 0.77f + 0.042\alpha + (9.81 \times 10^{-3})\beta - 0.81d - 0.70Wf \\
& + (7.56 \times 10^{-3})W\alpha + (8.89 \times 10^{-3})W\beta - 0.31Wd - (2.10 \times 10^{-3})f\alpha + (6.72 \times 10^{-3})f\beta \\
& + 0.19fd - (7.18 \times 10^{-4})\alpha\beta + 0.034\alpha d + 0.016\beta d + 0.69W^2 + 0.23f^2 - (9.68 \times 10^{-4})\alpha^2 \\
& - (3.00 \times 10^{-4})\beta^2 - 0.080d^2 + (3.61 \times 10^{-3})Wf\alpha + (2.00 \times 10^{-3})Wf\beta \\
& + (3.96 \times 10^{-3})W\alpha d - (2.89 \times 10^{-3})f\alpha d - (1.90 \times 10^{-4})\alpha\beta d + 0.035W^2f \\
& - (2.62 \times 10^{-3})W^2\alpha - (2.57 \times 10^{-3})W^2\beta + (7.71 \times 10^{-5})W\beta^2 - (2.23 \times 10^{-3})f^2\beta \\
& - (1.46 \times 10^{-3})f^2\beta + 0.014f^2d - (8.67 \times 10^{-5})f\beta^2 + (7.91 \times 10^{-6})\alpha^2\beta \\
& - (2.48 \times 10^{-4})\alpha^2d - 0.032W^3 + (5.29 \times 10^{-6})\alpha^3 + (5.11 \times 10^{-3})d^3
\end{aligned} \qquad (45)$$

The results of the additional simulation experiments, given in Table 4.12 and Table 4.13 above, agree with the predictions of both the reduced quadratic and reduced cubic regression models approximately equally. The average error of the two comparisons hints that the cubic model might have marginally greater prediction accuracy, however any gains in accuracy can be assumed to be very slight. The reduced quadratic regression model is selected for its greater simplicity while maintaining equivalent prediction accuracy. Figure 4.36 through Figure 4.38 below show this model plotted over the design space. The Pareto chart in Figure 4.35 suggests that variations in groove flat width and groove exit angle explain the majority of the direct mass coefficient's variation about its mean.
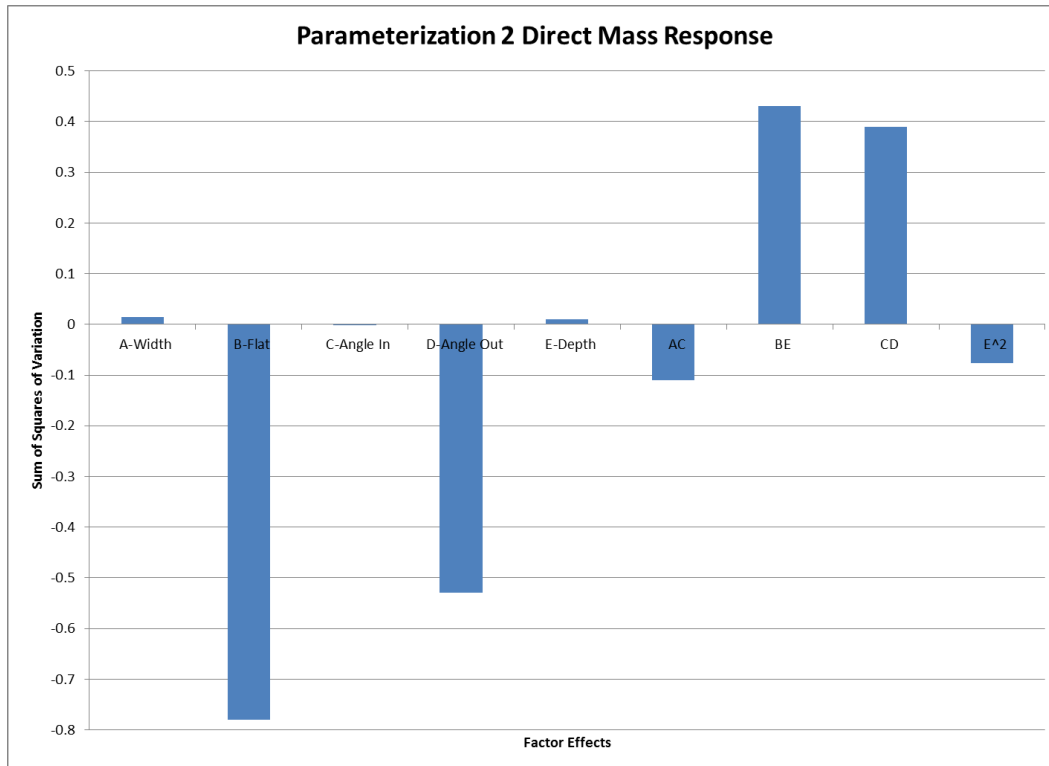
Figure 4.35: Pareto chart showing relative factor effects from the regression model for direct mass coefficient response based on explained sums of squares of variation
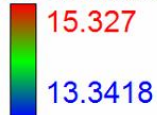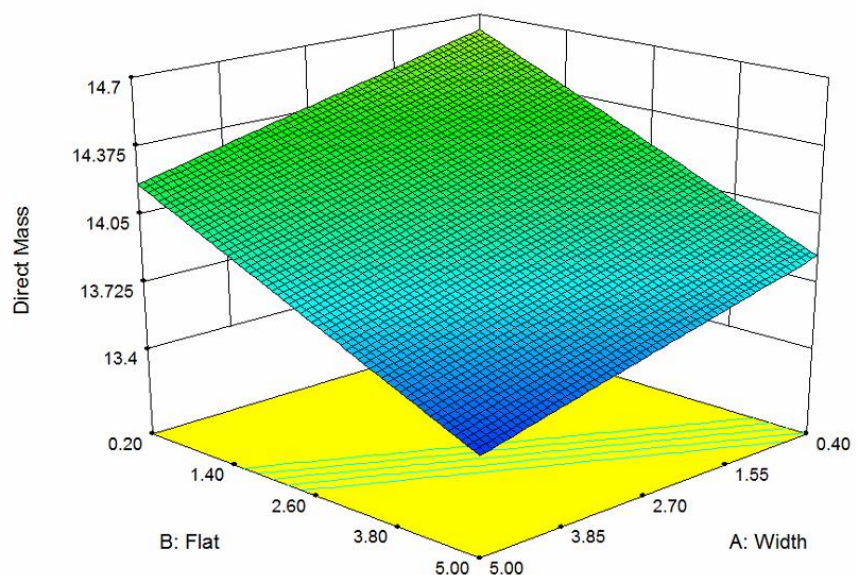
Figure 4.36: Quadratic regression model response surface of direct mass coefficient sensitivity near the predicted optimal design point, in terms of groove width and flat width
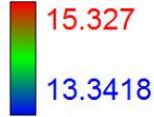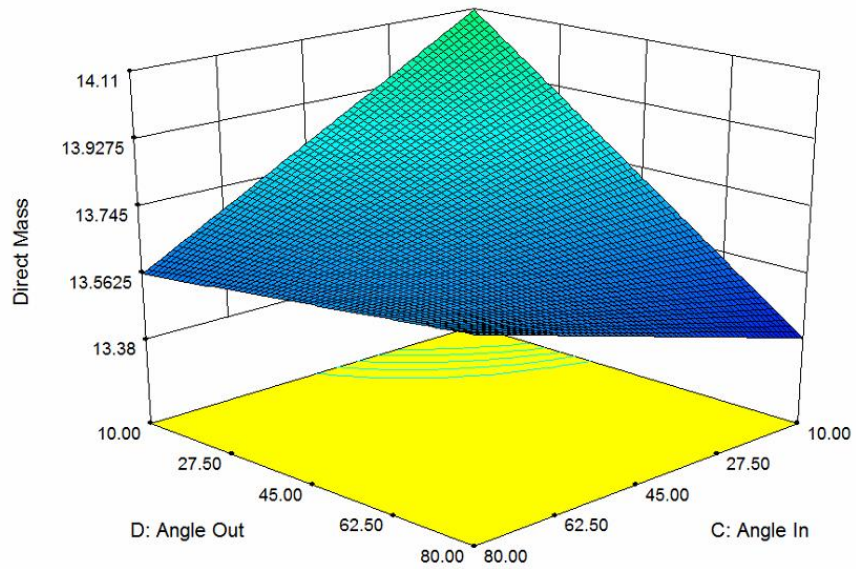
Figure 4.37: Quadratic regression model response surface of direct mass coefficient sensitivity near the predicted optimal design point, in terms of groove entrance and exit angles
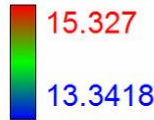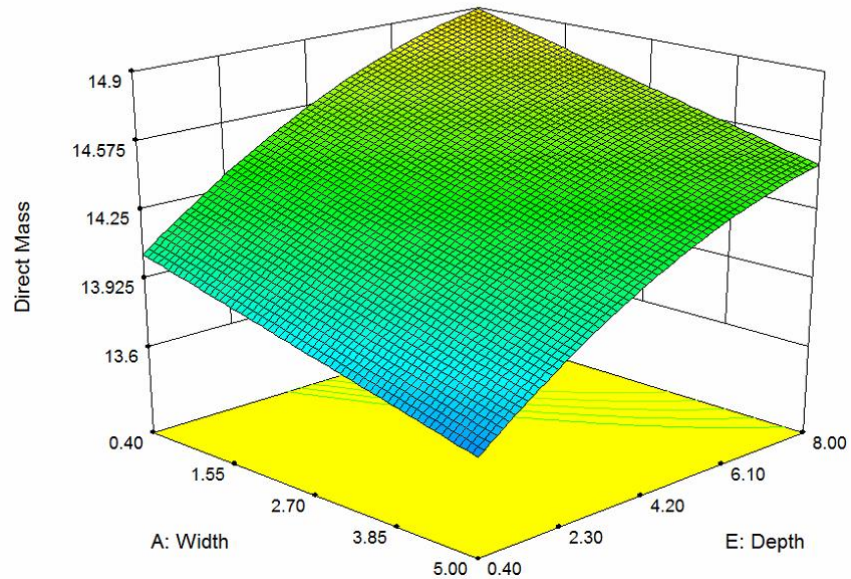
Figure 4.38: Quadratic regression model response surface of direct mass coefficient sensitivity near the predicted optimal design point, in terms of groove width and depth

Cross-coupled Mass Coefficient

Unique among the responses for this parameterization and experimental design, no regression model more complicated than the 6-parameter model consisting of the intercept and first-order factor effects was found to significantly fit the cross-coupled mass coefficient response based on sequential sum of squares analysis. Additionally, the predicted coefficients of determination for more complex regression models were found to be negative, indicating no confidence in their capability to predict the responses of data points examined in the experimental design, let alone ability to predict responses associated with other areas of the design space. ANOVA was performed on the full first-order factor effects model and the groove width and flat width both failed to be found significant above a 90% confidence level. The remaining 4-parameter regression model, and the associated parameter estimates, is given in Equation 46. While, the model is statistically significant above a 99% confidence level, it only proposes to explain 22.1% of the response data's variation about its mean. Associated adjusted and predicted R^2 values of 0.196 and 0.149 respectively, confirm the likely significance of the included parameters. However, the low standard coefficient of determination suggests that the response is dependent on effects due to unmodeled factors as well as the few factors of the parameterization that fit the response. Due to the simplicity of this model no response surface plots were produced.

$$M_{XY} = 0.11 + (3.07 \times 10^{-3})\alpha - (2.56 \times 10^{-3})\beta - 0.016d \qquad (46)$$

4.5 Comparison of Parameterizations

The regression model for the leakage rate response associated with the second parameterization predicted the lowest leakage rate among the potential seal geometries. The

second parameterization DOE also tested larger variations in seal geometry than allowed by the first parameterization. However, the regression models found to fit the response data for the first parameterization DOE's were more accurate at predicting the responses of the design point predicted to have optimal leakage rate. The simplicity of the reduced quadratic and first-order linear regression models fit to the response data of the first parameterization also made it easier to associate potential physical mechanisms to the response behavior. Both parameterization studies provided insight into the relationships between groove shape and scale parameters and seal performance characteristics, and are thus useful to the design and further optimization of annular labyrinth seal geometries.

CHAPTER 5: CONCLUSIONS AND FUTURE WORK

This study has demonstrated the application of experimental design and multiple regression modeling to the investigation of annular seal groove shape and scale factors on seal performance characteristics. For the first parameterization, a 21-parameter model was refined to 11 parameters, resulting in a strong linear correlation between the regression model representing groove scale factors and the leakage rate response. This model provides information on the sensitivity of leakage rate to groove scale and suggests a seal geometry with a predicted minimum leakage rate. Regression models were also obtained for the seal's rotordynamic coefficients. The regression models for the response seal performance characteristics suggest some general trends relating the groove radii scale to each response, shown in Table 5.1. The flow rate is at a minimum with groove radii near 4 mm. The regression equations for the other responses were linear, with the direct stiffness and direct mass coefficients exhibiting an inverse correlation and the remaining coefficients a direct correlation A second stage of experiments was performed to verify the location of design point having predicted optimum leakage rate and refine the regression models' sensitivity in the region around the predicted optimum. The combination of the response data from these DOE's allowed the formulation of new regression models with enhanced prediction accuracy over original regression models.

Table 5.1: Trends from 1st parameterization

R_j	Q	K_{XX}	K_{XY}	C_{XX}	C_{XY}	M_{XX}	M_{XY}
↑ (>4mm)	↑	↓	↑	↑	↑	↓	–
↑ (<4mm)	↓	↓	↑	↑	↑	↓	–
↓ (>4mm)	↓	↑	↓	↓	↓	↑	–
↓ (<4mm)	↑	↑	↓	↓	↓	↑	–

A second parameterization of the baseline seal geometry was investigated to identify an optimal groove shape. Both reduced quadratic and reduced cubic regression models were found to fit the seal performance responses. The design points of predicted optimum leakage rate were investigated for each order of regression model and used as a benchmark to select the most accurate regression model for each response. For both parameterizations the seal leakage rate was improved over that of the base seal and sensitivity information covering the design space is provided by the regression models for each seal performance response.

Figure 5.1 shows one dimensional relationships between each design variable and the seal performance responses. The range allowed for each design variable is plotted against the various seal performance responses normalized by the responses associated with the baseline seal groove geometry. Each figure is applicable only near the values of the design variables being held constant at the levels associated with the seal groove geometry of minimum leakage rate. The trends visible in these plots are not constant if other design variables are changed due to the strong two and three factor interaction effects present in the regression models. For more complete information on trends relating the design variables to the seal performance characteristics, refer to the response surfaces in the chapter four or the regression models themselves.
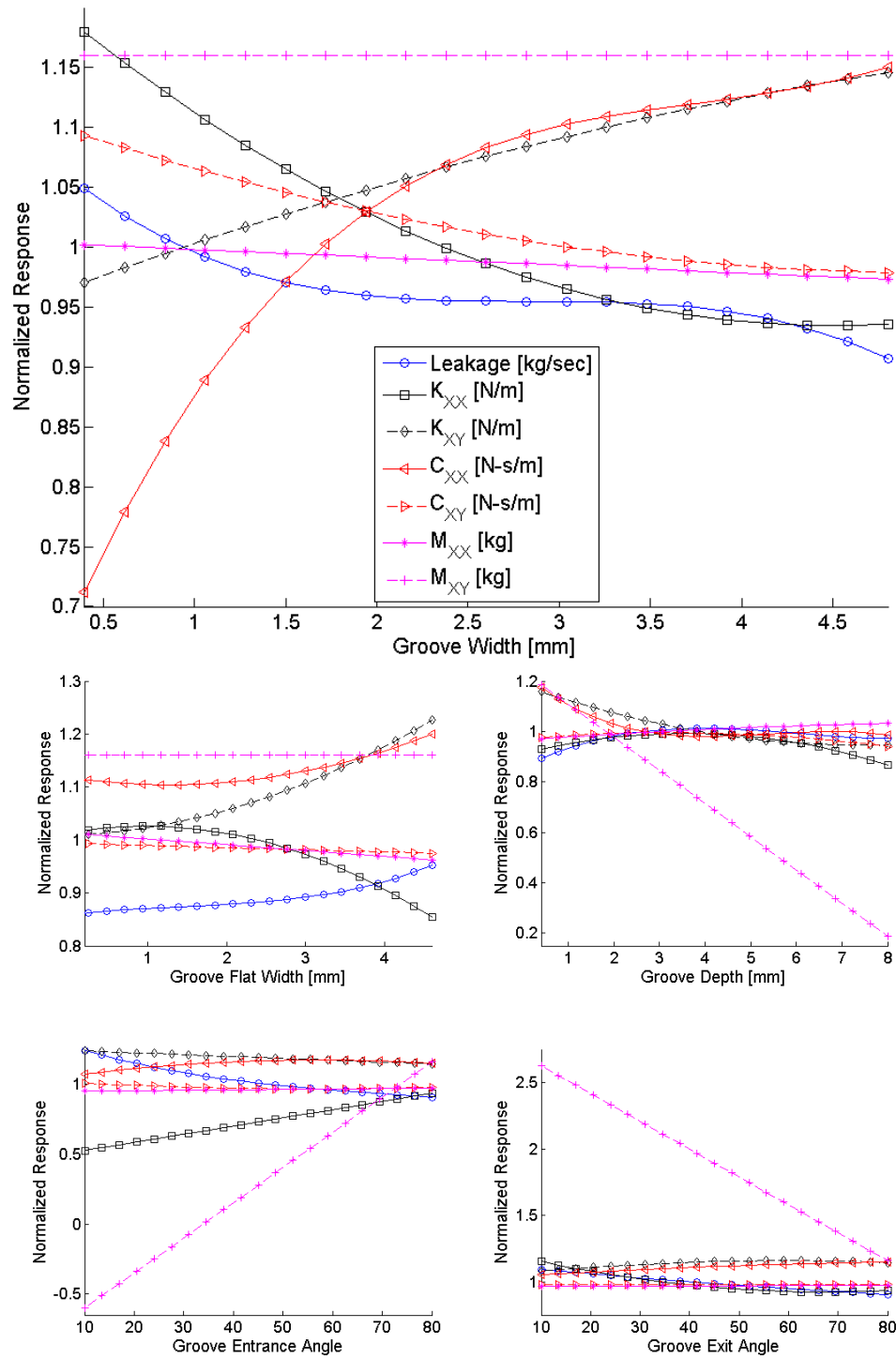
Figure 5.1: One-dimensional relationships between the second parameterization design variables and the seal performance responses, for the optimal leakage rate geometry and normalized by the baseline seal responses
W=4.8 mm, f=3.6 mm, α=80, β=80, d=0.59 mm

Starting from the seal geometry found to have minimum leakage rate, decreasing groove width increases the leakage rate. As the leakage rate increases, direct stiffness and cross-coupled damping increases quadratically, the cross-coupled stiffness decreases linearly, direct damping decreases quadratically, and the mass coefficients remain largely unchanged. As the flat width is increased, leakage, cross-coupled stiffness, and direct damping increase quadratically; while direct stiffness decreases quadratically. The flat width has little effect on the cross-coupled damping coefficient or the mass coefficients. The effects of groove depth are characterized by shallow convex parabolas for leakage rate, direct stiffness, and both damping coefficients, with maxima near a depth of 4 mm for each response. Cross-coupled stiffness decreases gradually with increased groove depth, and the cross-coupled mass coefficient exhibits a large linear decrease. Changes in both the entrance and exit angles cause small variations in the cross-coupled stiffness and damping and the direct mass coefficients. Leakage rate decreases quadratically with increases in both angles at approximately the same rate. There is more variation in direct damping from the groove entrance angle than the exit angle but both have a positive correlation. The largest differences between the effects of each angle are seen in the direct stiffness and cross-coupled mass coefficients. The entrance angle is positively correlated with direct stiffness with variation down to near 50% of the baseline seal response at low angles, while the exit angle exhibits a negative correlation from approximately 120% of the baseline response at low angles to about 80% at high angles. The cross-coupled mass coefficient seems most strongly affected by the two angles with a positive correlation to entrance angle and a negative correlation to exit angle.

The geometry associated with minimum leakage rate also exhibited near minimum direct stiffness, near maximum cross-coupled stiffness, and near maximum direct damping. This suggests that shallow rectangular grooves best minimize leakage rate and direct stiffness, while maximizing direct damping. Correspondingly, seal groove geometry number 13, which has the highest leakage rate, displays the highest direct stiffness, the lowest cross-coupled stiffness, and the lowest direct damping. Seal groove geometry number 13 is a triangular groove with a wide base and shallow entrance and exit angles. These maxima and minima, along with the regression trends discussed previously, suggest that a prospective seal designer will have to accept a potential tradeoff of decreased vibrational stability for reductions in leakage rate through the seal. This demonstrates the viability of the application of design of experiments and multiple regression to annular labyrinth seal design.

Although design spaces of greater than three factors can be difficult to visualize, compared to iterative design methods, this approach more broadly spans the potential design space and may provide combinations of factors that are not intuitive. Every additional experiment increases knowledge of the design space and allows the testing of more complex models to describe system behavior. While computationally expensive these simulations can be less time consuming than a pure optimization routine because the DOE simulations can be run simultaneously.

The next iteration of the work discussed in this thesis begins with the addition of more simulation response data to the library being used to generate the least-squares regression models. The selection of new design points, at which to perform simulation experiments, could

be done by experimental designs or optimization algorithms, with or without regression analysis. New experimental designs would be selected to focus on areas of the current design space where experiments have not yet been performed, or to expand the limits currently set on the design variables. New limits could be imposed on the second parameterization design variables to allow new groove shapes such as parallelograms or inverted trapezoids. Alternatively, multiple optimization algorithms could be used to select new design points with goals such as confirmation of the current geometry associated with minimum leakage as a global minimum, or to meet the requirements of an objective function that selects for preferable rotordynamic coefficients, for a given system, as well as leakage rate. Optimization algorithms such as genetic algorithms, artificial neural networks, or simplex optimization could then be compared for convergence speed and agreement on global minima.

Verification of the validity of this study's rotordynamic coefficients could be performed by calculating the rotordynamic stiffness coefficients from full 360° seal CFD models that include rotor eccentricity. Verification could also be obtained by accumulation and regression analysis of experimental seal performance data for similar groove shapes, or experimental testing of the seal groove shapes simulated in this thesis. Simulation experiments could be performed on a plain seal with the same overall geometry to see if the intercept parameters from the regression models correspond to their responses. Additionally, simulation error can be estimated by starting the CFD simulations from multiple random initial conditions, or through comparison with physical experiment.

In future studies, more geometric effects on seal leakage rate could be explored through the generation of additional geometric parameterizations of labyrinth seal grooves. The more general the parameterization the more information the regression model can provide about the sensitivity of leakage rate to geometric factors along a labyrinth seal. In particular, a large study investigating the effects of allowing each of the 20 grooves in the baseline seal to vary by scale, or varying the spacing between grooves would identify seal performance responses that are affected by the groove's axial location. Individual groove scales could be allowed to vary with a converging or diverging axial pattern to reduce the number of design variables. Groove cavity geometry could be defined by horizontal and vertical coordinates specifying points on a spline curve to allow wild variations in groove cavity geometry. Image processing could be used to track the center coordinates of the groove cavity vortices and regression models applied to link geometric design variables to vortex properties. Finally, the methods herein could be applied to more complex stepped labyrinth seals, other non-labyrinth annular seal geometries, to compare seals with different working fluids and operating conditions, or to other turbomachinery flow problems such as journal bearings or squeeze film dampers.

Learning processes have been characterized as an iterative inductive/deductive cycle [32]. Data are gathered and, by a process of induction, ideas (a model) are generated to explain them. New hypotheses (predictions of the model) are generated by deduction. More data are gathered and the cycle continues. This process is a never ending refinement on the present understanding. This study proposed an alternate approach for investigating the effects of various geometric factors on leakage rate for balance drum seals. A systematic experimental

design was conducted to investigate the effects of five factors on leakage rate of a selected seal model. The fitting of linear models and analysis of variance of those results have revealed the significant geometric factor effects of the parameterized seal geometries. These results provide information that could be used to guide further experimentation in this design space to achieve an improved seal design.

WORKS CITED

[1] D. Childs, Turbomachinery Rotordynamics, New York, NY: John Wiley & Sons, Inc., 1993.

[2] A. A. Lomakin, "Calculation of critical speed and securing of dynamic stability of the rotor of hydraulic high pressure machines with reference to forces arising in the seal gaps," *Energomashinostrojenie,* vol. 4, pp. 1-5, 1958.

[3] H. F. Black, "Effects of Hydraulic Forces in Annular Pressure Seals on the Vibrations of Centrifugal Pump Rotors," *Journal of Mechanical Engineering Science,* vol. 11, no. 2, pp. 206-213, 1969.

[4] P. J. Migliorini, A. Untaroiu, H. G. Wood and P. E. Allaire, "A Computational Fluid Dynamics/Bulk-Flow Hybrid Method for Determining Rotordynamic Coefficients of Annular Gas Seals," *Journal of Tribology,* vol. 134, no. 2, April 2012.

[5] G. G. Hirs, "A Bulk-Flow Theory for Turbulence in Lubricant Films," *Journal of Lubrication Technology,* vol. 95, pp. 137-146, April 1973.

[6] C. C. Nelson, "Rotordynamic Coefficients for Compressible Flow in Tapered Annular Seals," *Transactions of the ASME,* vol. 107, pp. 318-325, July 1985.

[7] M. Arghir and J. Frêne, "Rotordynamic Coefficients of Circumferentially-Grooved Liquid Seals Using the Averaged Navier-Stokes Equations," *J. Tribol,* vol. 119, no. 3, pp. 556-567, 1997.

[8] J. J. Moore and A. B. Palazzolo, "Rotordynamic Force Prediction of Whirling Centrifugal Impeller Shroud Passages Using Computational Fluid Dynamic Techniques," *J. Eng. Gas Turbines Power,* vol. 123, no. 4, pp. 910-918, 2001.

[9] N. Kim and D. L. Rhode, "A New CFD-Perturbation Model for the Rotordynamics of Incompressible Flow Seals," in *ASME International Gas Turbine and Aeroengine Congress and Exposition*, Munich, Germany, May 8-11, 2003.

[10] L. T. Tam, A. J. Przekwas, A. Muszynska, R. C. Hendricks, M. J. Braun and R. L. Mullen, "Numerical and Analytical Study of Fluid Dynamic Forces in Seals and Bearings," *ASME J. Vibr. Acoust.,* vol. 110, pp. 315-325, 1988.

[11] A. Untaroiu, H. G. Wood, T. Dimond and P. E. Allaire, "Calculation of Dynamic Coefficients for a Magnetically Levitated Artificial Heart Pump Using a CFD Approach," in *Proceedings of the ASME International Mechanical Engineering Congress and Exposition, Paper No. IMECE2008-67802*, Boston, Massachusetts, October 31 - November 6, 2008.

[12] A. Untaroiu, C. Goyne, C. D. Untaroiu, H. G. Wood, R. Rockwell and P. E. Allaire, "Computational Modeling and Experimental Investigation of Static Straight-Through Labyrinth Seals," in *Proceedings of the ASME International Mechanical Engineering Congress and Exposition, Paper No. IMECE2008-67847*, Boston, Massachusetts, October 31 - November 6, 2008.

[13] A. Untaroiu, C. D. Untaroiu, H. G. Wood and P. E. Allaire, "Numerical Modeling of Fluid-Induced Rotordynamic Forces in Seals With Large Aspect Ratios," *Journal of Engineering for Gas Turbines and Power,* vol. 135, March 2013.

[14] D. L. Rhode, S. H. Ko and G. L. Morrison, "Leakage Optimization of Labyrinth Seals Using a Navier-Stokes Code," *Tribology Transactions,* vol. 37, no. 1, pp. 105-110, 1994.

[15] V. Schramm, J. Denecke, S. Kim and S. Wittig, "Shape Optimization of a Labyrinth Seal Applying the Simulated Annealing Method," *International Journal of Rotating Machinery,* vol. 10, no. 5, pp. 365-371, 2004.

[16] S. P. Asok, K. Sankaranarayanasamy, T. Sundararajan, K. Rajesh and G. Sankar Ganeshan, "Neural network and CFD-based optimisation of square cavity and curved cavity static labyrinth seals," *Tribology International,* vol. 40, pp. 1204-1216, 2007.

[17] A. Bellaouar, B. V. Kopey and N. Abdelbaki, "Methods of the rational choice of a labyrinth seal design for gas pumping units," *Mechanika,* vol. 19, no. 1, pp. 81-86, 2013.

[18] S. Pierret, R. F. Coelho and H. Kato, "Multidisciplinary and multiple operating points shape optimization of three-dimensional compressor blades," *Struct. Multidisc. Optim.,* vol. 33, pp. 61-70, 2007.

[19] ANSYS, Inc., "ANSYS CFX Introduction," Canonsburg, PA, 2011.

[20] ANSYS, Inc., "ANSYS CFX Reference Guide," Cannonsburg, PA, 2011.

[21] ANSYS, Inc., "ANSYS CFX-Solver Theory Guide," Canonsburg, PA, 2011.

[22] J. C. Tannehill, D. A. Anderson and R. H. Pletcher, Computational Fluid Mechanics and Heat Transfer, Taylor and Francis, 2nd Edition, 1997.

[23] ANSYS, Inc., "ANSYS CFX-Solver Modeling Guide," Cannonsburg, PA, 2011.

[24] J. K. Scharrer, "Theory Versus Experiment for the Rotordynamic Coefficients of Labyrinth Gas Seals: Part I - A Two Control Volume Method," *Transactions of the ASME,* vol. 110, pp. 270-280, July 1988.

[25] R. Nordmann and P. Weiser, "Evaluation of Rotordynamic Coefficients of Look-Through Labyrinths by Means of a Three Volume Bulk Flow Model," 1991.

[26] T. W. Ha and A. S. Lee, "A Rotordynamic Analysis of Circumferentially-Grooved Pump Seals Based on a Three-Control-Volume Theory," *KSME International Journal,* vol. 14, no. 3, pp. 261-271, 2000.

[27] P. K. Kundu and I. M. Cohen, Fluid Mechanics, Third Edition, Elsevier, 2004.

[28] W. M. Lai, D. Rubin and E. Krempl, Introduction to Continuum Mechanics, 4th Edition ed., Amsterdam: Butterworth-Heinemann/Elsevier, 2010, pp. p. 374-375.

[29] E. Marsis and G. Morrison, "Leakage and Rotordynamics Numerical Study of Circular Grooved and Rectangular Grooved Labyrinth Seals," in *Proceedings of ASME Turbo Expo 2013: Turbine Technical Conference and Exposition*, San Antonio, Texas, USA, 2013.

[30] L. F. Moody, "Friction Factors for Pipe Flow," *Transactions of ASME,* vol. 66, no. 8, pp. 671-684, 1944.

[31] J. R. Taylor, Classical Mechanics, Sausalito, CA: University Science Books, 2005.

[32] G. E. P. Box, J. S. Hunter and W. G. Hunter, Statistics for Experimenters. Design, Innovation, and Discovery 2nd ed., Hoboken, NJ: John Wiley & Sons, Inc., 2005.

[33] R. A. Fisher, Design of Experiments, New York: Hafner Press, 1974.

[34] S. N. Deming and S. L. Morgan, Experimental design: A Chemometric Approach, Amsterdam: Elsevier, 1993.

[35] N. R. Draper and H. Smith, Applied Regression Analysis, 3rd ed., New York: John Wiley, 1998.

[36] G. Box and J. S. Hunter, "The 2^(k-p) Fractional Factorial Designs: Part I," *Technometrics,* vol. 3, pp. 311-351, 1961a.

[37] G. Box and J. S. Hunter, "The 2^(k-p) Fractional Factorial Designs: Part II," *Technometrics,* vol. 3, pp. 449-

458, 1961b.

[38] R. L. Plackett and J. P. Burman, "The Design of Optimum Multifactorial Experiments," *Biometrika,* vol. 33, pp. 305-325, 1943.

[39] G. Box and K. Wilson, "On the Experimental Attainment of Optimum Conditions," *J. Roy. Statist. Soc.,* vol. Series B, no. 13, pp. 1-45, 1951.

[40] A. Untaroiu, V. Hayrapetian, C. D. Untaroiu, H. G. Wood, B. Schiavello and J. McGuire, "On the Dynamic Properties of Pump Liquid Seals," *Journal of Fluids Engineering,* vol. 135, May 2013.

[41] The Mathworks, Inc., "Optimization Toolbox User's Guide," The Mathworks, Inc., Natick, MA, 2012a.

[42] Stat-Ease, "Design Expert 7.1 Help Documentation," Stat-Ease, Minneapolis, MN, 2007.

[43] S. P. Asok, K. Sankaranarayanasamy, T. Sundararajan, G. Vaidyanathan and K. Udhaya Kumar, "Pressure drop and cavitation investigations on static helical-grooved square, triangular and curved cavity liquid labyrinth seals," *Nuclear Engineering and Design,* vol. 241, pp. 843-853, 2011.

APPENDIX A: EXPERIMENTAL DESIGN DATA POINTS

Table A.1: First parameterization, first experimental design: non-central composite

Run #	Radius 1	Radius 2	Radius 3	Radius 4	Radius 5
1	0.99	0.99	0.99	0.99	0.99
2	0.99	0.99	0.99	0.99	3.18
3	0.99	0.99	0.99	3.18	0.99
4	0.99	0.99	0.99	3.18	3.18
5	0.99	0.99	3.18	0.99	0.99
6	0.99	0.99	3.18	0.99	3.18
7	0.99	0.99	3.18	3.18	0.99
8	0.99	0.99	3.18	3.18	3.18
9	0.99	3.18	0.99	0.99	0.99
10	0.99	3.18	0.99	0.99	3.18
11	0.99	3.18	0.99	3.18	0.99
12	0.99	3.18	0.99	3.18	3.18
13	0.99	3.18	3.18	0.99	0.99
14	0.99	3.18	3.18	0.99	3.18
15	0.99	3.18	3.18	3.18	0.99
16	0.99	3.18	3.18	3.18	3.18
17	3.18	0.99	0.99	0.99	0.99
18	3.18	0.99	0.99	0.99	3.18
19	3.18	0.99	0.99	3.18	0.99
20	3.18	0.99	0.99	3.18	3.18
21	3.18	0.99	3.18	0.99	0.99
22	3.18	0.99	3.18	0.99	3.18
23	3.18	0.99	3.18	3.18	0.99
24	3.18	0.99	3.18	3.18	3.18
25	3.18	3.18	0.99	0.99	0.99
26	3.18	3.18	0.99	0.99	3.18
27	3.18	3.18	0.99	3.18	0.99
28	3.18	3.18	0.99	3.18	3.18
29	3.18	3.18	3.18	0.99	0.99
30	3.18	3.18	3.18	0.99	3.18
31	3.18	3.18	3.18	3.18	0.99
32	3.18	3.18	3.18	3.18	3.18
33	1.59	1.59	1.59	1.59	1.59
34	0.4	1.59	1.59	1.59	1.59
35	4.77	1.59	1.59	1.59	1.59
36	1.59	0.4	1.59	1.59	1.59
37	1.59	4.77	1.59	1.59	1.59
38	1.59	1.59	0.4	1.59	1.59
39	1.59	1.59	4.77	1.59	1.59
40	1.59	1.59	1.59	0.4	1.59
41	1.59	1.59	1.59	4.77	1.59
42	1.59	1.59	1.59	1.59	0.4
43	1.59	1.59	1.59	1.59	4.77
Optimum	4.10	3.91	4.06	3.75	4.55

Table A.2: First parameterization, second experimental design: central composite

Run #	Radius 1	Radius 2	Radius 3	Radius 4	Radius 5
1	4.00	4.00	4.00	4.00	3.41
2	3.41	4.00	4.00	4.00	4.00
3	4.00	4.00	4.59	4.00	4.00
4	4.25	4.25	4.25	3.75	3.75
5	3.75	3.75	3.75	3.75	3.75
6	3.75	3.75	3.75	4.25	4.25
7	4.25	3.75	4.25	3.75	4.25
8	3.75	3.75	4.25	4.25	4.25
9	4.00	4.00	4.00	4.59	4.00
10	4.25	4.25	3.75	4.25	4.25
11	3.75	3.75	4.25	3.75	3.75
12	3.75	3.75	4.25	3.75	4.25
13	3.75	4.25	3.75	3.75	3.75
14	3.75	4.25	3.75	3.75	4.25
15	4.25	3.75	4.25	3.75	3.75
16	4.59	4.00	4.00	4.00	4.00
17	4.00	4.00	4.00	4.00	4.00
18	3.75	4.25	4.25	4.25	4.25
19	4.00	4.00	4.00	4.00	4.59
20	3.75	4.25	3.75	4.25	3.75
21	4.25	4.25	4.25	4.25	3.75
22	3.75	4.25	3.75	4.25	4.25
23	4.00	4.59	4.00	4.00	4.00
24	3.75	4.25	4.25	4.25	3.75
25	4.25	3.75	4.25	4.25	3.75
26	4.25	3.75	3.75	4.25	4.25
27	3.75	3.75	4.25	4.25	3.75
28	4.25	4.25	4.25	3.75	4.25
29	4.25	3.75	3.75	4.25	3.75
30	4.00	4.00	4.00	3.41	4.00
31	3.75	3.75	3.75	3.75	4.25
32	4.25	3.75	3.75	3.75	4.25
33	4.25	3.75	4.25	4.25	4.25
34	4.25	4.25	3.75	3.75	3.75
35	3.75	3.75	3.75	4.25	3.75
36	4.25	4.25	3.75	4.25	3.75
37	3.75	4.25	4.25	3.75	4.25
38	4.25	4.25	4.25	4.25	4.25
39	4.25	3.75	3.75	3.75	3.75
40	4.00	4.00	3.41	4.00	4.00
41	4.25	4.25	3.75	3.75	4.25
42	3.75	4.25	4.25	3.75	3.75
43	4.00	3.41	4.00	4.00	4.00

Table A.3: Second parameterization, five-level factorial design

Run #	Width	Flat Width	Angle In	Angle Out	Depth
1	4.8	2.4	80	80	4.2
2	2.6	0.2	80	80	5.8
3	2.6	1.5	60	30	0.4
4	4.8	2.4	80	80	5.8
5	4.8	0.2	80	80	5.8
6	2.6	0.2	80	80	4.2
7	4.8	4.6	80	80	0.4
8	1.7	0.2	80	80	4.2
9	4.8	2.4	80	60	2.6
10	3.5	2.4	80	30	0.4
11	3.5	0.2	80	80	2.6
12	1.7	0.2	80	80	2.6
13	4.8	0.2	10	10	0.4
14	2.6	1.5	80	80	2.6
15	3.5	2.4	30	45	0.4
16	4.8	2.4	80	80	2.6
17	3.5	0.2	30	10	0.4
18	2.6	0.2	80	60	2.6
19	4.8	0.2	60	80	2.6
20	3.5	0.2	80	80	8
21	3.5	2.4	45	30	0.4
22	3.5	0.2	80	45	2.6
23	1.7	0.2	30	45	0.4
24	4.8	1.5	60	60	2.6
25	4.8	1.5	80	60	4.2
26	4.8	1.5	80	45	2.6
27	4.8	3.3	30	30	0.4
28	4.8	3.3	80	80	2.6
29	3.5	0.2	45	80	2.6
30	3.5	2.4	60	30	0.4
31	4.8	0.2	80	60	5.8
32	3.5	1.5	80	60	2.6
33	1.7	0.2	30	30	0.4
34	3.5	0.2	80	60	4.2
35	2.6	2.4	80	80	0.4
36	3.5	3.3	80	80	0.4
37	4.8	0.2	60	45	2.6
38	4.8	0.2	45	80	2.6
39	4.8	1.5	45	80	2.6
40	3.5	2.4	60	45	0.4
41	3.5	2.4	30	80	0.4
42	4.8	2.4	60	80	2.6
43	4.8	3.3	80	80	4.2
44	3.5	1.5	60	80	2.6
45	2.6	0.2	80	80	2.6
46	4.8	0.2	60	80	4.2
47	4.8	0.2	80	80	8
48	2.6	1.5	30	80	0.4
49	4.8	3.3	45	45	0.4

Run #	Width	Flat Width	Angle In	Angle Out	Depth
50	2.60	1.50	60.00	45.00	0.40
51	3.50	2.40	30.00	60.00	0.40
52	4.80	0.20	80.00	80.00	2.60
53	1.70	1.50	80.00	80.00	0.40
54	3.50	2.40	45.00	60.00	0.40
55	4.80	0.20	60.00	80.00	5.80
56	1.70	0.20	45.00	45.00	0.40
57	2.60	1.50	30.00	45.00	0.40
58	1.70	0.20	45.00	30.00	0.40
59	3.50	2.40	45.00	45.00	0.40
60	3.50	0.20	60.00	80.00	4.20
61	2.60	1.50	30.00	60.00	0.40
62	4.80	1.50	10.00	30.00	0.40
63	3.50	2.40	80.00	80.00	2.60
64	2.60	0.20	60.00	80.00	2.60
65	0.40	0.20	80.00	80.00	0.40
66	4.80	1.50	60.00	80.00	2.60
67	3.50	0.20	80.00	80.00	5.80
68	4.80	1.50	30.00	10.00	0.40
69	2.60	1.50	45.00	30.00	0.40
70	3.50	0.20	80.00	80.00	4.20
71	3.50	0.20	10.00	30.00	0.40
72	4.80	0.20	80.00	80.00	4.20
73	3.50	0.20	60.00	60.00	2.60
74	**4.80**	**3.30**	**45.00**	**30.00**	**0.40**
75	4.80	1.50	80.00	60.00	2.60
76	3.50	0.20	60.00	80.00	2.60
77	2.60	1.50	45.00	60.00	0.40
78	3.50	2.40	60.00	60.00	0.40
79	4.80	0.20	80.00	60.00	2.60
80	4.80	1.50	80.00	80.00	8.00
81	**4.80**	**3.30**	**30.00**	**45.00**	**0.40**
82	2.60	0.20	30.00	30.00	0.40
83	4.80	0.20	60.00	60.00	2.60
84	4.80	1.50	80.00	80.00	4.20
85	4.80	0.20	80.00	45.00	2.60
86	2.60	1.50	60.00	60.00	0.40
87	3.50	0.20	80.00	60.00	2.60
88	3.50	1.50	30.00	30.00	0.40
89	3.50	1.50	80.00	80.00	2.60
90	4.80	1.50	60.00	80.00	4.20
91	4.80	2.40	30.00	30.00	0.40
92	4.80	1.50	80.00	80.00	5.80
93	2.60	1.50	45.00	45.00	0.40
94	4.80	1.50	80.00	80.00	2.60
95	4.80	0.20	80.00	60.00	4.20
96	2.60	1.50	80.00	30.00	0.40
97	4.80	0.20	45.00	60.00	2.60
98	3.50	1.50	80.00	80.00	4.20
Optimum	4.80	3.60	80.00	80.00	0.59

APPENDIX B: EXPERIMENTAL DESIGN RESULTS

Table B.1: First parameterization, first experimental design: non-central composite

Run #	Q [kg/sec]	K_{XX} [N/m]	K_{XY} [N/m]	C_{XX} [N-s/m]	C_{XY} [N-s/m]	M_{XX} [kg]	M_{XY} [kg]
1	9.340	1.990E+07	5.921E+08	3.461E+05	2.808E+04	14.088	0.209
2	9.112	1.964E+07	6.086E+08	3.545E+05	2.796E+04	14.077	0.001
3	9.116	1.952E+07	6.062E+08	3.532E+05	2.803E+04	14.139	0.308
4	9.082	1.897E+07	6.251E+08	3.633E+05	2.775E+04	13.968	0.461
5	9.009	1.857E+07	6.125E+08	3.563E+05	2.767E+04	13.989	0.555
6	9.007	1.893E+07	6.360E+08	3.689E+05	2.774E+04	13.826	0.128
7	9.016	1.938E+07	6.270E+08	3.627E+05	2.817E+04	13.908	0.372
8	8.924	1.895E+07	6.410E+08	3.713E+05	2.776E+04	13.860	0.297
9	9.201	1.942E+07	5.997E+08	3.497E+05	2.816E+04	14.162	0.118
10	9.080	1.942E+07	6.313E+08	3.659E+05	2.799E+04	13.931	0.307
11	9.007	1.950E+07	6.359E+08	3.681E+05	2.810E+04	13.858	0.238
12	8.939	1.933E+07	6.455E+08	3.738E+05	2.788E+04	13.849	-0.039
13	9.026	1.970E+07	6.324E+08	3.672E+05	2.823E+04	13.952	0.357
14	8.959	1.976E+07	6.484E+08	3.750E+05	2.822E+04	13.905	-0.023
15	8.861	1.940E+07	6.506E+08	3.760E+05	2.806E+04	13.811	0.019
16	8.784	1.930E+07	6.658E+08	3.854E+05	2.822E+04	13.810	-0.140
17	9.204	1.990E+07	6.062E+08	3.520E+05	2.822E+04	14.153	0.156
18	9.049	1.910E+07	6.315E+08	3.665E+05	2.776E+04	13.902	0.237
19	9.093	1.990E+07	6.191E+08	3.589E+05	2.828E+04	14.008	0.040
20	8.927	1.909E+07	6.491E+08	3.755E+05	2.779E+04	13.847	0.129
21	8.926	1.945E+07	6.431E+08	3.717E+05	2.800E+04	13.778	0.250
22	8.915	1.935E+07	6.489E+08	3.754E+05	2.807E+04	13.903	0.107
23	8.898	1.915E+07	6.497E+08	3.764E+05	2.799E+04	13.864	0.206
24	8.782	1.958E+07	6.657E+08	3.849E+05	2.821E+04	13.777	-0.313
25	8.999	1.930E+07	6.382E+08	3.705E+05	2.791E+04	13.844	0.178
26	8.844	1.912E+07	6.540E+08	3.779E+05	2.796E+04	13.900	0.293
27	8.853	1.970E+07	6.492E+08	3.765E+05	2.805E+04	13.905	-0.036
28	8.774	1.886E+07	6.634E+08	3.846E+05	2.809E+04	13.798	-0.025
29	8.833	1.884E+07	6.550E+08	3.792E+05	2.797E+04	13.730	0.194
30	8.702	1.916E+07	6.693E+08	3.872E+05	2.817E+04	13.760	0.160
31	8.815	1.981E+07	6.584E+08	3.801E+05	2.844E+04	13.837	0.270
32	8.616	1.909E+07	6.906E+08	3.984E+05	2.808E+04	13.773	0.132
33	9.076	1.981E+07	6.054E+08	3.546E+05	2.810E+04	14.067	0.122
34	9.178	2.047E+07	5.968E+08	3.465E+05	2.863E+04	14.110	0.236
35	9.024	2.021E+07	6.327E+08	3.654E+05	2.841E+04	13.937	0.694
36	9.185	2.034E+07	5.972E+08	3.477E+05	2.847E+04	14.137	-0.083
37	9.036	1.918E+07	6.428E+08	3.721E+05	2.798E+04	13.788	0.286
38	9.241	2.032E+07	5.970E+08	3.473E+05	2.839E+04	14.229	0.075
39	8.994	1.949E+07	6.365E+08	3.681E+05	2.810E+04	13.759	1.041
40	9.246	2.034E+07	5.929E+08	3.462E+05	2.836E+04	14.127	-0.032
41	9.029	1.945E+07	6.357E+08	3.672E+05	2.787E+04	13.809	0.819
42	9.210	2.055E+07	5.964E+08	3.477E+05	2.842E+04	14.151	0.096
43	9.001	1.841E+07	6.446E+08	3.729E+05	2.751E+04	13.773	0.302
Optimum	8.540	1.914E+07	7.229E+08	4.137E+05	2.865E+04	13.740	0.155

Table B.2: First parameterization, second experimental design: central composite

Run #	Q [kg/sec]	K_{XX} [N/m]	K_{XY} [N/m]	C_{XX} [N-s/m]	C_{XY} [N-s/m]	M_{XX} [kg]	M_{XY} [kg]
1	8.571	1.896E+07	7.186E+08	4.116E+05	2.836E+04	13.673	0.372
2	8.539	1.891E+07	7.200E+08	4.137E+05	2.854E+04	13.716	0.404
3	8.548	1.920E+07	7.350E+08	4.197E+05	2.880E+04	13.607	0.426
4	8.589	1.895E+07	7.197E+08	4.116E+05	2.844E+04	13.714	-0.109
5	8.566	1.894E+07	7.120E+08	4.088E+05	2.856E+04	13.756	0.153
6	8.592	1.927E+07	7.099E+08	4.052E+05	2.835E+04	13.767	0.309
7	8.546	1.935E+07	7.325E+08	4.196E+05	2.857E+04	13.696	0.406
8	8.570	1.885E+07	7.138E+08	4.086E+05	2.836E+04	13.675	0.387
9	8.547	1.905E+07	7.258E+08	4.166E+05	2.870E+04	13.626	0.119
10	8.513	1.845E+07	7.321E+08	4.193E+05	2.837E+04	13.640	0.235
11	8.577	1.862E+07	7.122E+08	4.098E+05	2.820E+04	13.671	0.082
12	8.564	1.915E+07	7.102E+08	4.062E+05	2.850E+04	13.829	0.350
13	8.606	1.865E+07	7.052E+08	4.069E+05	2.817E+04	13.690	0.127
14	8.533	1.920E+07	7.130E+08	4.080E+05	2.844E+04	13.715	0.328
15	8.554	1.889E+07	7.137E+08	4.098E+05	2.853E+04	13.687	0.766
16	8.565	2.002E+07	7.229E+08	4.138E+05	2.861E+04	13.612	0.087
17	8.582	1.885E+07	7.163E+08	4.110E+05	2.844E+04	13.668	0.457
18	8.519	1.886E+07	7.249E+08	4.174E+05	2.849E+04	13.662	0.185
19	8.558	1.993E+07	7.219E+08	4.135E+05	2.877E+04	13.640	-0.135
20	8.553	1.878E+07	7.131E+08	4.101E+05	2.827E+04	13.655	0.045
21	8.544	1.920E+07	7.358E+08	4.217E+05	2.812E+04	13.654	0.096
22	8.550	1.978E+07	7.171E+08	4.105E+05	2.848E+04	13.593	0.939
23	8.554	1.943E+07	7.314E+08	4.180E+05	2.880E+04	13.630	-0.019
24	8.573	1.942E+07	7.159E+08	4.104E+05	2.852E+04	13.723	0.145
25	8.530	1.903E+07	7.271E+08	4.168E+05	2.848E+04	13.719	0.061
26	8.562	1.958E+07	7.297E+08	4.167E+05	2.865E+04	13.632	0.200
27	8.585	1.895E+07	7.104E+08	4.079E+05	2.834E+04	13.744	0.068
28	8.534	1.911E+07	7.390E+08	4.244E+05	2.829E+04	13.591	-0.054
29	8.560	1.915E+07	7.154E+08	4.114E+05	2.837E+04	13.674	0.275
30	8.551	1.900E+07	7.188E+08	4.125E+05	2.844E+04	13.670	0.355
31	8.625	1.880E+07	7.043E+08	4.056E+05	2.814E+04	13.680	0.146
32	8.540	1.897E+07	7.160E+08	4.108E+05	2.850E+04	13.786	0.348
33	8.549	1.864E+07	7.302E+08	4.195E+05	2.829E+04	13.625	0.062
34	8.581	1.918E+07	7.184E+08	4.125E+05	2.836E+04	13.567	0.291
35	8.625	1.896E+07	7.094E+08	4.073E+05	2.848E+04	13.747	0.452
36	8.566	1.887E+07	7.236E+08	4.148E+05	2.835E+04	13.673	0.127
37	8.559	1.909E+07	7.244E+08	4.147E+05	2.832E+04	13.669	0.375
38	8.515	1.844E+07	7.362E+08	4.224E+05	2.827E+04	13.643	0.286
39	8.557	1.974E+07	7.124E+08	4.084E+05	2.865E+04	13.695	0.107
40	8.539	1.958E+07	7.194E+08	4.113E+05	2.870E+04	13.627	0.217
41	8.534	1.926E+07	7.354E+08	4.209E+05	2.845E+04	13.610	0.140
42	8.600	1.937E+07	7.091E+08	4.060E+05	2.868E+04	13.714	0.489
43	8.539	1.939E+07	7.251E+08	4.150E+05	2.849E+04	13.624	0.379

Table B.3: Second parameterization, five-level factorial design

Run #	Q [kg/sec]	K_{XX} [N/m]	K_{XY} [N/m]	C_{XX} [N-s/m]	C_{XY} [N-s/m]	M_{XX} [kg]	M_{XY} [kg]
1	9.498	2.031E+07	5.851E+08	3.497E+05	2.768E+04	14.150	0.072
2	9.814	2.128E+07	5.499E+08	3.286E+05	2.836E+04	14.322	0.056
3	9.891	2.103E+07	5.838E+08	3.387E+05	2.885E+04	14.136	0.210
4	9.298	1.950E+07	5.887E+08	3.573E+05	2.711E+04	14.097	-0.076
5	9.349	2.010E+07	5.921E+08	3.557E+05	2.747E+04	14.129	0.014
6	9.831	2.115E+07	5.522E+08	3.299E+05	2.834E+04	14.295	0.066
7	8.941	1.756E+07	7.621E+08	4.347E+05	2.705E+04	13.342	0.428
8	10.198	2.243E+07	5.323E+08	3.141E+05	2.933E+04	14.396	0.046
9	9.490	2.106E+07	5.895E+08	3.469E+05	2.842E+04	14.205	-0.016
10	9.668	2.006E+07	6.274E+08	3.614E+05	2.809E+04	13.888	0.370
11	9.897	2.306E+07	5.458E+08	3.209E+05	2.948E+04	14.421	0.097
12	10.198	2.254E+07	5.333E+08	3.143E+05	2.938E+04	14.391	-0.027
13	12.753	3.826E+07	4.824E+08	2.627E+05	3.957E+04	15.327	-0.136
14	9.976	2.219E+07	5.447E+08	3.211E+05	2.916E+04	14.381	0.150
15	10.296	1.979E+07	6.311E+08	3.584E+05	2.851E+04	13.777	0.189
16	9.255	2.094E+07	5.962E+08	3.526E+05	2.824E+04	14.133	-0.053
17	11.222	2.551E+07	5.376E+08	3.057E+05	3.173E+04	14.328	0.110
18	9.909	2.241E+07	5.483E+08	3.237E+05	2.910E+04	14.427	0.139
19	9.321	2.050E+07	6.044E+08	3.540E+05	2.820E+04	14.121	0.107
20	9.507	2.052E+07	5.673E+08	3.416E+05	2.781E+04	14.256	0.075
21	10.151	2.025E+07	6.201E+08	3.548E+05	2.840E+04	13.775	0.205
22	9.770	2.152E+07	5.685E+08	3.355E+05	2.860E+04	14.305	0.139
23	10.557	2.241E+07	5.423E+08	3.134E+05	2.977E+04	14.377	0.144
24	9.575	2.076E+07	5.999E+08	3.508E+05	2.840E+04	14.113	-0.016
25	9.459	2.047E+07	5.942E+08	3.535E+05	2.793E+04	14.167	-0.020
26	9.656	2.170E+07	5.916E+08	3.455E+05	2.872E+04	14.165	0.342
27	10.956	2.055E+07	6.539E+08	3.668E+05	2.988E+04	13.848	-0.107
28	9.312	2.100E+07	5.954E+08	3.508E+05	2.841E+04	14.209	-0.001
29	9.688	2.006E+07	5.880E+08	3.445E+05	2.825E+04	14.196	-0.084
30	9.851	2.065E+07	6.212E+08	3.572E+05	2.842E+04	13.911	0.220
31	9.411	2.059E+07	5.957E+08	3.532E+05	2.796E+04	14.121	0.221
32	9.820	2.193E+07	5.596E+08	3.303E+05	2.873E+04	14.321	0.150
33	10.821	2.390E+07	5.278E+08	3.040E+05	3.049E+04	14.412	0.178
34	9.619	2.151E+07	5.672E+08	3.368E+05	2.860E+04	14.384	0.096
35	9.132	1.938E+07	6.249E+08	3.645E+05	2.786E+04	14.004	-0.054
36	8.929	1.714E+07	6.874E+08	3.975E+05	2.717E+04	13.782	0.134
37	9.717	2.074E+07	6.042E+08	3.519E+05	2.835E+04	14.076	0.251
38	9.494	2.028E+07	6.129E+08	3.564E+05	2.814E+04	14.072	0.191
39	9.476	2.034E+07	6.099E+08	3.562E+05	2.809E+04	14.017	0.077
40	9.615	1.858E+07	6.442E+08	3.695E+05	2.794E+04	13.901	0.386
41	9.654	1.559E+07	6.892E+08	3.937E+05	2.688E+04	13.678	0.032
42	9.402	2.053E+07	5.983E+08	3.514E+05	2.819E+04	14.064	-0.078
43	9.460	2.026E+07	5.865E+08	3.514E+05	2.767E+04	14.163	0.156
44	9.754	2.124E+07	5.667E+08	3.337E+05	2.868E+04	14.287	0.166
45	10.005	2.234E+07	5.401E+08	3.192E+05	2.915E+04	14.360	0.126
46	9.317	1.992E+07	6.067E+08	3.596E+05	2.776E+04	14.052	0.092
47	9.271	1.949E+07	5.969E+08	3.611E+05	2.701E+04	14.068	-0.109
48	9.740	1.817E+07	6.245E+08	3.601E+05	2.759E+04	13.800	0.038
49	9.970	1.592E+07	6.979E+08	3.967E+05	2.806E+04	13.754	-0.146

Run #	Q [kg/sec]	K_{XX} [N/m]	K_{XY} [N/m]	C_{XX} [N-s/m]	C_{XY} [N-s/m]	M_{XX} [kg]	M_{XY} [kg]
50	9.709	2.065E+07	5.961E+08	3.452E+05	2.871E+04	14.142	0.061
51	9.974	1.662E+07	6.634E+08	3.791E+05	2.843E+04	14.047	-0.280
52	9.150	2.057E+07	6.013E+08	3.550E+05	2.820E+04	14.136	0.205
53	9.675	2.144E+07	5.651E+08	3.316E+05	2.886E+04	14.295	0.099
54	9.556	1.795E+07	6.560E+08	3.774E+05	2.756E+04	13.751	0.085
55	9.369	1.975E+07	6.037E+08	3.587E+05	2.753E+04	14.028	0.023
56	10.166	2.245E+07	5.468E+08	3.188E+05	2.953E+04	14.394	0.128
57	10.312	2.106E+07	5.856E+08	3.364E+05	2.929E+04	14.158	-0.011
58	10.417	2.327E+07	5.375E+08	3.115E+05	3.002E+04	14.443	0.247
59	9.811	1.874E+07	6.387E+08	3.661E+05	2.804E+04	13.862	0.386
60	9.631	2.064E+07	5.758E+08	3.415E+05	2.823E+04	14.279	0.041
61	10.033	1.943E+07	6.068E+08	3.491E+05	2.853E+04	14.045	0.019
62	12.263	2.466E+07	6.346E+08	3.453E+05	3.247E+04	14.103	-0.030
63	9.832	2.220E+07	5.503E+08	3.250E+05	2.908E+04	14.391	0.145
64	9.857	2.144E+07	5.580E+08	3.291E+05	2.869E+04	14.318	0.063
65	10.799	2.535E+07	5.050E+08	2.919E+05	3.127E+04	14.560	0.050
66	9.373	2.061E+07	6.005E+08	3.529E+05	2.824E+04	14.123	-0.115
67	9.574	2.014E+07	5.616E+08	3.378E+05	2.781E+04	14.248	0.181
68	11.329	2.645E+07	5.606E+08	3.156E+05	3.239E+04	14.141	0.139
69	10.160	2.167E+07	5.735E+08	3.313E+05	2.919E+04	14.157	0.270
70	9.642	2.121E+07	5.657E+08	3.363E+05	2.835E+04	14.301	0.149
71	11.883	2.201E+07	6.033E+08	3.346E+05	3.073E+04	14.109	0.102
72	9.565	2.083E+07	5.722E+08	3.417E+05	2.808E+04	14.191	0.141
73	9.732	2.149E+07	5.738E+08	3.368E+05	2.870E+04	14.291	0.113
74	**10.314**	**1.972E+07**	**6.718E+08**	**3.813E+05**	**2.865E+04**	**13.702**	**0.020**
75	9.471	2.126E+07	5.871E+08	3.456E+05	2.863E+04	14.224	0.221
76	9.761	2.137E+07	5.629E+08	3.312E+05	2.887E+04	14.294	0.139
77	9.662	1.881E+07	6.092E+08	3.536E+05	2.802E+04	14.020	0.115
78	9.336	1.781E+07	6.662E+08	3.842E+05	2.742E+04	13.772	0.150
79	9.381	2.118E+07	5.910E+08	3.478E+05	2.854E+04	14.211	0.160
80	9.175	1.907E+07	5.972E+08	3.641E+05	2.669E+04	14.064	-0.001
81	**10.541**	**1.772E+07**	**6.897E+08**	**3.868E+05**	**2.868E+04**	**13.792**	**0.280**
82	10.680	2.258E+07	5.624E+08	3.218E+05	3.003E+04	14.220	0.218
83	9.516	2.085E+07	5.980E+08	3.497E+05	2.841E+04	14.107	0.237
84	9.499	2.067E+07	5.799E+08	3.461E+05	2.782E+04	14.116	0.113
85	9.625	2.134E+07	5.897E+08	3.451E+05	2.875E+04	14.227	0.226
86	9.479	1.951E+07	6.108E+08	3.549E+05	2.816E+04	13.986	0.057
87	9.829	2.242E+07	5.558E+08	3.280E+05	2.912E+04	14.393	0.076
88	10.681	2.129E+07	6.067E+08	3.441E+05	2.951E+04	13.884	0.284
89	9.793	2.233E+07	5.517E+08	3.267E+05	2.900E+04	14.381	-0.028
90	9.406	2.002E+07	6.060E+08	3.589E+05	2.752E+04	14.014	0.011
91	11.014	2.135E+07	6.464E+08	3.612E+05	3.034E+04	13.905	0.049
92	9.314	2.009E+07	5.920E+08	3.558E+05	2.750E+04	14.127	0.003
93	9.880	1.990E+07	5.940E+08	3.434E+05	2.851E+04	14.092	0.215
94	9.286	2.100E+07	5.931E+08	3.498E+05	2.844E+04	14.198	0.080
95	9.460	2.041E+07	5.905E+08	3.509E+05	2.797E+04	14.199	0.239
96	9.752	2.135E+07	5.805E+08	3.377E+05	2.892E+04	14.203	0.243
97	9.503	2.039E+07	6.215E+08	3.609E+05	2.825E+04	14.007	0.053
98	9.606	2.100E+07	5.607E+08	3.358E+05	2.815E+04	14.309	0.085
Optimum	8.386	1.634E+07	7.722E+08	4.433E+05	2.742E+04	13.508	0.202